# THE MONITORING AND MULTIPLEXING OF FIBER OPTIC SENSORS USING CHIRPED LASER SOURCES

A Dissertation

by

XIAOKE WAN

Submitted to the Office of Graduate Studies of
Texas A&M University
in partial fulfillment of the requirements for the degree of

DOCTOR OF PHILOSOPHY

May 2003

Major Subject: Electrical Engineering

# THE MONITORING AND MULTIPLEXING OF FIBER OPTIC SENSORS USING CHIRPED LASER SOURCES

A Dissertation

by

XIAOKE WAN

Submitted to the Office of Graduate Studies of
Texas A&M University
in partial fulfillment of the requirements for the degree of

DOCTOR OF PHILOSOPHY

May 2003

Major Subject: Electrical Engineering

# THE MONITORING AND MULTIPLEXING OF FIBER OPTIC SENSORS USING CHIRPED LASER SOURCES

A Dissertation

by

XIAOKE WAN

Submitted to Texas A&M University
in partial fulfillment of the requirements
for the degree of

DOCTOR OF PHILOSOPHY

Approved as to style and content by:

| | |
|---|---|
| Ohannes Eknoyan<br>(Chair of Committee) | |
| Chin B. Su<br>(Member) | Andrew K. Chan<br>(Member) |
| Robert A. Kenefick<br>(Member) | C. Singh<br>(Head of Department) |

May 2003

Major Subject: Electrical Engineering

# ABSTRACT

The Monitoring and Multiplexing of Fiber Optic Sensors
Using Chirped Laser Sources. (May 2003)
Xiaoke Wan,
B.S., Jilin University, China;
M.S., Chinese Academy of Sciences;
M.S., Texas A&M University
Chair of Advisory Committee: Dr. Ohannes Eknoyan

A wide band linearly chirped erbium-doped fiber laser has been developed. The erbium-doped fiber laser using a rotating mirror/grating combination as one of the reflectors in a Fabry-Perot laser cavity has been tuned over a 46 nm spectral range. Linearization of the chirp rate has been achieved using feedback from a fiber Fabry-Perot interferometer (FFPI) to adjust the voltage ramp which drives the rotating mirror. In a demonstration of monitoring an array of two fiber Bragg grating (FBG) sensors, a wavelength resolution of 1.7 pm has been achieved.

The linearly chirped fiber laser has been used in measuring the optical path difference (OPD) of interferometric fiber optic sensors by performing a Fourier transform of the optical signal. Multiplexing of an array of three FFPI sensors of different lengths has been demonstrated, with an OPD resolution ranging from 3.6 nm to 6.3 nm. Temperature was measured with one of the sensors over the range from 20°C to 610°C with a resolution of 0.02°C.

Short FBGs are used to form the two mirrors of a fiber Bragg grating pair interferometer (FBGPI) sensor, so that the mirror reflectances change gradually as a function of temperature. Modulating the drive current of a DFB laser produces chirping

of the laser frequency to scan over ~2.5 fringes of the FBGPI reflectance spectrum. Because the fringes are distinguished due to the FBG reflectance change, the ambient temperature can be determined over the range from 24 $^{o}$C to 367 $^{o}$C with a resolution of 0.004 $^{o}$C.

Multiplexing of FBGPI sensors of different lengths with a linearly chirped fiber laser has demonstrated improved sensitivity and multiplexing capacity over a conventional FBG WDM system. The FBG spectral peak position and the phase shift of an FBGPI are determined through the convolution of the sensor reflected signal with an appropriately matched reference waveform, even though the reflectance spectra for the FBGs from different sensors overlap over a wide temperature range. A spectral resolution for the FBG reflectance peak of 0.045 GHz (0.36 pm), corresponding to a temperature resolution of 0.035 $^{o}$C, has been achieved.

To my family

# ACKNOWLEDGMENTS

I would like to express my appreciation to Dr. Ohannes Eknoyan for serving as the chair of my committee. I would also appreciate Dr. Chin B. Su, Dr. Andrew K. Chan, Dr. Robert A. Kenefick for serving on my committee and Dr. David Pugh as my GCR. I would like to greatly appreciate Ms. Lynette Huval and Mr. Robert Atkins for their daily support to our lab. I would also like to express my gratitude to my former mentors, Professor Lihuang Lin at SIOFM, China, and Dr. Edward Fry in Physics Department.

I would like to express my greatest gratitude to Dr. Henry F. Taylor. It would have been impossible for me to complete this research without his guidance and detailed help. His profound knowledge and generosity have been an invaluable resource through my research study.

I am very thankful for all former and current students who have provided me advice, assistance, friendship and a great working environment. I want to thank Dr. Yichao Chen and Ms. Zhaoyia Xie for helping me to make FFPI sensors, Mr. Kyongtae Park for assistance with circuitry and optics layout, Mr. Juan Jurez for help with programing and computers, Taehan Bae for providing a high reflectance fiber. I also thank Ms. Jane Wang, Dr. Kyoo Nam Choi, Mr. Jongseo Lee, Mr. Apichai Bhatranand, Ms. Hsin-Hui Kuo, Dr. Pingsheng Tang, Mr. Yang Ping, Dr. Cheng Peng, Dr. Seongmin Yim, and Mr. Donghua Gu for their help and friendship. I thank Dr. Chun Lee and Mr. Jim Gardner at Fiber Dynamics Inc. for their assistance.

I also want to thank my friends in the Physics Department for their help and friendship. They are Dr. Cunyun Ye, Dr. Cechan Tian, Dr. Gangyao Xiao, Dr. Jun Yang, Dr. Chun Wang, Dr. Dahe Liu and Mr. Tiegang Di.

# TABLE OF CONTENTS

Page

Page

Page

# LIST OF FIGURES

Page

Page

Page

Page

# LIST OF TABLES

Page

# I. INTRODUCTION

## 1.1. Background and motivation

Although optical fibers are primarily used in optical communications, they are also very useful for sensing applications. Optical fiber sensors are small in size, light in weight, and geometrically versatile so they can be configured as "point" or "distributed" sensors. Their ability to withstand high temperature and pressure makes them ideal for applications in harsh environments. The low optical loss of the fibers makes it possible to locate sensors far from the signal processing electronics. Fiber optic sensors are also inherently immune to electro-magnetic interference. Additional desired features of optical fiber sensor systems include high resolution, the ability to obtain accurate measurement from a "cold start", multiplexing capability, and simple, low-cost signal processing.

A Fiber Fabry-Perot interferometer (FFPI) sensor is the cavity between two dielectric mirrors formed inside a single mode fiber.[1] It is extremely sensitive to perturbations (i.e., temperature and strain) which affect the optical path difference (OPD) of the sensor cavity. Since FFPI sensors were first fabricated at Texas A&M University in 1988, several schemes have been developed for their monitoring and multiplexing. The use of a chirped diode laser as the light source provides a simple approach to monitor FFPI sensors.[2] However, due to the ambiguity between interference fringes, it can not achieve an accurate measurement from a "cold start". White light interferometry (WLI) is established as a practical method of measuring the absolute OPD in interferometric sensors.[3] Compared to the laser monitoring technique, it offers two important advantages: the ability to make accurate measurement from "cold start", and the ability to monitor many sensors deployed along a single fiber using coherence

---

The journal model is Applied Optics.

multiplexing. However, optical implementation and signal processing for a WLI system are somewhat complex.

A Fiber Bragg grating (FBG) is a section of fiber with refractive index periodically modulated along the fiber axis.[4] The FBG reflects light at a wavelength which is sensitive to a temperature or a strain perturbation. FBG sensors have very low excess loss, can be monitored in a straightforward manner, and are amenable to multiplexing. A typical wavelength division multiplexing (WDM) scheme monitors an array of FBG sensors with a broadband light source and a wavelength detecting device for signal demodulation. Various wavelength detecting techniques have been demonstrated with use of an optical spectrum analyzer (OSA), edge filters, scanning filters and interferometers. However, these schemes have shown difficulties associated with low spectral resolution of the filters or spectrometers, or limited dynamic range with the interferometric phase read out. In addition, the multiplexing capacity of a WDM sensor system is limited because the sensors are generally not allowed to share optical spectrum bandwidth.

### 1.2. Objective

In this research, several novel techniques the monitoring and multiplexing of FFPI and FBG sensors with chirped laser sources are investigated. The objective is to provide cost-effective solutions, either in a form of a simple arrangement for single sensor monitoring or a system with improved multiplexing capacity, for "cold start" measurements with high resolution ($< 0.1\ ^{o}C$) over a large dynamic range ($> 300\ ^{o}C$).

A wideband linearly chirped erbium-doped fiber laser is developed for the sensor applications.[5] Using an arrangement of a rotating mirror and a bulk grating in the Littrow configuration, the laser is tuned over the entire erbium-doped fiber gain spectral region while keeping a narrow linewidth. The frequency shift is monitored by an FFPI sensor such that the laser frequency is shifted at a constant rate with a feedback control loop.

Monitoring and multiplexing of an array of FFPI sensors using a linearly chirped fiber laser is tested theoretically and demonstrated experimentally.[6] This method represents an optical implementation of the frequency modulated continuous wave (FMCW) technique first applied in radar systems. The reflected signal from each FFPI sensor is modulated at a frequency proportional to the OPD of the sensor, such that the OPD is determined from the Fourier transform of the detected signal. Taking advantage of the wide wavelength tuning range, this technique allows using both the amplitude and phase of the Fourier transform to obtain spatial resolution <<1 wavelength and range >>1 wavelength. Because of the primary benefit of laser monitoring – high fiber-coupled optical power and high signal-to-noise ratio - this scheme is capable of achieving a higher dynamic range for an individual sensor and also enables the multiplexing of a greater number of sensors with a single light source and photodetector than is possible with a conventional WLI setup. Furthermore, optical implementation of the chirped laser is somewhat simpler than a conventional WLI system.

The FBG pair interferometer (FBGPI) is introduced: an FFPI constructed using FBG mirrors with similar reflectance spectra.[7] This new sensing element combines the benefit of the high resolution of an FFPI sensor and the wavelength demodulation technique in an FBG sensor. In a simple arrangement using a current modulated diode laser, the laser-chirping-induced interference pattern of the FBGPI sensor is monitored. Because the spectral dependence of the FBG mirror reflectances provides coarse measurement capability in conjunction with the fine resolution of the interference fringes, it provides a “cold start” measurement with high resolution.

Finally, an array of FBGPI sensors monitored with the wide band tunable fiber laser is demonstrated in theory and experiment.[8] The sensor signal is convolved with in-phase and quadrature components of a reference waveform corresponding to an interferometer of approximately the same length to obtain a coarse measurement of the optical frequency corresponding to the FBG reflectance peak, and refine this measurement to a higher level of precision, using the phase of the convolved signal. Compared to a conventional FBG sensor system, it provides an improved resolution

because of the determination of phase as well an enhanced multiplexing capacity by allowing multiple sensors to share the same regime of the optical spectrum.

# II. THE FIBER FABRY-PEROT INTERFEROMETER SENSOR

## 2.1. Introduction

The Fabry-Perot interferometer (FPI), sometimes called the Fabry-Perot etalon, has been widely used for high-resolution spectroscope since its invention in the late 19th century.[9,10] The first fiber Fabry-Perot interferometer (FFPI) appeared in the early 1980s, when it began to be applied to the sensing of temperature, strain and pressure.

The FPI is extremely sensitive to perturbations which affect the optical path length between the mirrors. Unlike other fiber interferometers (Mach-Zehnder, Michelson, Sagnac), the FFPI contains no fiber couplers – components which can complicate the interpretation of data. The compact size of the FFPI also enables "point" sensing in some applications. Finally, it is amenable to the application of space division, time division, and coherence multiplexing techniques for reducing the cost of multi-point monitoring.

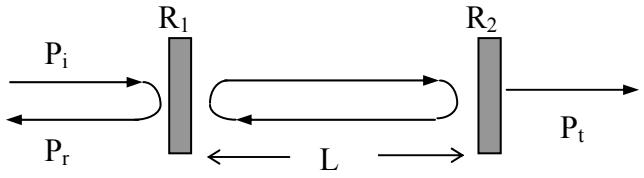


Fig. 1. Fabry-Perot interferometer, with $P_i$, $P_r$, and $P_t$ the incident, reflected, and transmitted optical power.

## 2.2. Theory

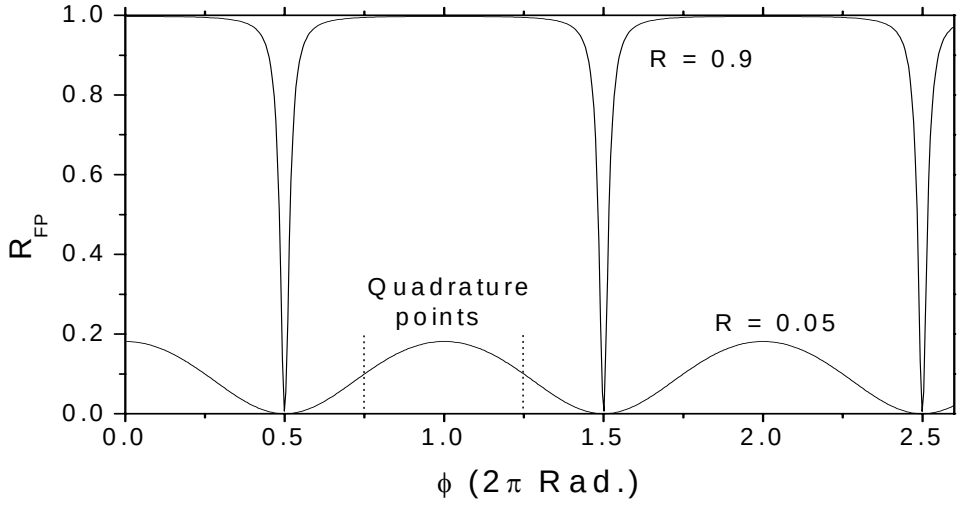


Fig. 2. The reflectance R as a function of the round trip phase shift for two individual mirror reflectance value, R=0.9 and R=0.05. The quadrature points, halfway between the maximum and minimum reflectance points, represents the greatest sensitivity of reflectance to phase change.

An FPI consists of two mirrors of reflectance $R_1$ and $R_2$ separated by a cavity length of L, shown as in Fig. 1. The Fabry-Perot reflectance and transmittance are given by

$$R_{FP} = (R_1 + R_2 + 2R_1R_2\cos\phi)/(1 + R_1R_2 + 2\sqrt{R_1R_2}\cos\phi), \tag{2.1}$$

$$T_{FP} = (1 - R_1)\cdot(1 - R_2)/(1 + R_1R_2 + 2\sqrt{R_1R_2}\cos\phi), \tag{2.2}$$

where the round-trip propagation phase shift, is given by

$$\phi = 4\pi nL / \lambda , \tag{2.3}$$

with n the refractive index and λ the free space optical wavelength. It is evident from eq.(2.1) that $R_{FP}$ is maximum for $\phi = 2m\pi$, with $m$ an integer. In the case that $R=R_1=R_2$, with $R<<1$, then

$$R_{FP} \cong 2R \cdot (1 + \cos\phi) , \tag{2.4}$$

$$T_{FP} \cong 1 - 2R \cdot (1 + \cos\phi) . \tag{2.5}$$

According to eq. (2.1), the reflectance is plotted as a function of phase shift in Fig. 2 with R=0.9 and R=0.05. The approximation expression from eq. (2.4) closely follows the curve in the latter case.

### 2.3. FPI sensor configuration

As shown in Fig. 3, an intrinsic FFPI has two internal mirrors followed by a "non-reflecting" fiber end. The internal mirrors formed from dielectric coatings have shown good mechanical properties,[1] low excess loss, and a wide range of reflectance. The most commonly used mirror material is $TiO_2$, which has a refractive index of 2.4 (vs. 1.46 for fused silica). Thus the reflection results from refractive index discontinuities at the two film-fiber interfaces. A film ~100 nm thick is deposited on the end of a fiber by electron beam evaporation. This fiber is then fusion spliced to the end of a second uncoated fiber. The fusion splicer is operated at lower arc current and duration than for a normal splice, and several splicing pulses are applied.[1] The mirror reflectance generally decreases as a function of the number of splicing pulses, making it possible to select a desired reflectance over the range from ~1% to about 10%. An excess loss as low as 1% can be achieved. Cavity lengths from 100 μm to 1 m have been demonstrated, with lengths in the vicinity of 1 cm commonly used.

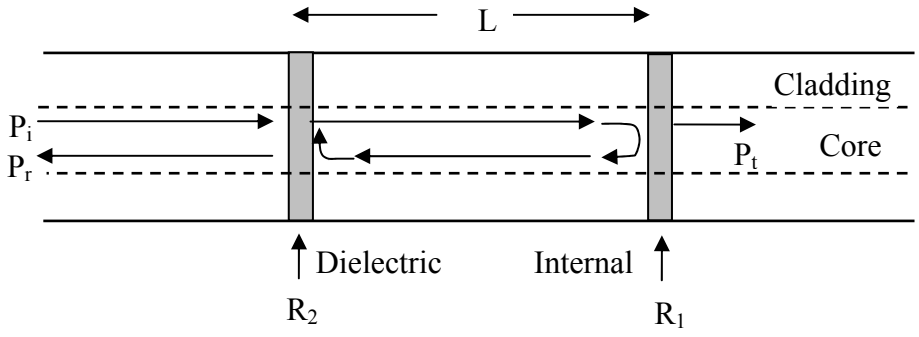


Fig. 3. FFPI sensor with dielectric internal mirrors.

## 2.4. Interrogation methods

In most electrical sensors (e.g., thermocouples for temperature, piezoelectric pressure sensors) the raw signal is a monotonic and fairly linear function of the measurand. In the case of interferometric optic sensors, it is often not so straightforward. Following eq. (2.3), the phase shift change is in the form

$$\Delta\phi = \frac{4\pi}{\lambda}(L\frac{dn}{dT} + n\frac{dL}{dT})\Delta T\,, \tag{2.6}$$

where $\Delta T$ is the ambient temperature change. The refractive index variation with temperature (first term in parentheses in the above equation) dominates over the effect of length change with temperature in silica fibers. The value of $\frac{1}{\phi}\cdot\frac{dn}{dT}$ is ~$8\times10^{-6}$/ $^{o}$C in a silica fiber at room temperature, and changes only slightly over the range from 0 – 600 $^{o}$C.[11] Since the phase shift can not be directly measured, it is determined from the optical signal, e.g., reflectance or transmittance, which is often a highly nonlinear function of the phase shift. It is evident from Fig. 2 that the reflectance signal is a periodic function of the round trip phase shift in the cavity. Determining the measurand-

induced phase shift from the optical signal is a major challenge in an interferometric system.

### 2.4.1. Laser (single wavelength)

A simple experimental arrangement for monitoring the reflectance of an FFPI sensor using a single laser is shown in Fig. 4. Light from a laser diode is directed to an FFPI and a laser power monitoring photodiode through a fiber coupler. An optical isolator is connected in serial with the laser to block the destabilizing optical feedback. The reflected light from the FFPI is converted by another photodiode to an electrical current signal $I_r$, such that the reflectance is obtained as $R_{FP} = CI_r/I_i$, with C a constant and $I_i$ the photocurrent measured by the laser power monitoring photodiode. The absolute value of $R_{FP}$ can be obtained through calibration, although it is often not necessary.

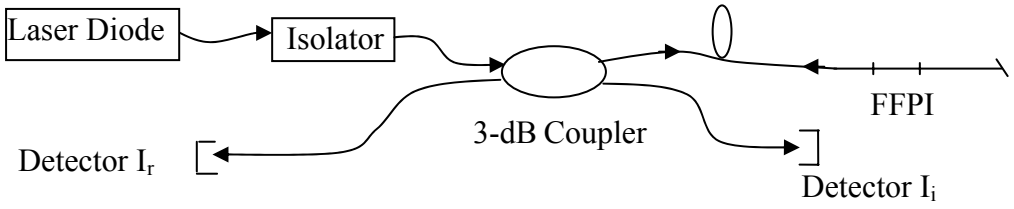


Fig. 4. Experimental arrangement for monitoring the reflectance of an FFPI sensor with a laser diode.

In the case that the laser is operated at constant bias current (cw condition), it is desirable to operate the interferometer at the quadrature point to get a quasi-linear dependence of reflectance on phase shift. Referring to Fig. 2, sensitivity null/ambiguity

points occur at maxima and at minima in the reflectance signal. Thus, the linear dynamic range of phase shift is limited << $\pi$ radians. [12,13]

One way to overcome the problems of sensitivity nulls and direction-of-change ambiguities in interferometric sensors is to modulate the frequency of the light source. In one case, the bias current to a distributed feedback (DFB) laser was ramped repetitively to produce a linear dependence of optical frequency on time (linear chirping), such that the reflectance signal from an FFPI is a temporal fringe pattern for each modulation cycle. The interferometer phase shift is determined from the time delay of the quadrature point relative to the beginning of a modulation cycle.[2] In a continuously monitoring mode, it is also possible to "count fringes" with aid of software. Thus, a phase shift can be accurately measured through many $\pi$ radians.

### 2.4.2. Broadband light source

Broadband light source interferometry, often referred as "white light interferometry" (WLI), is commonly used for FFPI sensing. In this case, the spectral width of the light source is sufficiently large that its coherence length is much less than the round-trip optical path of the FFPI. Suitable light sources for WLI include semiconductor superluminnescent diodes (SLDs), light emitting diodes (LEDs), and amplified spontaneous emission (ASE) light of erbium-doped fiber amplifiers (EDFAs). These light sources typically have a spectral width of a few tens of nm.

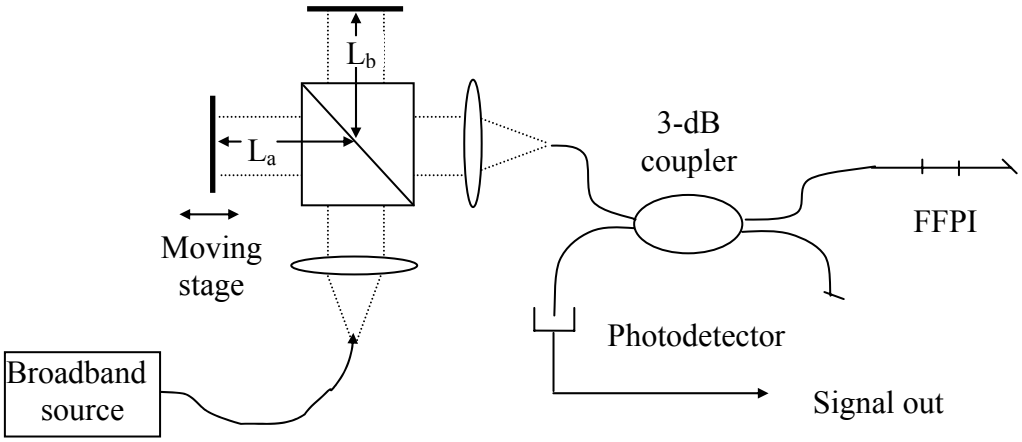


Fig. 5. White light interferometry for monitoring the optical path difference of an FFPI.

In an example of WLI shown in Fig. 5, light from the broadband source is transmitted by a reference Michelson interferometer and then reflected by a sensing FFPI before reaching the photodetector.[14] The Michelson interferometer can be replaced with a Mach-Zehnder interferometer[3] or a Fabry-Perot interferometer.[15] With 2nL the optical path difference (OPD) of the sensor interferometer, and 2nL+Δ the OPD of the reference interferometer, the photodetector output is given as a function of the OPD mismatch as

$$I(\Delta) = C + \eta \int_0^\infty g(\nu) \cdot \cos(\frac{2\pi(2nL+\Delta)}{c}\nu) \cdot \cos(\frac{4\pi nL}{c}\nu) \cdot d\nu, \qquad (2.7)$$

where C and $\eta$ are constants and $g(\nu)$ is the spectral density of the light source. In the case that $g(\nu)$ satisfies a Gaussian distribution, eq. (2.7) becomes [3]

$$I(\Delta) = C + \eta P[1 + \frac{1}{2}\cos(\frac{2\pi\Delta\nu}{c})\exp(-\frac{4\Delta^2}{L_c{}^2})], \tag{2.8}$$

with P the total power and $L_c$ the coherence length of the light source. In a sensor monitoring experiment, the OPD of the reference sensor is scanned such that the scanning range includes the OPD of the sensor interferometer; i.e., so that the OPD mismatch, Δ, is changing in the vicinity of zero. As illustrated in Fig. 6, the photo current output is an interference pattern modulated by a Gaussian envelope function profile, and the maximum amplitude (peak fringe) occurs when Δ=0. The width of the interference pattern is proportional to the coherence length of the light source. A change in the OPD of the sensor causes a lateral translation of the fringe pattern. Thus, the exact OPD change is determined by the shift of central fringe peak. Identification of the central fringe is a key issue, because even with a minimum noise, the central fringe is barely distinguishable from adjacent fringes in term of amplitude. A mistaken central fringe identification leads to an error in OPD of at least one wavelength. An approach using two broadband light sources with a wide wavelength separation has considerably reduced the chance of central fringe error by improving the fringe amplitude contrast.[16,17]

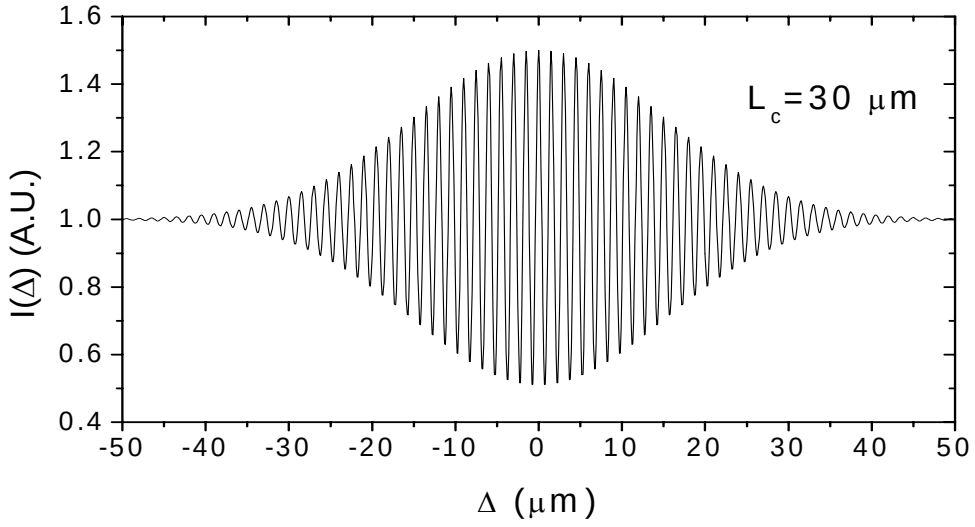


Fig. 6. Interference pattern of a white light interferometer.

## 2.5. Multiplexing techniques

Sensor multiplexing provides a means to reduce the number of expensive components and hence the overall system cost. Space division multiplexing, time division multiplexing and coherence multiplexing can be utilized with FFPI sensors.

### 2.5.1. Space division multiplexing

Fig.7 shows a typical configuration for space division multiplexing. Light from a continuous wave (cw) source is directed to each sensor through a multi-port directional coupler and the reflected light signal is measured by separate photodetectors. A signal processor utilizes the photodetector signals to determine a measurand value for each sensor. Monitoring up to 32 extrinsic Fabry-Perot interferometer (EFPI) sensors with two broadband light sources operating at different wavelengths was reported.[18] With a

similar physical configuration, a single DFB laser and one mirocontroller-based processor can monitor up to 24 FFPI sensors.[1]

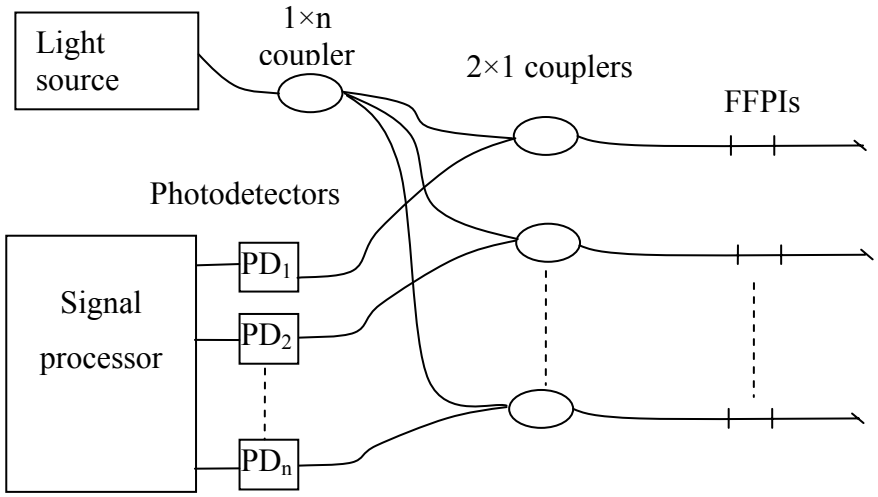


Fig. 7. Space division multiplexing configuration monitoring multiple FFPIs with a single processor.

### 2.5.2. Time division multiplexing

In a time-division multiplexing configuration, fiber delay lines of different length are deployed between a transmitter and receiver. When a laser pulse is transmitted, the reflected light pulses from each of the accessed sensors reaches the photodetector in different time slots via fiber delay lines of different length. To determine the measurand value for one specific sensor, the reflected signal is sampled for analog-to-digital conversion at fixed time delays relative to the start of the pulse, and the samples are averaged.

### 2.5.3. Coherence multiplexing

As an example of coherence multiplexing, the WLI monitoring configuration of Fig. 5 is extended to the interrogation of FFPI sensors of different length connected along a linear bus. Light from the broadband source is transmitted by a reference interferometer before reaching the sensors. When the reference interferometer is scanned, separated interference patterns are observed, and one local fringe peak is located for each sensor. The location of the fringe peaks determines the measurand value for each sensor. In an experiment using a quartz halogen lamp as the light source and scanned Michelson reference interferometer, 6 EFPI strain sensors of different optical cavity lengths were multiplexed in series along the length of a single mode fiber.[19]

## 2.6. Summary

In this chapter we have reviewed the theory of the Fabry-Perot interferometer, and introduced FFPI sensors formed with two low reflectance dielectric mirrors inside a single mode fiber. The OPD change of FFPI sensors can be optically interrogated using a laser which emits at a single wavelength or a broadband light source. The laser approach has the advantage of high-speed measurement but generally cannot provide accurate reading from “cold start” and the unambiguous range is limited. The broadband light source approach provides an absolute OPD measurement over a large dynamic range. FFPI sensors are also amenable to space division, time division and coherence multiplexing.

# III. FIBER BRAGG GRATING AND ITS APPLICATIONS

## 3.1. Fiber Bragg grating (FBG) fundamentals

An FBG is a section of single mode fiber in which the refractive index varies along the fiber axis in a periodic manner. This index modulation is normally produced by exposure of the fiber core to an intense optical interference pattern from an ultraviolet laser.[4,21] Due to the coherent scattering from the index variations, a strong reflection occurs at the Bragg wavelength $\lambda_B$ , which is given by

$$\lambda_B = 2n_{eff}\Lambda, \tag{3.1}$$

where $n_{eff}$ is the effective refractive index and $\Lambda$ is the grating period. Fig. 8 shows that an FBG acts as a wavelength stop-band filter when monitored in transmission and as a band-pass filter when monitored in reflection.

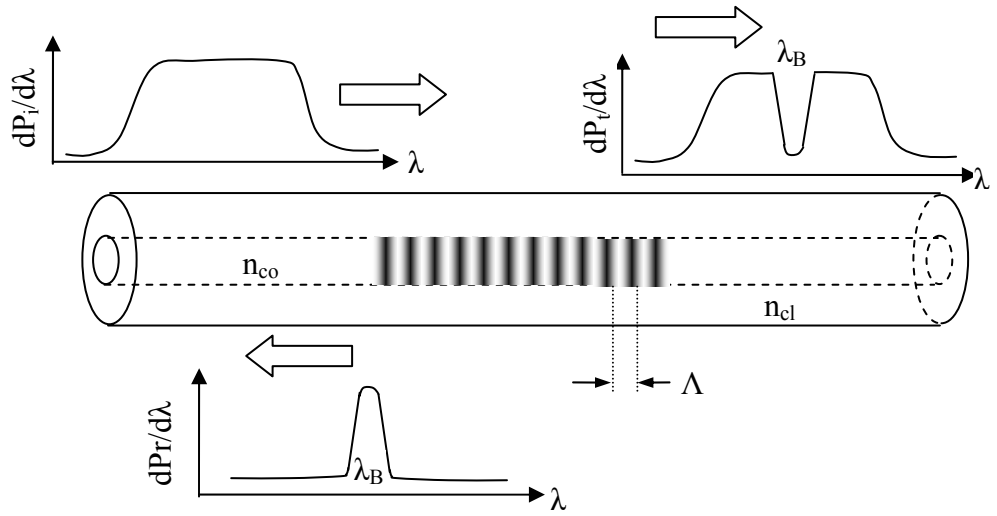


Fig. 8. FBG as a band reflecting filter, with $P_i$, $P_t$ and $P_r$ the incident, transmitted, and reflected power, respectively.

For a uniform Bragg grating formed within the core of single mode fiber, the refractive index of the fiber core can be expressed as

$$n(z) = n_{co} + \Delta n \cos(\frac{2\pi\ z}{\Lambda}), \tag{3.2}$$

where $\Delta n$ is the amplitude of the induced index modulation (typical values are in the range of $10^{-5}$ to$10^{-3}$), and the z axis is along the fiber core. The reflectance of such an FBG is given from the coupled mode theory as[22]

$$R(k) = \frac{\Omega^2 \sinh^2(sL)}{\Omega^2 \cosh^2(sL) - \Delta k^2}, \tag{3.3}$$

where L is the grating length; $k = 2\pi n_{eff} / \lambda$ is the wavevector, and the wavevector detuning is defined as

$$\Delta k = k - k(\lambda_B) = k - \pi / \Lambda; \tag{3.4}$$

$\Omega$ is the coupling coefficient, and the complex variable $s$ is defined as $s^2 = \Omega^2 - \Delta k^2$. The coupling coefficient is given by

$$\Omega = \frac{\pi \Delta n}{\lambda} M_p, \tag{3.5}$$

where $M_p$ the fraction of the fiber mode power inside the fiber core can be approximated as

$$M_p = 1 - \frac{\lambda^2}{4a^2\pi^2(n_{co}^{\ 2} - n_{cl}^{\ 2})}, \tag{3.6}$$

with a the core radius and $n_{cl}$ the cladding refractive index. Following from eq. (3.3), the peak reflectance at the Bragg wavelength is given as

$$R(\lambda_B) = \tanh^2(\Omega L). \tag{3.7}$$

Noting that $s$ can be real or imaginary, eq. (3.3) is expressed as following when $s$ is imaginary,

$$R(k) = \frac{\Omega^2 \sin^2(|\ s\ | L)}{\Delta k^2 - \Omega^2 \cos^2(|\ s\ | L)}. \tag{3.8}$$

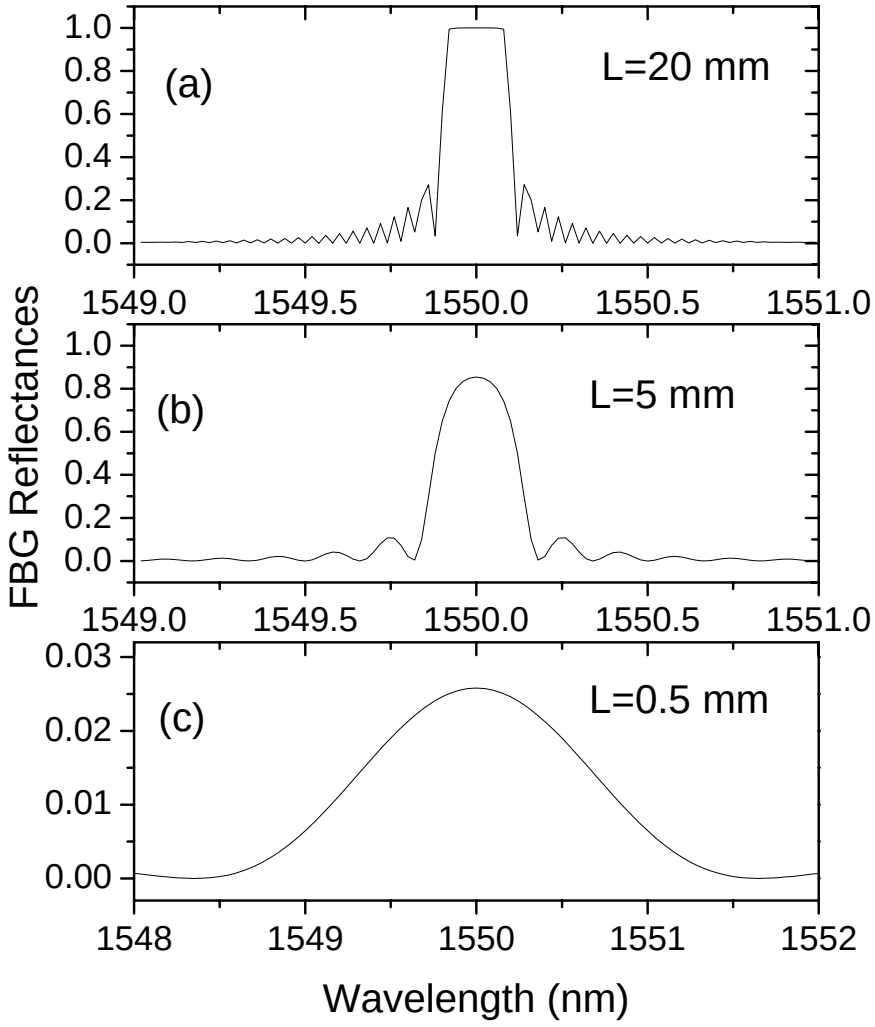


Fig. 9. Calculated FBG reflectance spectra in different grating lengths.

The FBG reflectance spectrum given by eq. (3.3), with $\Delta n$ =$2\times10^{-4}$ and $\lambda_B$=1550 nm, is plotted in Fig. 9. Fig. 9 (a) shows a spectrum for a 2-cm long grating with a flat high reflectance band, which is normally used in dense wavelength division multiplexing (DWDM) as an add-drop filter or demultiplexer. The sidelobes of the

reflectance profile can be removed by modifying the uniform index modulation with an apodized index modulation envelope.[23] Figs. 9 (b) and (c) show that an FBG with a short length has lower reflectance and a more gradually changing profile. The grating with the reflectance spectrum in Fig. 9 (c) can be used as one reflector in a low finesse Fabry-Perot interferometer.

### 3.2. FBG in optical communication applications

FBGs are used in a variety of optical communication components. Their unique filtering property and versatility as in-fiber devices are applied in wavelength stabilized lasers, fiber lasers, remote pump amplifiers, Raman amplifiers, phase conjugators, wavelength converters, passive optical networks, wavelength division multiplexers and demultiplexers, add/drop multiplexers, dispersion compensators, and gain equalizers.

#### 3.2.1. Wavelength stabilizer

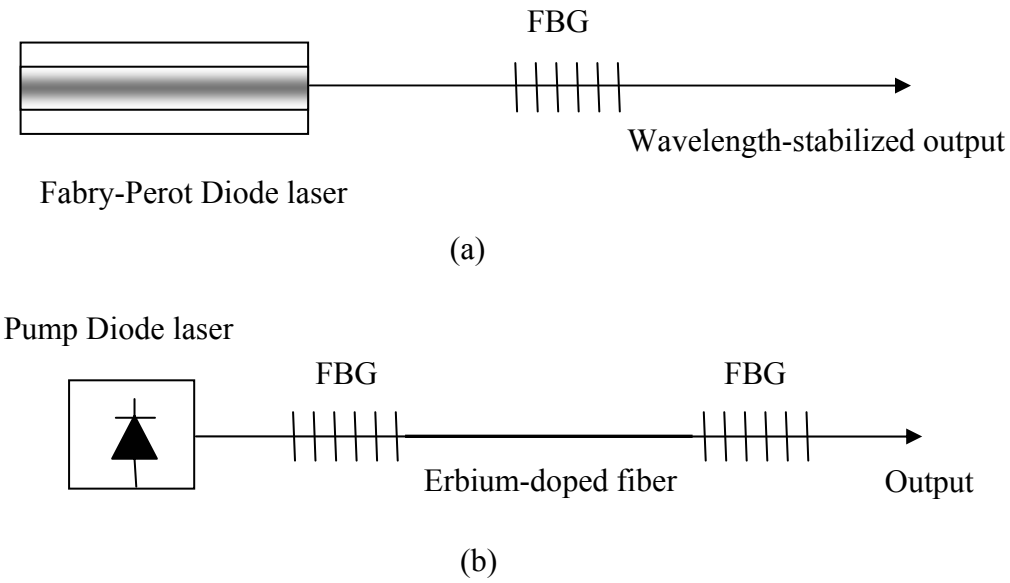


Fig. 10. The FBG as a wavelength selective reflector for (a) a wavelength stabilized pump laser; (b) an all-fiber laser.

FBGs are commonly used as feedback reflectors in wavelength stabilized 980 nm semiconductor lasers for erbium-doped amplifiers.[24, 25] As shown in Fig. 10 (a), laser stabilization is achieved using a weak, narrow-band FBG in the fiber pigtail to couple light back into a Fabry-Perot semiconductor pump laser, creating an external laser cavity. Shown in Fig. 10 (b), all-fiber lasers can be constructed using FBGs as resonator mirrors and an erbium-doped fiber as the gain medium. Because of the short cavity length and the narrow bandwidth of the FBG reflectors, the laser is operated in a single longitudinal mode, such that the narrow laser linewidth is suitable as an externally-modulated cw source in a gigabit/s transmission system.[26]

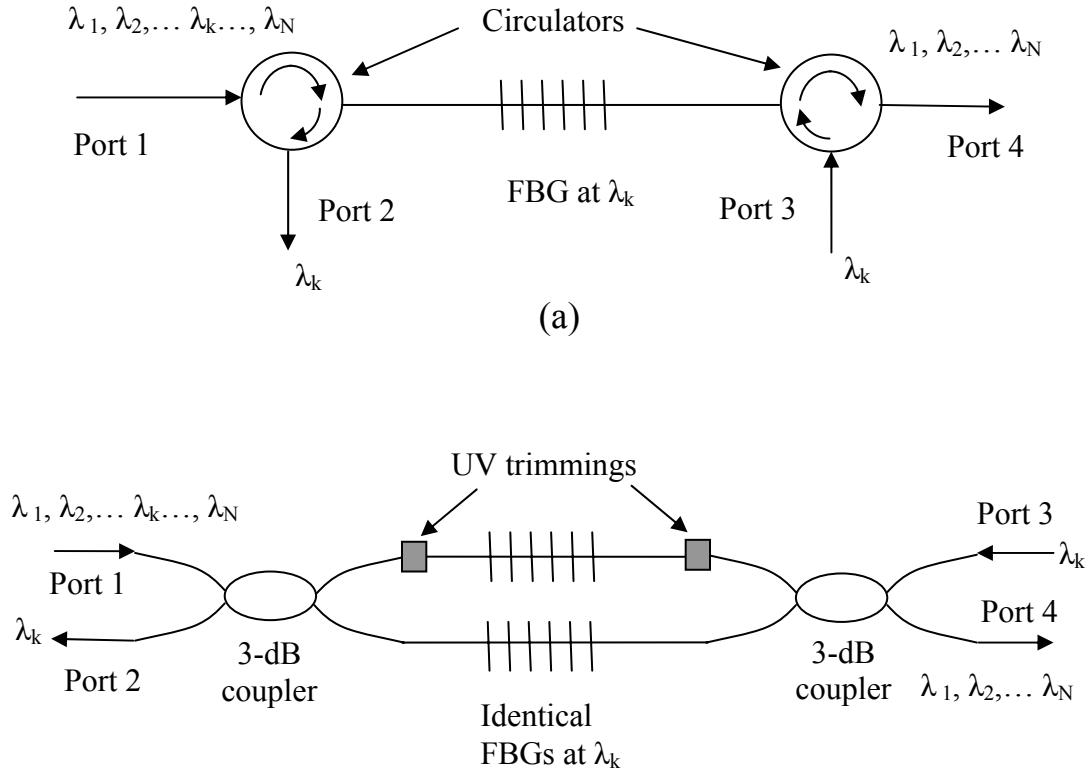


Fig. 11. FBG multiplexer/demultiplexer in (a) circulator arrangement, (b) Mach-Zehnder interferometer arrangement.

### 3.2.2. Add/drop filter

There are several techniques to make use of an FBG in an add/drop filter. One of the most straightforward methods is to connect an FBG with circulators as shown in Fig. 11(a). With port 1 as the input port, the wavelength channel reflected by the FBG is transmitted through port 2, and a new signal in this channel can be added through port 3. Commercial circulators have very high port-to-port isolation (typically 50-60 dB) and thus give the filter excellent wavelength isolation and return loss. The disadvantage of this configuration is relatively high insertion loss and high price of the circulators. Fig. 11 (b) shows another approach in which a Mach-Zehnder interferometric arrangement is formed with two 3-dB coupler and two identical FBGs. With port 1 as the input port and port 3 as the add port, it is possible to adjust the phases of the reflected and transmitted signals such that interferometric maxima are produced at port 2 and port 4. As a result of the symmetry of the device, multiplexing and demultiplexing can take place simultaneously in the same device. A monolithic version of this device can be fabricated without fiber splicing. Two fibers are laid parallel so the fused couplers are formed and then identical FBGs are written.[27] Accurate phase adjustment is accomplished by exposing one arm of the interferometer to UV light to produce refractive index changes.

### 3.2.3. Dispersion compensator

Chromatic dispersion in a transmission fiber can cause significant distortion of optical pulses, leading to system power budget and bandwidth penalties. Dispersion compensation can be accomplished by using a long chirped FBG where the periodicity of the grating decreases continuously along the length of the grating.[28] As shown in Fig. 12, longer wavelengths are reflected from the front of the grating, whereas the shorter wavelengths penetrate farther into the grating before being reflected. The wavelength-dependent time delay of the reflection compensates for the pulse broadening resulting from propagation of the light over the long fiber.

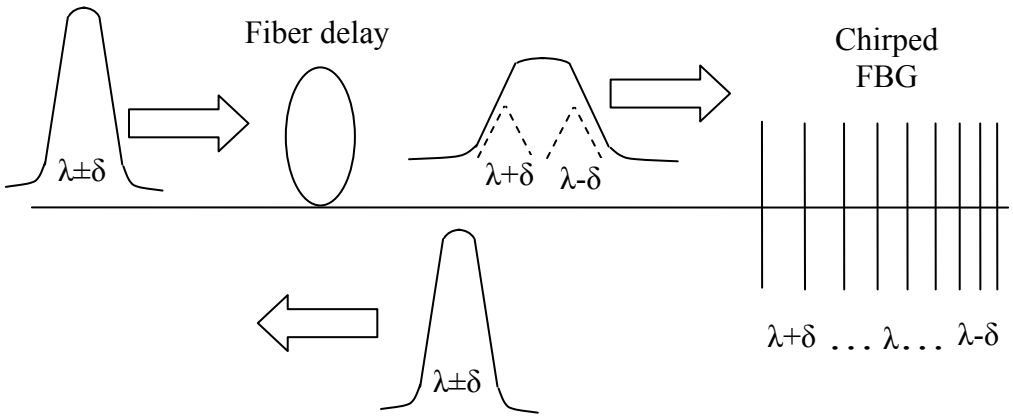


Fig. 12. Chirped FBG used to compensate for the dispersion of an optical pulse.

### 3.3. FBG sensors and interrogation methods

The FBG is an excellent sensor element, suitable for measuring static and dynamic fields, such as temperature, strain, and pressure.[29] The principal advantage is that the measurand information is wavelength-encoded (an absolute quantity), thus a system incorporating FBGs as sensor elements is potentially interrupt-immune. In addition, their low insertion loss and narrow reflection bandwidth allows for WDM multiplexing/demultiplexing techniques to be applied to an array of FBGs along a single optical fiber. Combined with other advantages of intrinsic fiber sensors, such as immunity to electromagnetic interference (EMI), light weight, flexibility, stability, high temperature tolerance and durability, the FBG is a strong candidate for use in smart structures.

The most commonly used monitoring technique in an FBG-based sensor system is based on determining the Bragg wavelength which shifts with the changes in the

measurand (e.g. strain, temperature). From eq. (3.1), the Bragg wavelength is a nearly linear function of temperature or strain as indicated by the following expressions:[29]

$$\frac{1}{\lambda_B}\frac{\delta\lambda_B}{\delta T} = 6.67\times10^{-6}\ /^{O}C\,, \tag{3.9}$$

$$\frac{1}{\lambda_B}\frac{\delta\lambda_B}{\delta \varepsilon} = 0.78\times10^{-6}\ /\ \mu\varepsilon\,. \tag{3.10}$$

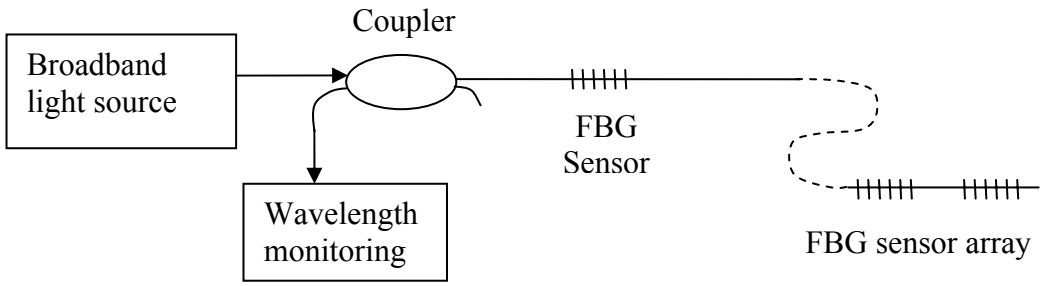


Fig. 13. Monitoring and multiplexing of FBG sensors using a broadband illumination arrangement.

The most frequently utilized method for the interrogation of an FBG sensor is based on a passive broadband illumination arrangement. The input light source has a broad spectrum, and either the narrowband component reflected by the FBG is directed to a wavelength detecting device, or the transmitted spectral with Bragg "notch" is analyzed. Fig. 13 shows the general arrangement for the reflective approach. The broadband light source is often a SLED or the amplified spontaneous emission (ASE) light of an Erbium-doped amplifier, with a bandwidth in the tens of nm range. A commercially available optical spectrum analyzer (OSA) can be used as a wavelength monitoring device, such that the measured Bragg wavelength resolution approaches ~1 pm, which is required to resolve a temperature of ~0.1 $^{o}$C and a strain change of ~1 με. However, it is a more challenging goal to measure the spectrum using small electro-

optic devices. Various wavelength detecting techniques such as edge filters, scanning filters, and interferometers have been demonstrated.

### 3.3.1. Edge filter approach

In a ratiometric approach based on the use of a broadband light source, the FBG wavelength is determined by comparing the transmittance of the FBG-reflected light through a filter with the transmittance of light which passes through a direct reference path.[30] Edge or bandpass filters provide a suitable wavelength-dependent loss for this type of detecting system. A wavelength resolution of ~5 pm, corresponding to 5 μs or 0.5 $^{o}$C in strain and temperature respectively, has been achieved using a fiber WDM coupler as the filter.[31] The wavelength detecting arrangement is shown in Fig. 14. The multiplexing of sensors using this approach has yet to be addressed.

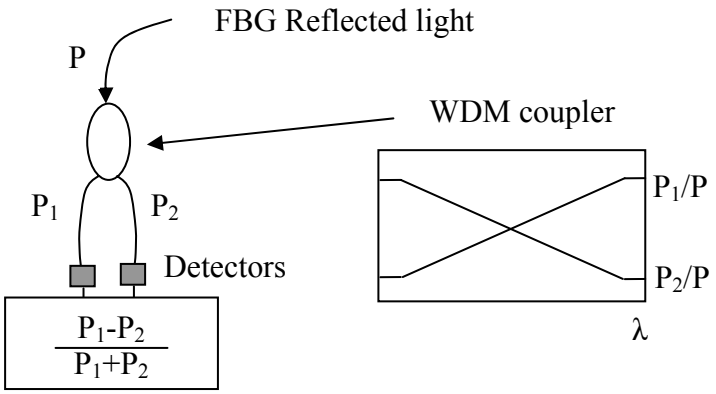


Fig. 14. Using a WDM coupler to determine the Bragg wavelength.

### 3.3.2. Scanning filter approach

FBG wavelength monitoring has also been demonstrated using scanning filters such as tunable Fabry-Perot (FP),[32] acousto-optic tunable filter (AOTF),[33] and Bragg

grating-based filter.[34] When using an FP filter, the light reflected by the FBG is returned via the coupler to the scanning filter and to a detector. The FP passes a narrowband wavelength component, depending on the spacing between the two mirrors. Electrical control of this mirror spacing via a piezoelectric stack allows for tuning the pass band wavelength. Typical characteristics of this type of FP used are a free spectrum range (FSR) of 50 nm and bandwidth of ~0.3 nm. This allows as many as 16 FBG sensors spaced by ~3 nm to be multiplexed in a serial configuration. A 16-bit digital-to-analog converter generates the control voltage for the FP and produces a minimum wavelength resolution of ~0.8 pm. An FP scanning rate of >300 Hz also makes fast measurement possible. The impact of the piezo hysterisis and nonlinearity on the wavelength accuracy has yet to be addressed. The scanning filter technique also has the drawback that it only utilizing a narrow "slice" of optical spectrum during each scanning cycle. A strong erbium fiber ASE light source with average power in the range of 10 mw can be used to compensate for the extra power penalty.

### 3.3.3. Interferometer approach

In an interferometer wavelength detection approach, the FBG wavelength shift is converted into a phase change of the interferometer. Fig. 15 shows an asymmetric Mach-Zehnder interferometer arrangement as a wavelength detection device. As the phase in one interferometer arm is ramped over exact π radians, an electrical carrier is generated at the receiver. The output signal is band-pass filtered at the fundamental ramp modulation frequency, such that the phase modulation of the carrier can be detected using a lock-in amplifier. The dependence of the output phase change on Bragg wavelength shift is given by

$$\Delta\phi = \frac{2\pi nd}{\lambda^2}\Delta\lambda\,, \tag{3.11}$$

where nd is the interferometer optical path difference (OPD).

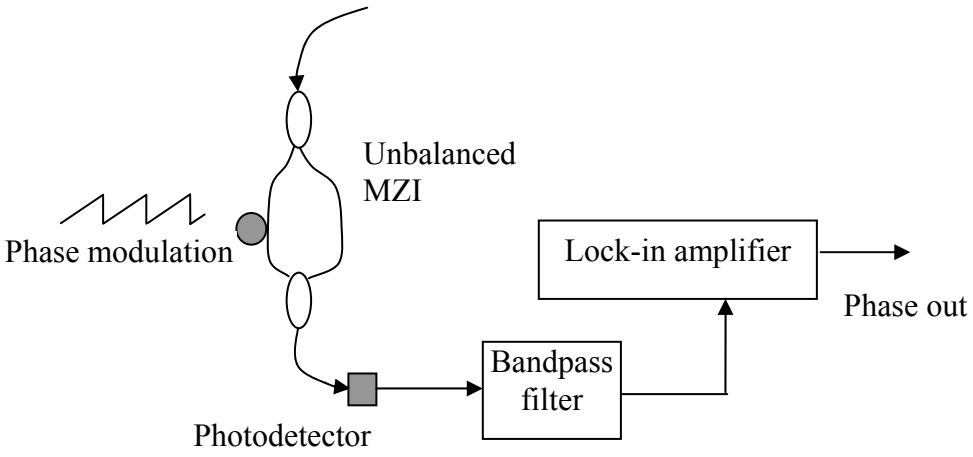


Fig. 15. Mach-Zehnder interferometer arrangement for wavelength detection.

Since the temporal coherence has to be maintained as the light beams travels through the two interferometer arms, the OPD must be less than the effective coherence length of the light reflected from the FBG. By appropriate choice of the interferometer OPD, this technique can be extremely sensitive to a small dynamic wavelength shift. However, the detection of quasi-static strain is precluded by temperature-induced interferometer OPD drift and by the limited unambiguous range, corresponding to a phase change of $2\pi$ radians in the interferometer. Therefore, this technique is most suited for recovering dynamic strain signals, with the dynamic range limited to $<10^4$. A dynamic strain resolution of ~6 nanostrain/$\sqrt{\text{Hz}}$ has been reported for a 4.5 mm OPD interferometer.[35] A combination of WDM multiplexing and interferometric detection has also been demonstrated.[36] A drawback which exists in such a WDM system is that the phase modulation can not be exactly $2\pi$ radians for all the FBG sensors. This leads to a cyclic phase error which has yet to be addressed.

### 3.4. Summary

An FBG is formed by a spatially periodic refractive index modulation inside a fiber core, such that a strong reflection band is produced near the Bragg wavelength. The wavelength response of an FBG is calculated using mode coupled theory. Numerical results have been given for particular FBG parameters including: Bragg wavelength, index modulation depth and grating length.

FBG applications in communication have been illustrated. An FBG is used as a selective wavelength feedback element for wavelength stabilizing a pump laser diode and for constructing a narrow linewidth fiber laser cavity. The FBG is also a very important element for many DWDM multiplexing/demultiplexing devices. A circulator configuration and a Mach-Zehnder interferometer arrangement for an add-drop multiplexer/demultiplexer have been described. A chirped FBG can be used to compensate for the chromatic dispersion of a fiber used for long-haul transmission.

The FBG is a very important sensor element. Compared to interferometric fiber sensors, the measurand information is wavelength-encoded, such that a direct absolute measurement is available, and WDM multiplexing/demultiplexing is readily implemented. A passive broadband illumination arrangement is commonly used in FBG interrogation. Besides using the commercially available optical spectrum analyzer (OSA), methods using other small electro-optic devices have been illustrated. The edge filter approach is based on the principle of detecting the wavelength dependent transmission through the filter. It provides a simple solution with good resolution and instantaneous measurement, but the measurement range and the multiplexing capability is limited. Scanning filters are successfully used for FBG sensor interrogation. A piezo driven Fabry-Perot tunable filter is shown as an example. The wavelength resolution is excellent and the system is able to multiplex an array of many FBGs along a single fiber. Finally, an interferometric approach is introduced. Although this method relinquishes absolute measurement by converting wavelength detection into phase detection, extremely high resolution is obtained. An interferometer normally suffers

from slow drift, so this technique is suited for high resolution dynamic strain measurement, but not for absolute parameter measurement. Multiplexing can also be combined with this approach.

# IV. LINEARLY CHIRPED ERBIUM-DOPED FIBER LASER

## 4.1. Erbium-doped fiber

The Erbium-doped fiber has found wide applications as the gain medium for Erbium-doped fiber amplifiers (EDFAs). Since it is able to compensate for the optical signal attenuation which occurs during long distance fiber transmission, the EDFA repeater plays an exceptionally important role in supporting the backbone of the optical fiber communication networks since its invention in late 1980s. Compared to electronic regenerators, EDFAs are more versatile and intrinsically reliable, and much less expensive. With a wideband gain spectrum centered at 1550 nm wavelength, the EDFA can simultaneously amplify > 100 wavelength channels in a single fiber.

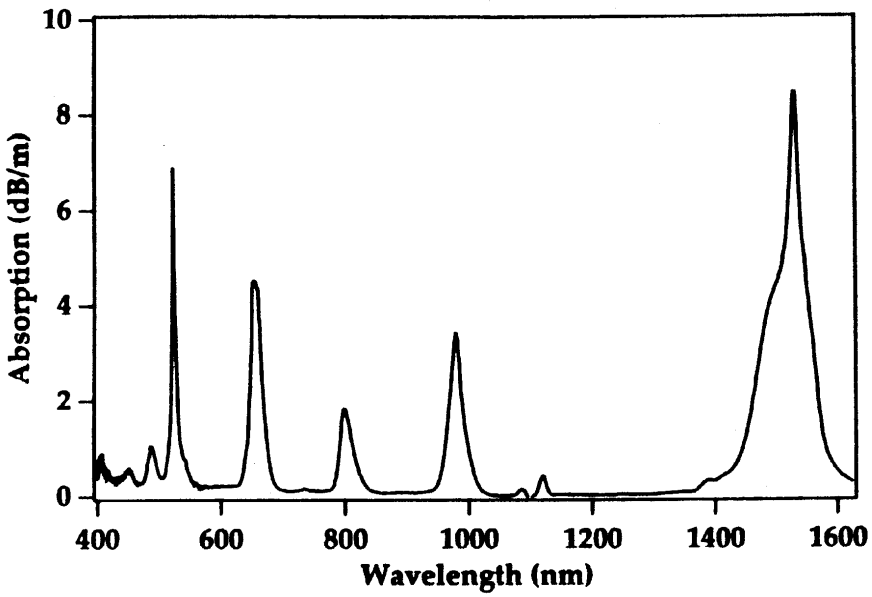


Fig. 16. Absorption spectrum of erbium-doped fiber.

Fig. 16 shows the absorption spectrum measured in an erbium-doped fiber, where the peaks represent the transitions between the $Er^{3+}$ ion $^4I_{15/2}$ ground energy level and higher energy levels.[37] Two main spectral regions near 1480 nm and 980 nm with strong absorption are potential pump bands. The $^4I_{15/2} \rightarrow {}^4I_{11/2}$ transition is responsible for the pump absorption at 980 nm and the $^4I_{13/2} \leftrightarrow {}^4I_{15/2}$ transition is responsible for pump absorption at 1480 nm and emission in the 1550 nm wavelength region.

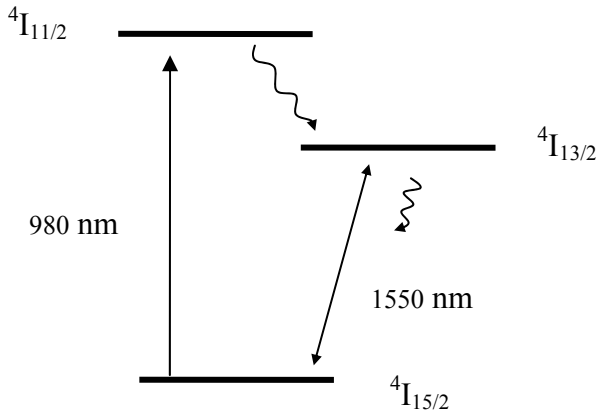


Fig. 17. $Er^{3+}$ ion energy level diagram with presence of 980 nm pumping.

In the 980 nm pumping case, the energy levels can be treated as a three-level energy system. Fig. 17 shows the energy level diagram with transition actions. The lifetime of the $Er^{3+}$ $^4I_{13/2}$ level is about $10^{-2}$ s.[37] The transition from the $^4I_{11/2}$ level is considerably faster with a transition rate in the order of $10^{-5}$ s.[38] Therefore, the population inversion can be built between the $^4I_{13/2}$ level and the $^4I_{15/2}$ ground level. It is reasonable to neglect the ion population in the $^4I_{11/2}$ level due to the fast transition to the level of $^4I_{13/2}$, thus the rate equation is given

$$d(N_2-N_1)/dt= \beta\sigma_1 N_1+ \rho\sigma_2 (N_2-N_1)- \gamma N_2. \quad (4.1)$$

with $N_1$, $N_2$ the population in the level $^4I_{15/2}$ and $^4I_{13/2}$ respectively, $\sigma_1$ the absorption cross section at pump wavelength, $\sigma_2$ the absorption or stimulated emission cross section

at the signal wavelength, γ is the spontaneous emission rate, and β and ρ are the photon flux density of the pump light and signal light respectively.

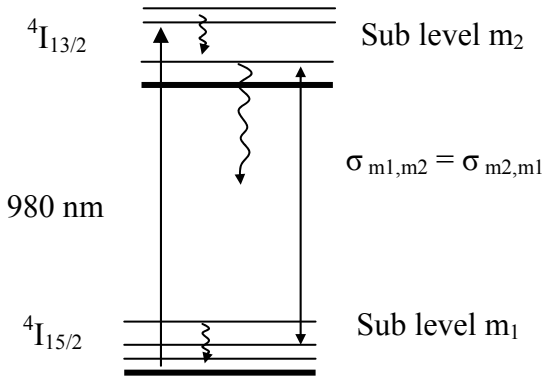


Fig. 18. $Er^{3+}$ ion energy level diagram with presence of 1480 nm pumping.

In the case of 1480 nm pumping, we have to consider the Stark splitting of the $^4I_{13/2}$ level and the $^4I_{15/2}$ level, because a population inversion is impossible to build for a pure two-level energy system. The energy diagram is shown in Fig. 18. According to the McCumber theory of emission,[39] the population in the sublevels is considered as the Boltzmann distribution, instead of equal distribution. The relationship between the emission cross section $\sigma_{21}$ and the absorption cross section $\sigma_{12}$ is thus written as

$$\sigma_{21}(\nu)=\sigma_{12}(\nu)\exp[(\varepsilon-h\nu)/kT], \qquad (4.2)$$

with ν is the optical frequency, ε the "mean" transition energy between the two energy levels of $^4I_{13/2}$ and $^4I_{15/2}$, k the Boltzmann constant. It indicates that the absorption and emission cross sections are equal only at one wavelength, ~1530 nm, and that for wavelengths lower than the crossing point, the absorption cross section is larger and vice versa for wavelengths larger than the crossing point. The McCumber analysis is verified by experiment.[40] Fig. 19 shows the measured and calculated cross sections for an erbium-doped from Miniscalco's and Quimby's work. The rate equation is given by

$$d(N_2-N_1)/dt = [\beta(\nu_{1480})\sigma_{12}(\nu_{1480})+\rho(\nu_{1550})\sigma_{12}(\nu_{1550})]N_1 \qquad (4.3)$$
$$-[\beta(\nu_{1480})\sigma_{21}(\nu_{1480})+\rho(\nu_{1550})\sigma_{21}(\nu_{1550})]N_2-\gamma\, N_2.$$

With the presence of pump light at 1480 nm, the population inversion between the excited state and the ground state is made possible for amplification in the 1550 nm wavelength region.

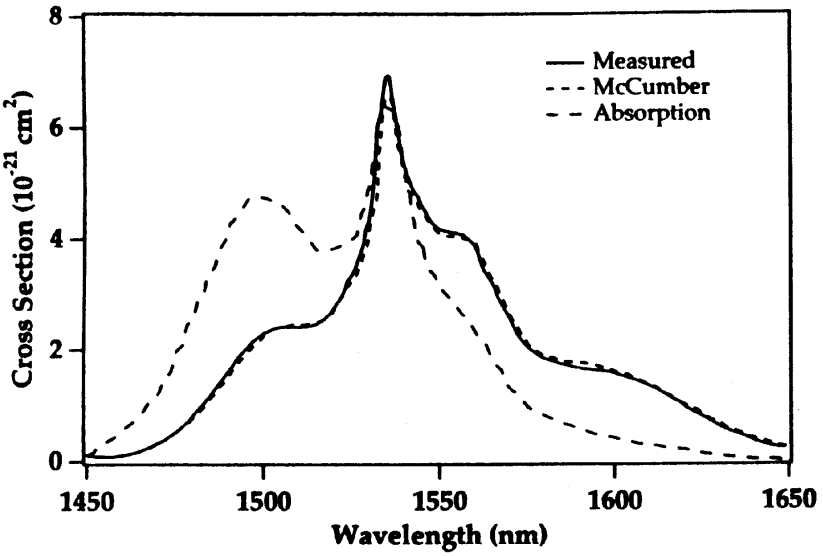


Fig. 19. Measured stimulated cross section agrees with the result using McCumber theory.

## 4.2. Erbium-doped fiber laser background

Neodymium doped crystal fiber lasers were investigated during the early 1970's as potential devices for fiber transmission.[41,42] Lasing at 1.06 μm wavelength was achieved for these devices. A laser is typically fabricated by polishing and coating the end face of the fiber and then aligning it to a pump laser diode or LED. In 1985, an $Nd^{3+}$ doped single mode fiber laser pumped by a GaAlAs laser diode was demonstrated.[43]

Shortly after the recognition of $Er^{3+}$ ion as an ideal amplifying medium for modern fiber-optic transmission system at 1.5 μm, the erbium-doped fiber laser (EDFL) was demonstrated. In an EDFL device, the Erbium-doped fiber is fusion spliced or connected with a fiber connector to standard single-mode fiber and other optical components such as a pump laser diode with fiber connection, coupler, isolator, tunable filter and polarization controller. Easily adaptable and versatile, the EDFL has become a very useful tool in the telecommunication and fiber sensing areas.

### 4.2.1. Ring type tunable EDFL

A tunable EDFL in a ring configuration is shown in Fig. 20, where the pump laser is normally a 980 nm or 1480 nm laser diode, and the Erbium doped fiber is about 15 m long.[44] An isolator is connected such that the light travels in one direction inside the laser cavity. In this case, the traveling wave cavity eliminates the "spatial hole burning" commonly existing in a standing wave cavity. When the laser is operated in a cw condition, the laser output is most likely in single longitude mode.[44] However, with the presence of environmental disturbance, special techniques have to be applied to keep the laser from mode hopping and frequency drifting.[45,46] Operated in a stable single mode condition, the laser linewidth is in the order of kHz. The tunable bandpass filter is connected so the laser wavelength can be tuned within the wide erbium-doped fiber gain spectrum span ranging from 1520 nm to 1570 nm. The tunable intracavity filter can be a Fabry-Perot etalon,[47] Mach-Zehnder interferometer,[48] ultra strength fiber Bragg grating (FBG),[49] acousto-optic tunable filter,[50] or bulky external cavity grating mirror.[44] Slope efficiency of 10%~15% is commonly achieved in this type of laser, which gives an output power in the order of mw. In general, the ring type EDFL offers many desired features such as: single mode operation and narrow laser linewidth, wide tuning range, and large output power.

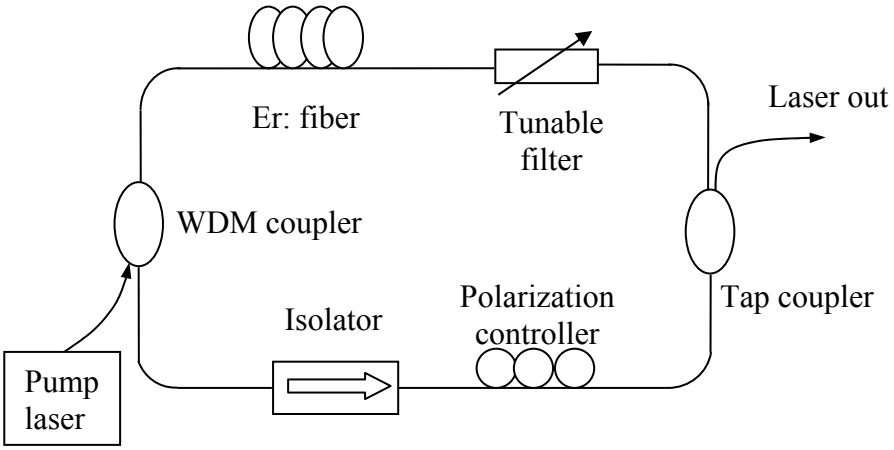


Fig. 20. Scheme of a ring type tunable Erbium-doped fiber laser.

However, continuous wavelength tuning has not yet been demonstrated in the ring type tunable lasers. According to the studies investigating mode hopping and mode competition during the wavelength transition of the ring type EDFL,[51,52] it is difficult to achieve continuous tuning.

### 4.2.2. Tunable EDFL with fiber Bragg gratings

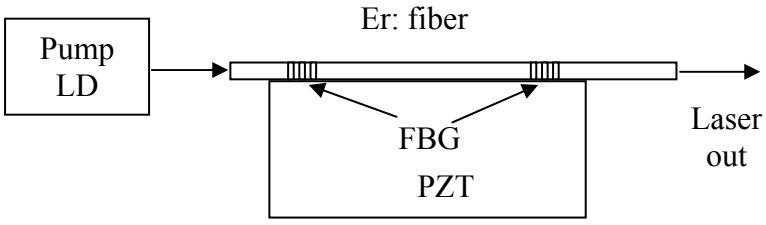


Fig. 21. Configuration of an EDFL with FBG reflectors.

Another popular tunable EDFL is built as a Fabry-Perot laser cavity with FBG reflectors.[53,54] The configuration is shown in Fig. 21. The cavity length is often a few cm long, such that the narrow reflection bandwidth of the FBGs only allows one single mode oscillation. Thus, the laser wavelength can be given as

$$\lambda = 4n_{eff} L/m, \tag{4.4}$$

with $n_{eff}$ the effective reflective index of the laser cavity, L the cavity length, and m the longitude mode order. The wavelength is tuned by applying tensile stress along the fiber laser cavity with a piezoelectric transducer (PZT). The center wavelength of an FBG reflector, also known as the Bragg wavelength, is given as in a similar form as

$$\lambda_b = 2n_b\Lambda, \tag{4.5}$$

where $\Lambda$ is the FBG grating pitch. Assuming that the refractive index change and fiber elongation of the FBG fiber and the erbium-doped fiber have the same dependence on the strain change, the Bragg wavelength will always track the laser wavelength, $\lambda_b \equiv \lambda$, thus allowing continuous tuning without mode hopping. However, the laser has two disadvantages:[53] 1. Because of the short Er: fiber, the output power is low; 2. The tuning range is limited to less than a few nm due to the fiber tensile strength and the limited strain a PZT can provide.

### 4.2.3. Comments

In most of these previous EDFL experiments, the goal has been to demonstrate and characterize lasers with wide spectral tunability and narrow linewidth as needed for dense WDM systems. However, these lasers can be applied in areas other than optical communications. In particular, the broad spectral tuning range makes these fiber lasers useful in spectroscopy, where a chirped laser can replace a broadband light source and optical spectrum analyzer. Ideally, the laser should be tuned continuously over the entire scanning range at constant rate, while a narrow instantaneous linewidth is maintained. The ring type and FBG approaches have not demonstrated this capability, because the former has difficulties in the continuous tuning mode and the later is limited by tuning range.

### 4.3. Constructing a tunable EDFL with a Fabry-Perot cavity

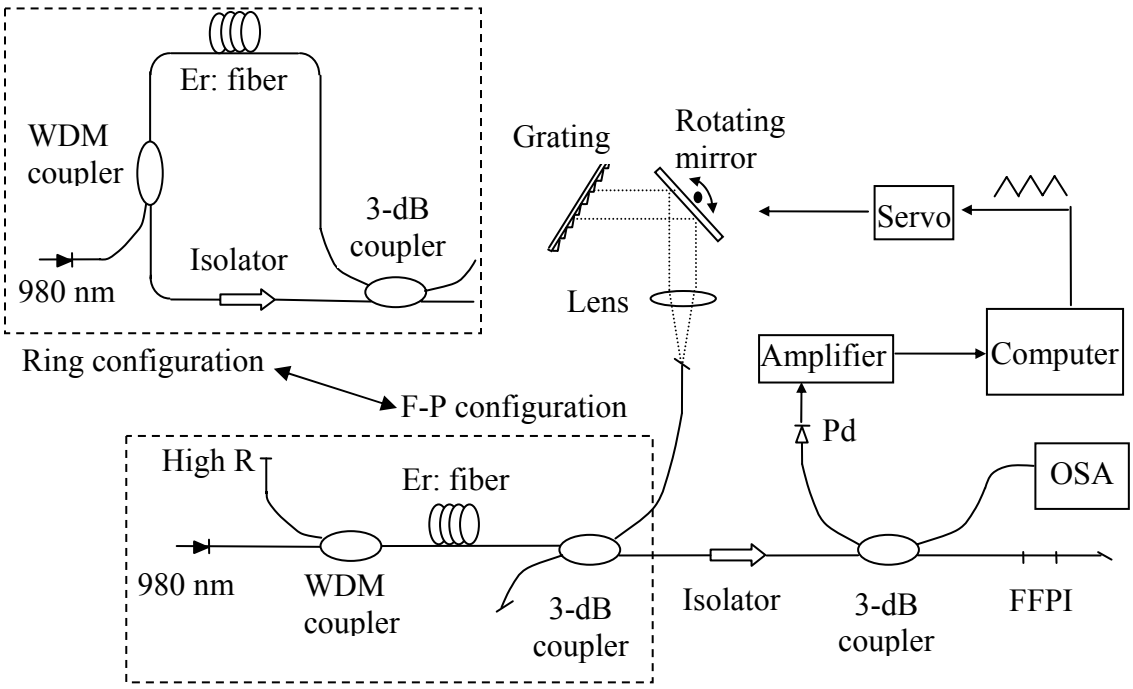


Fig. 22. Experimental arrangement of the tunable fiber laser. The Fabry-Perot laser cavity can be easily converted to a ring cavity.

The experimental arrangement of the tunable erbium-doped fiber laser is shown in Fig. 22. A 14-m long erbium-doped fiber is pumped by a diode laser emitting at 980 nm. A high-reflectance fiber mirror and a rotating mirror-grating combination in the Littrow configuration serve as reflectors for the Fabry-Perot laser cavity. The high-reflectance fiber mirror is formed by gold plating on a cleaved fiber, with a measured reflectance of 87%. In the mirror-grating combination, the light exiting from the fiber is first collimated by a lens with a focal length of 50 mm, and then reflected by a rotating mirror before it reaches the grating. The fiber end is angle polished and anti-reflection (AR) coated to eliminate back reflection and reduce loss. The 600 line/mm grating is

oriented at an angle of ~28 $^{o}$ relative to the input beam, such that the first order diffraction light will travel against the incident light propagation and be coupled back into the fiber, if the light wavelength satisfies

$$\lambda = 2d\sin\alpha, \tag{4.6}$$

with d the grating pitch, and $\alpha$ the incidence angle. The resolution of the first order diffraction equals the total number of grating lines illuminated by the light beam, given by

$$\delta\lambda/\lambda = d\cos\alpha/(f\theta), \tag{4.7}$$

where f is the lens focal length and $\theta$ the divergence angle of light exiting from the single mode fiber given by

$$\theta = 4\lambda/(\pi D), \tag{4.8}$$

with D the mode field diameter of the fiber. Combining eq. (4.5), (4.6), (4.7), the wavelength resolution is

$$\delta\lambda = 0.41D(4d^2-\lambda^2)^{-1/2}/f. \tag{4.9}$$

In the 1550 nm wavelength region, with a fiber mode field diameter of 9 μm, the minimum bandwidth of the grating mirror is 0.22 nm. When wideband light is sent to the grating mirror, the spectrum of the feedback light signal is measured with an optical spectrum analyzer (OSA). In , the 3-dB bandwidth is measured to be 0.32 nm.

The commercial rotating mirror used in the experiment is from Gsi Lumonics, model number M3. The mirror is driven by a DC servo motor with an embedded position sensor and an electronic feedback circuit. A Labview computer program generating a 1 Hz triangle waveform serves as the command signal, such that the mirror is scanning back and forth in a linear fashion. According to eq. (4.6), the mirror needs to turn ~1.0 $^{o}$ to scan over a 50 nm wavelength region near 1550nm. By adjusting the command signal amplitude, the laser wavelength is tuned over the entire erbium-doped fiber gain region.

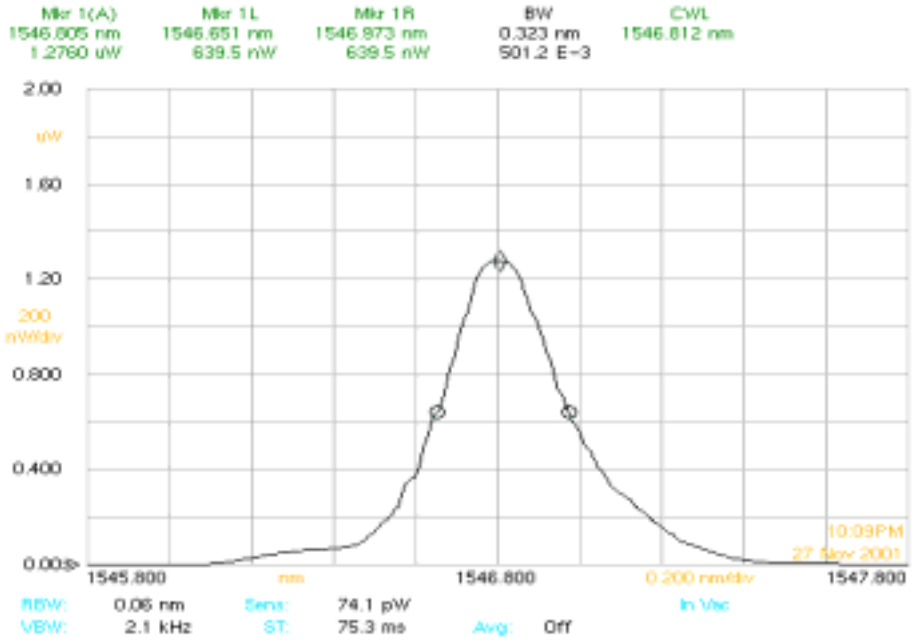


Fig. 23. Reflection spectrum of the mirror-grating combination.

As mentioned in section 2, the Fabry-Perot cavity laser is operated in multi longitude mode due to the "spatial hole burning" effect. Shown in Fig. 22, the laser cavity can be easily converted into a ring type such that the "spatial hole burning" effect can be eliminated. Single mode oscillation was confirmed in a very similar ring type laser.[44]

## 4.4. Monitoring the laser performance

### 4.4.1. Tuning range and laser power

Before the laser light reaches the OSA in Fig. 22, an isolator is connected to block any unwanted feedback. When the laser wavelength is scanned over the erbium-doped fiber gain region, temporal spectrum lines are captured by the OSA. Fig. 24 shows 5 traces of spectrum lines at different laser wavelengths and one trace of

spontaneous emission (laser-free) spectrum. Considering the laser power versus the total spontaneous emission power, the laser-noise ratio is >10 dB from 1521 nm through 1569 nm, and >25 dB from 1530 nm through 1561 nm. Additionally, the laser power variation is less than 2 dB over the 1521~1569 nm wavelength region. The OSA does not detect any light signal near the pump laser wavelength of 980 nm. Evidently, the 3-dB coupler and the isolator remove any unabsorbed pump light passing through the erbium-doped fiber.

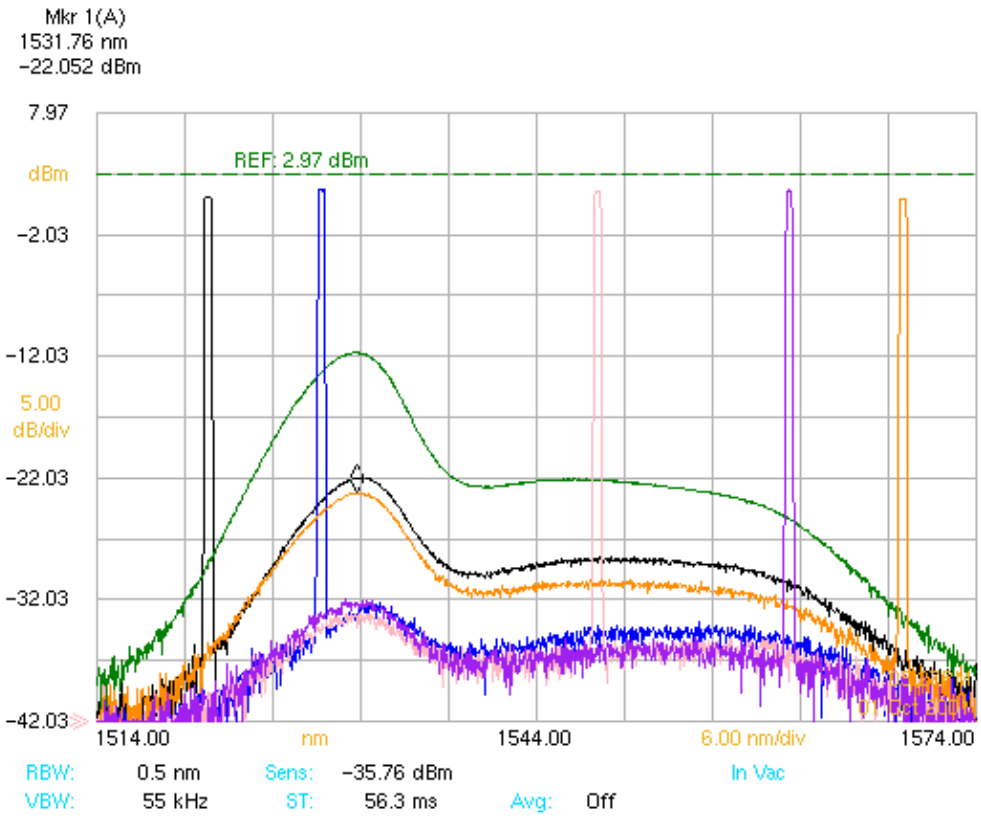


Fig. 24. Spectrum lines captured at 5 different laser wavelengths are compared to a spontaneous emission profile.

By replacing the OSA with a power meter, the laser power as a function of pump laser power is measured as shown in Fig. 25. The laser threshold and slope efficiency are found 13 mw and 20% respectively.

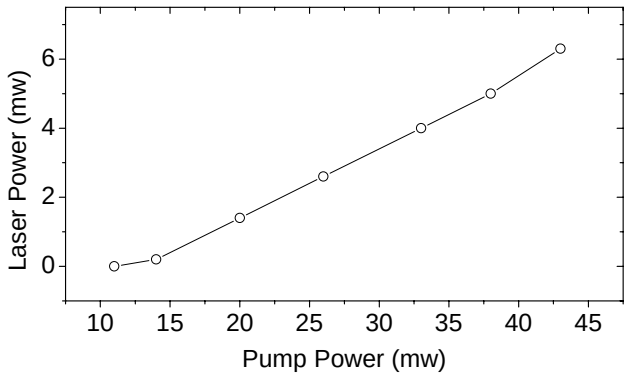


Fig. 25. Laser power as a function of pump power.

### 4.4.2. Continuous tuning

In Fig. 22, the laser is directed to a 10-mm long FFPI sensor, and a photodetector detects the reflected light signal. The photocurrent signal is converted to voltage by a transimpedence amplifier and a computer data acquisition program saves the voltage data. Fig. 26(a) shows the temporal variation of the reflected signal as the laser is scanned over a small portion (≈ 3 %) of the scanning, where the rotating mirror is scanned in a 1 Hz triangle waveform and the data acquisition sampling frequency is 20 kHz. According to the FFPI theory, the FFPI reflectance can be given as

$$R=C_1+C_2(1+\cos\phi), \tag{4.10}$$

with $C_1$, $C_2$ constants, and $\phi$ the FFPI round trip phase shift given as

$$\phi=4\pi nL\nu/c, \tag{4.11}$$

with n the index of refraction, L the FFPI cavity length, ν the optical frequency, and c the free space speed of light. The phase shift is calculated according to eq. (4.9). Shown in Fig. 26(b), the phase shift curve indicates that the laser frequency shifts linearly with little discontinuity. It follows from eq. (4.10) that the frequency change for $2\pi$ phase shift in the interferometer output signal is c/(2nL). With c = 3 x 10 m/s and n = 1.46, the frequency change per fringe is calculated to be 10.3 GHz, corresponding to a wavelength change of 78 pm.

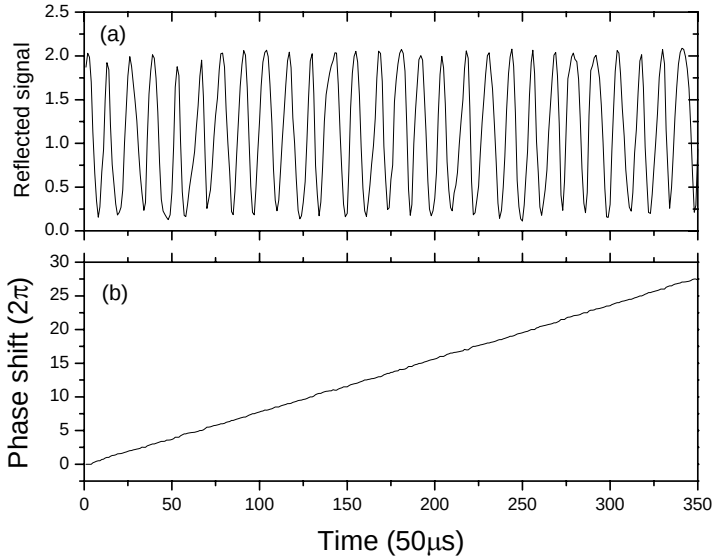


Fig. 26. (a) Reflected signal of the FFPI, (b) phase shift of the FFPI.

To further demonstrate the tuning continuity of the laser, a ring cavity laser operated in single longitudinal mode was constructed for comparison. As shown in Fig. 22, the laser cavity conversion can be easily done by connecting an isolator and closing the fiber loop. When the laser is operated in the same condition (i.e. pump power and tuning speed), it produces much larger wavelength noise such that the FFPI interference pattern can not be clearly identified. The reflected signal obtained by replacing the 10-

mm FFPI with a 2.5-mm long FFPI is shown in Fig. 27, which also plots the monitored laser output power signal. Notice that each fringe corresponds to ~0.31 nm in wavelength, the laser wavelength randomly hops in steps of 20~40 pm, and relaxation oscillation is occasionally present.

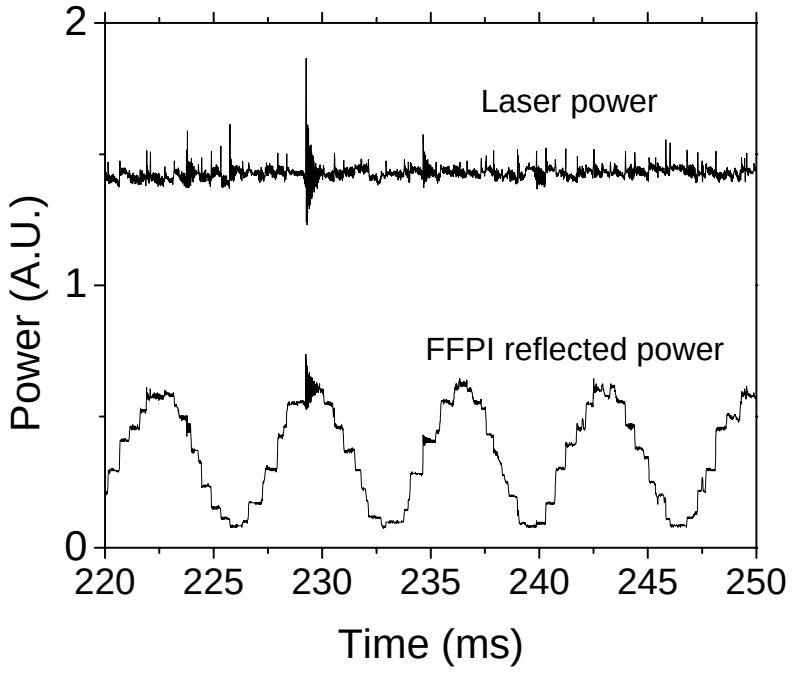


Fig. 27. In ring cavity configuration, the laser power and FFPI reflected signal as a function of time.

When the ring cavity laser operates in steady condition (i.e. the mirror is at fixed angle position), only one oscillating mode survives the mode competition. When the mirror is scanning, the cavity loss continually breaks the mode competition balance, such that the wavelength shifting is achieved by mode "hopping". In addition, the mode hopping carries random noise because it is very sensitive to many factors, including cavity loss, mode distribution and population inversion. On the contrary, the Fabry-

Perot laser cavity allows a large number of modes to oscillate simultaneously, such that the mean wavelength closely follows the minimum cavity loss wavelength with less noise. In conclusion, the Fabry-Perot cavity configuration has the advantage over a ring cavity configuration to produce continuous wavelength tuning.

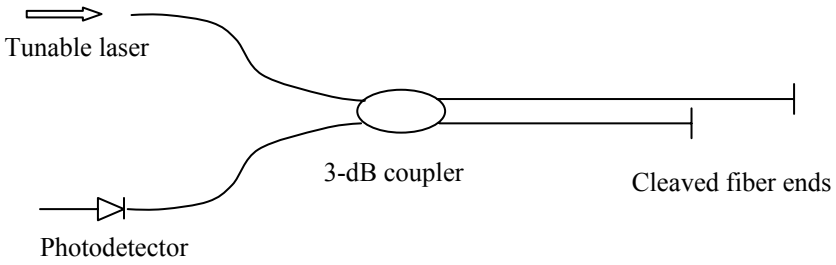


Fig. 28. Arrangement to measure the coherence length of the tunable laser.

### 4.4.3. Linewidth

Another important characteristic of the laser is the instantaneous linewidth during a spectral scan. Fig. 28 shows an arrangement to measure the coherence length of the laser light. The two fibers of a 3-dB coupler are cleaved to construct a Michelson interferometer. The visibility was measured using a fiber Michelson interferometer in which the OPD was varied by reducing the length of one of the arms by a cut-back technique.[1] The fringe visibility V, defined for equal-reflectance fiber ends as

$$V= (P_{max}-P_{min})/(P_{max}+P_{min}), \qquad (4.12)$$

with $P_{max}$ and $P_{min}$ the maximum and minimum optical powers within a fringe, is plotted as a function of OPD in Fig. 29. From this plot, the coherence length of the laser was determined to be 4.7 cm, corresponding to a spectral line width of 33 pm. Since the

longitudinal mode spacing is about 5.2 MHz, the laser is emitting in about 800 longitudinal modes at any given time.

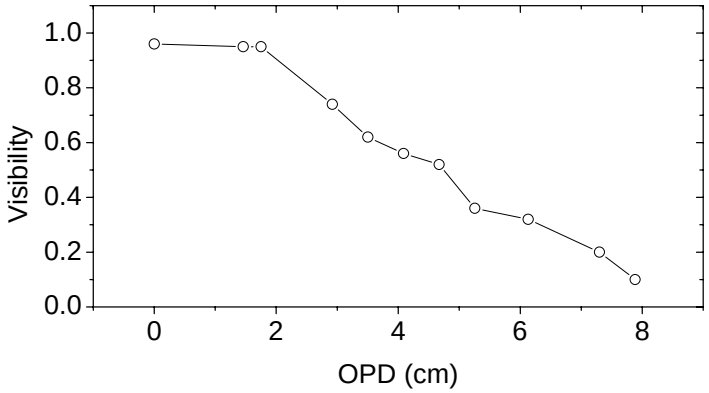


Fig. 29. Interference visibility as a function of OPD of the Michelson interferometer.

### 4.5. Linear laser tuning

Although Fig. 26 shows a nearly linear tuning over a limited wavelength range, the nonlinear effect becomes more noticeable when the wavelength range is extended. A quantitative indication of the chirp rate stability is obtained by measuring the time interval for scanning through a fixed number of fringes of the FFPI signal. A variation of about 5% in frequency scanning rate is found over the 46 nm frequency scanning range of the laser. To improve the chirp rate stability, an active optical feedback technique is employed. During each frequency scan, the Labview program determines the accumulated time t(N) for scanning through N fringes from the FFPI data by the computer, and then calculates an error signal proportional to the difference between the measured t(N) and a function t'(N) = KN, with K a constant proportional to the desired chirp rate. This error signal is fed back to the voltage generating program to adjust the

mirror angular rotation as needed to compensate for the accumulated error. In the experiment, N = 25.

The improvement in scan linearity achieved by this optical feedback technique is shown in Fig. 30. The root mean square variation in the optical chirp rate is reduced to 0.3%.

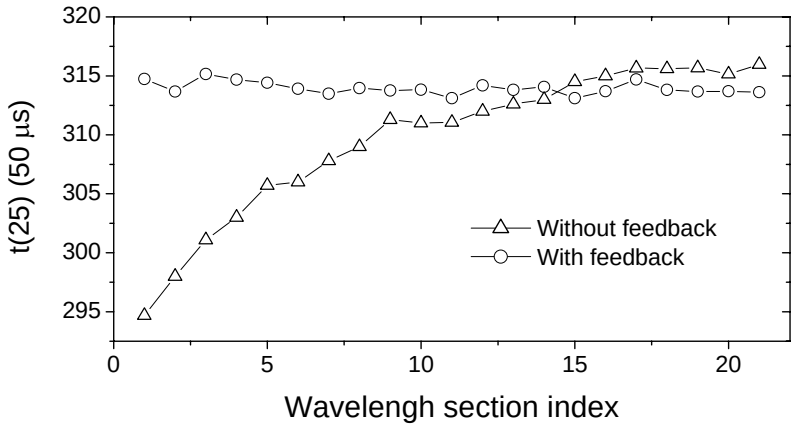


Fig. 30. The time interval for 25 fringe shift in different wavelength sections.

Another indication of the effect of the optical feedback is shown by the Fourier transform of the temporal data from the FFPI for the two cases, shown in Fig. 31. The 3 dB spectral width is 75 Hz without feedback and 5 Hz with feedback.

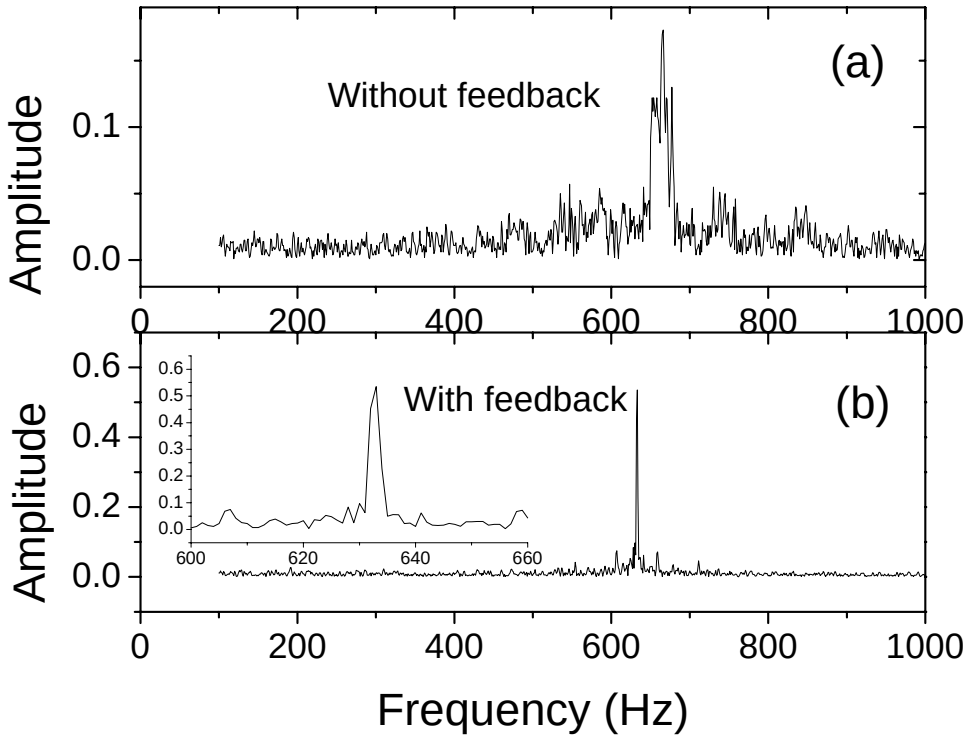


Fig. 31. Fourier amplitude of the reflected signal data in the cases (a) without feedback, (b) with the feedback.

### 4.6. Summary

In this section, we have introduced the fundamentals of the Erbium-doped fiber, and reviewed the history and background of Erbium-doped fiber lasers. In previously reported EDFL research, the tunability and single longitude mode oscillation with narrow linewidth were studied. In the present work, an EDFL using rotating a mirror-grating combination as one of the reflectors in a Fabry-Perot laser cavity has been tuned

over a 46 nm spectral range. Linearization of the chirp rate has been achieved using feedback from a fiber Fabry-Perot interferometer (FFPI) to adjust the voltage ramp which drives the rotating mirror. This method represents a simple and relatively inexpensive alternative to the optical spectrum analyzer in some spectroscopy applications.

# V. THE MONITORING AND MULTIPLEXING OF FFPI SENSORS USING A LINEARLY CHIRPED ERBIUM-DOPED FIBER LASER

## 5.1. Introduction

White light interferometry (WLI) is established as a practical method of measuring the absolute optical path difference (OPD) in interferometric fiber optic sensors. In most such systems, light from a broadband source is coupled into a scanned Michelson interferometer and then into the fiber sensor.[3,56,57] A fringe pattern is produced by the optical power transmitted or reflected from the sensor. The peak of the central fringe occurs when the OPD of the scanned Michelson interferometer exactly matches that of the fiber sensor.

Compared to monitoring systems for interferometric sensors which make use of single frequency (laser) light sources, WLI offers two important advantages: (1) the ability to make accurate measurements from a "cold start" with no a priori knowledge of the OPD, and (2) the ability to monitor many sensors deployed along a single fiber using coherence multiplexing.[58-60]

Another approach to monitoring the OPD in an interferometer makes use of a linearly chirped light source. In this case, the OPD is proportional to the frequency of the photodetector signal produced by the coherent addition of the amplitudes of the light waves which have traversed the two interferometer paths.[61,62] This method represents an optical implementation of the frequency modulated continuous wave (FMCW) technique first applied in radar systems.[63] Generally, the OPD is determined from the Fourier transform of the detected signal. The amplitude of the Fourier transform is used to evaluate the OPD with relatively low spatial resolution (>> 1 optical wavelength) over long ranges (>> 1 km), while the phase information allows for measurement of

OPDs with high spatial resolution (<< 1 wavelength) over short ranges (< 1 wavelength).

This research encompasses the application of the FMCW technique to obtain spatial resolution << 1 wavelength and range >> 1 wavelength in OPD measurements by utilizing both the amplitude and phase of the Fourier transform of the output signal. This is made possible by the wide spectral tuning range of the chirped laser. This scheme combines the primary benefit of laser monitoring - high fiber-coupled optical power and high signal-to-noise ratio - with the two advantageous features of WLI mentioned above. Thus, in cases where absolute OPD measurements are needed, the present scanned laser scheme is capable of achieving a higher dynamic range for an individual sensor and is also capable of multiplexing a greater number of sensors with a single light source and photodetector than is a conventional WLI setup. Furthermore, optical implementation of the scanned laser system is somewhat simpler than a conventional WLI system.

## 5.2. Theory

In the general case of N interferometers arranged in series, the photocurrent signal $I_s$ due to the light which has passed through the interferometers can be written

$$I_s = C_0 + \sum_{j=1}^{j=N} C_j \cos(\phi_j), \tag{5.1}$$

where the $C_j$'s are real constants which depend on the configuration of the system and the $\phi_j$'s are the optical phase shifts in the interferometers given by

$$\phi_j = 2\pi\nu D_j / c, \tag{5.2}$$

with $\nu$ the optical frequency, $D_j$ the optical path difference (OPD) for the j'th interferometer, and $c$ the free-space speed of light. Here, it is assumed that the modulation depths for the interferometers are small ($C_j << C_0$, all j), so that in eq. (5.1) terms in $I_s$ involving products of the $C_j$'s are neglected. If only one interferometer is

present, the photocurrent will vary sinusoidally with $\nu$, suggesting Fourier analysis of $I_s(\nu)$ as a means of determining the OPD. If multiple interferometers with different OPDs are present, each Fourier component will correspond to a different $D_j$ value. The optical transit time $\tau = D/c$ is the Fourier conjugate to ν. Values for the $D_j$'s can now be determined from the photocurrent signal by taking the Fourier transform $A_s(\tau)$, defined as

$$A_s(\tau) = \int_{\nu_a}^{\nu_b} I_s(\nu) \exp[-2\pi i \tau(\nu - \nu_a)] d\nu \tag{5.3}$$

where $\nu_a$ and $\nu_b$ are the optical frequencies at the start and at the end of the chirp. It follows from eqns. (5.1), (5.2), and (5.3) that, for the case of a single interferometer of OPD $D_j$,

$$|A_s(\tau)|^2 = C_j{}^2 \sin^2[\pi(\tau_j - \tau)(\nu_a - \nu_b)]/[2\pi(\tau_j - \tau)]^2 . \tag{5.4}$$

The magnitude of the Fourier transform $|A_s(\tau)|$ has a maximum value of $C_i(\nu_b - \nu_a)/(2\pi)$ at the delay time $\tau_j = D_j/c$. Furthermore, the Fourier transform at that maximum can be expressed as

$$A_s(\tau_j) = |A_s(\tau_j)| \exp[i\phi_j(\nu_a)] . \tag{5.5}$$

Therefore, the sensor phase shift $\phi_j(\nu_a)$ can be determined from the phase part of the Fourier transform as $\phi_j(\nu_a) = 2Q_j\pi + \bar{\phi}_j(\nu_a)$, with $Q_j$ an arbitrary integer and $0 \le \bar{\phi}_j(\nu_a) < 2\pi$. We notice that once it is determined, the sensor phase shift at an arbitrary frequency is also determined:

$$\phi_j(\nu) = 2Q_j\pi + \bar{\phi}_j(\nu_a) + 2\pi\tau_i\nu . \tag{5.6}$$

According to eq. (5.2), $\phi_j(\nu_a)$ varies by 2π rad. for a change in $D_j$ of one wavelength. In order for $\overline{\phi}_j(\nu_a)$ to be of practical value, it is necessary to determine the OPD value to a small fraction of an optical wavelength such that $Q_j$ can be determined.

The absolute square of the Fourier transform in eq. (5.4) is a sinc-squared function with a full width to the first zeroes $\Delta\tau$ given by

$$\Delta\tau = 2/(\nu_b - \nu_a), \tag{5.7}$$

and the corresponding change in $D_j$ is given by

$$\Delta D_j = 2c/(\nu_b - \nu_a). \tag{5.8}$$

Since $\lambda_a \nu_a = c$, with $\lambda_a$ the free-space optical wavelength at the start of the laser scan, it follows from eq. (5.8) that

$$\Delta D_j = 2\lambda_a \nu_a/(\nu_b - \nu_a). \tag{5.9}$$

Thus, the width of the spectral peak of the electrical signal, in terms of OPD, is much wider than an optical wavelength; for example, if the spectral scanning range is 2% of the laser frequency, the width of the spectral peak, to the first zeroes, is 100 wavelengths.

It is assumed, and later verified experimentally, that $D_j$ can be determined to within a range substantially less than one wavelength using the measured spectral position of the peak in $|A_s(\tau)|$. Although this represents a coarse OPD determination, it makes it possible to fine tune this result based on the measured phase of the Fourier transform $\overline{\phi}_j(\nu_a)$ and applying eq. (5.2) to determine $D_j$.

The determination of $D_j$ to an accuracy much less than one wavelength is facilitated by the use of a reference interferometer of known OPD. As a practical matter this interferometer, of optical length $D_r$, would be held in a controlled environment (i.e., at a fixed temperature and shielded from other perturbing effects) so that its optical

length is known to a high degree of accuracy. The signal from this interferometer, interrogated by the same chirped laser as the sensing interferometer, produces a photocurrent $I_r$ given by

$$I_r = C_0' + C_r \cos(\phi_r), \tag{5.10}$$

where, as before, $C_0'$ and $C_r$ are constants determined by the system configuration, and the phase shift $\phi_r = 2\pi\nu D_r / c$. Then, a coarse value for $D_j$ is determined from $\tau_j$ and $\tau_r$, the spectral peak positions of the signal and reference waveforms, respectively, using the expression

$$D_j = D_r \tau_j / \tau_r \ . \tag{5.11}$$

Similarly, eq. (5.2) can be applied so that a fine value for $D_j$ is determined from the difference between $\phi_j(\nu_a)$ and $\phi_r(\nu_a)$, the phase shifts of the signal and reference waveforms, respectively, by evaluating

$$D_j = D_r + c[\phi_j(\nu_a) - \phi_r(\nu_a)] / 2\pi\nu_a \, . \tag{5.12}$$

### 5.3. Monitoring a single FFPI sensor

The experimental arrangement is shown in Fig. 32. The linearly chirped erbium-doped fiber laser developed at Texas A&M University is described in Section IV. Tuning is accomplished using an intracavity rotating mirror driven by a function generator with a 1 Hz triangular waveform. The laser output is directed to a reference FFPI and two sensing FFPIs, and three photodiodes monitor the reflected signal from each FFPI separately. Lengths of the reference FFPI and the sensor FFPIs are 10mm, 12 mm and 10 mm respectively.

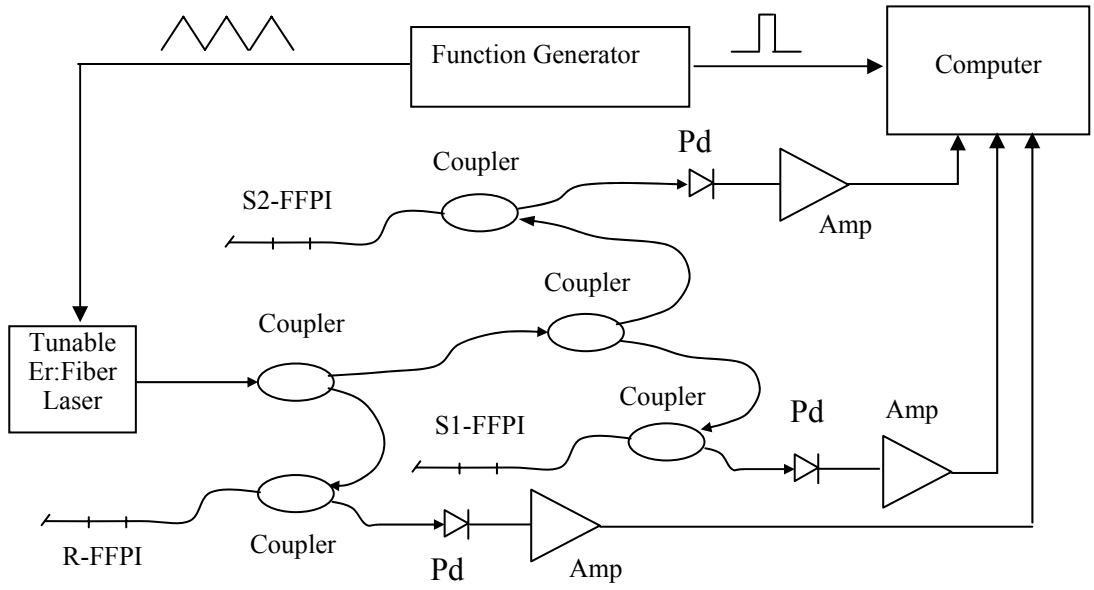


Fig. 32. Experimental arrangement for monitoring FFPI sensors.

A data acquisition program is trigged by the function generator clock to take the data of the reflected signal from the three photodiodes. 16,000 samples are taken for one sweep at a sampling rate of 40 kHz (25 μs sampling interval). Fig. 33 shows the reflected signal waveforms for a portion of one sweep. It is evident from the regular interference fringe patterns in Fig. 33 that, although the optical frequency from the laser is close to a linear function of time, there are noticeable fluctuations in the scan rate.

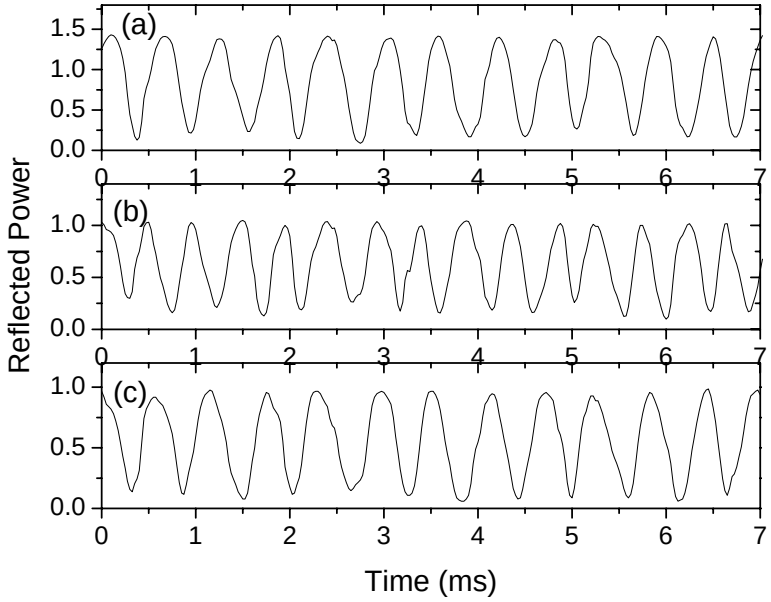


Fig. 33. Reflected single as a function of time for (a) R-FFPI, (b) S1-FFPI, (c) S2-FFPI.

According to the theory in the preceding section, $\nu_a$, the Fourier transform starting frequency defined in eq. (5.3), must be a constant for repeated measurements, such that the obtained $\phi_s(\nu_a)$ is valid to represent the OPD. Therefore, a strict procedure must be followed: At the first peak of the R-FFPI signal of the ith measurement, the phase $\phi_r = 2m_i\pi + \Delta_i$, with $m_i$ an integer and the deviation $\Delta_i << 2\pi$. It is assumed, and later verified in the experimental results, that $m_i \equiv M$ is a constant for repeated measurements. Now we can choose $\phi_r(\nu_a) = 2M\pi$, so that $\nu_a$ is defined as $\nu_a = cM / D_r$. Furthermore, we define the phase shift relative to $\phi_r(\nu_a)$ as:

$\widetilde{\phi}_r = \phi_r(\nu) - 2M\pi$. We notice that $\widetilde{\phi}_r$ is a quantity that can be unambiguously obtained from the continuous R-FFPI signal by applying eq. (5.10). Therefore, eq. (5.3) becomes:

$$A_s(\tau) = \frac{1}{2\pi\tau_r}\int_0^{1350\pi} I_s(\widetilde{\phi}_r)\exp(-i\tau\widetilde{\phi}_r/\tau_r)d\widetilde{\phi}_r, \tag{5.13}$$

where the integral range of 1350π corresponds to the entire laser wavelength region. For the discrete data set $\{t_k, \widetilde{\phi}_r(t_k), I_s(t_k)\}$ in Fig. 33, eq. (5.13) is approximated as:

$$A_s(\tau) = \frac{1}{2\pi\tau_r}\sum_0^{\widetilde{\phi}_r=1350\pi} I_s(t_k)\exp[-i\tau\widetilde{\phi}_r(t_k)/\tau_r]\cdot[\widetilde{\phi}_r(t_k) - \widetilde{\phi}_r(t_{k-1})]. \tag{5.14}$$

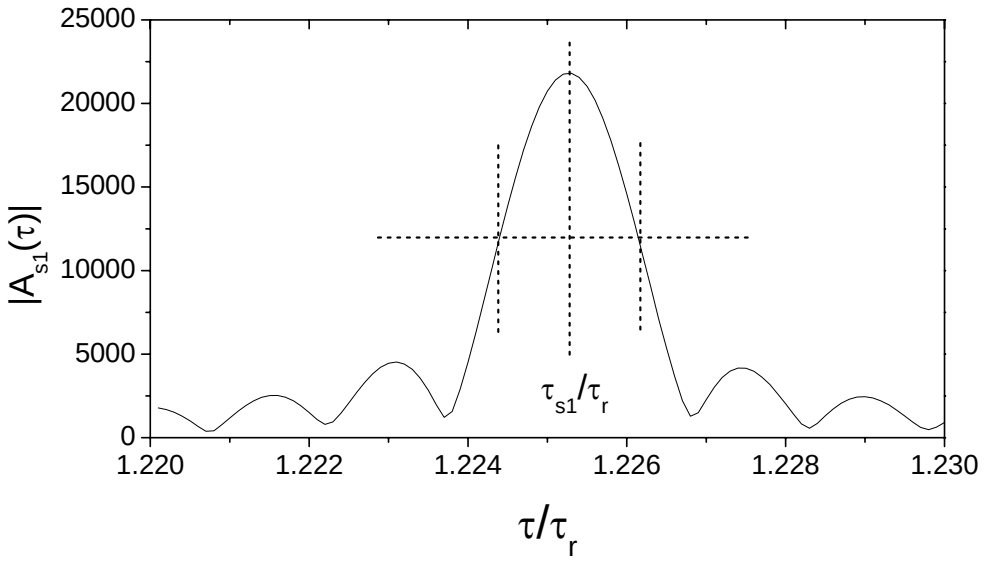


Fig. 34. Fourier amplitude of the S1-FFPI signal.

Fig. 34. shows the amplitude of the complex Fourier transform for the S1-FFPI signal. To compute OPD for the sensor, the first step is to determine as precisely as possible the peak position in the plot and apply eq. (5.11). The peak position $\tau_{s1}$ is determined by averaging the values of $|A_{s1}(\tau)|$ on the rising and falling edges of the

curve at the half-maximum points, thus taking advantage of the high slope at those locations. Following eq. (5.5), $\bar{\phi}_{s1}(\nu_a)$ is determined from the phase of the Fourier component at $\tau_{s1}$ within 0~2π range. Furthermore, the sensor phase shift at an arbitrary frequency follows eq. (5.6):

$$\phi_{s1}(\nu) = 2Q_{s1}\pi + \bar{\phi}_{s1}(\nu_a) + \tilde{\phi}_r(\nu)\tau_{s1}/\tau_r . \tag{5.15}$$

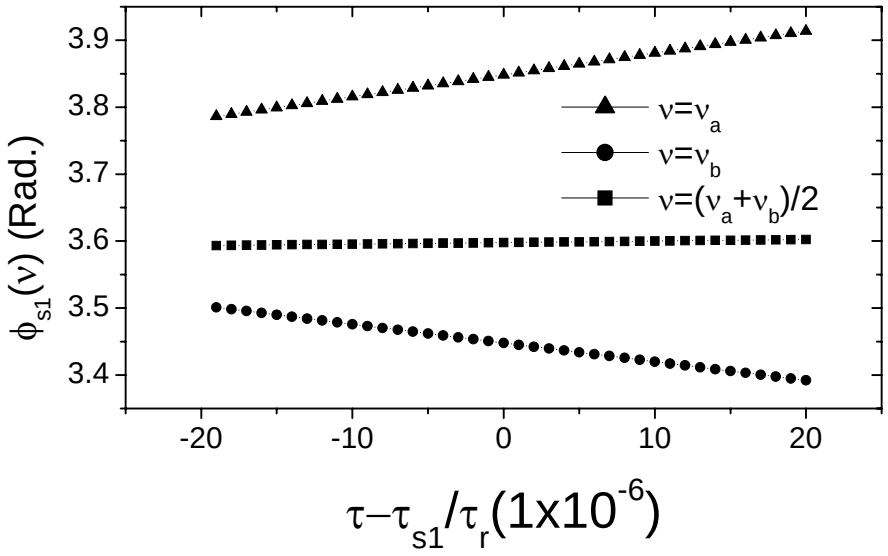


Fig. 35. At the start, end and central frequency, the phase as a function of $\tau$. Curves are vertically shifted to give a close view of the linear dependence in the same figure.

Nevertheless, the $\tau_{s1}$ value thus obtained is a coarse OPD measurement, so the deviation $\Delta\tau_{s1}$ is carried over to the phase shift result. Following eq. (5.15), the phase shift deviation is given as:

$$\Delta\bar{\phi}_{s1}(\nu) = \Delta\bar{\phi}_{s1}(\nu_c) + 2\pi(\nu - \nu_c)\Delta\tau_{s1}, \tag{5.16}$$

where $\nu_c = (\nu_a + \nu_b)/2$ is the center of the Fourier frequency integral range, and $0 \leq \bar{\phi}_{s1}(\nu) < 2\pi$. As shown in Fig. 35, $\bar{\phi}_{s1}(\nu_c)$ is nearly a constant in the neighborhood of $\tau_{s1}$, whereas $\bar{\phi}_{s1}(\nu_a)$ and $\bar{\phi}_{s1}(\nu_b)$ are linear functions of $\tau$ with slopes of opposite sign. It follows from eq. (5.15) that, because linear function $\phi_{s1}(\nu)$ thus obtained is the best fit of the actual one with the slope $\tau_{s1}$, points at near the center frequency region should be least affected by the deviation of $\tau_{s1}$, whereas points at two end frequencies have errors proportional to the slope deviation.

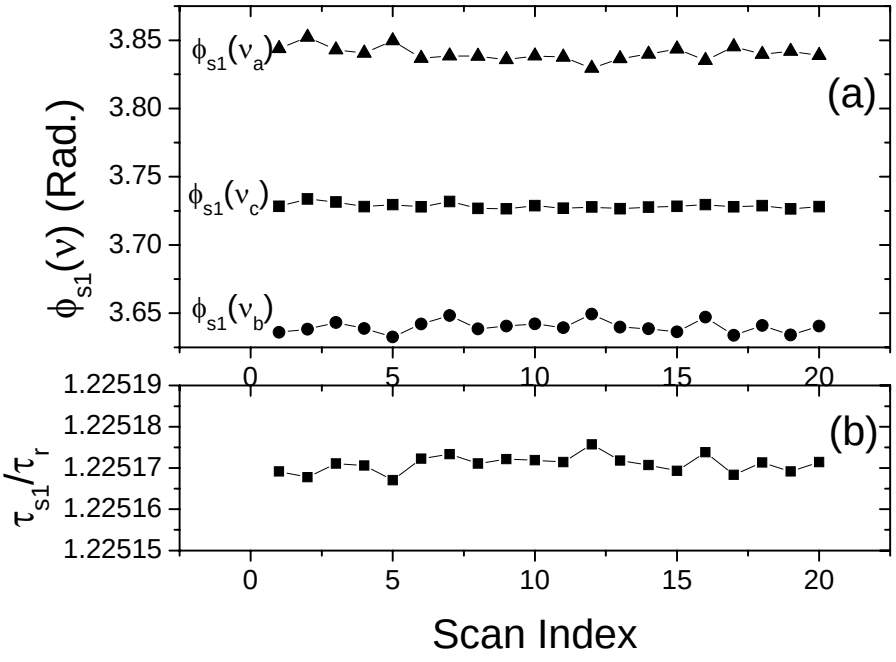


Fig. 36. Parameters of S1-FFPI for 20 consecutive laser scans, showing (a) variations in the phase, (b) variations in the relative interferometer delay time. Curves in (a) are vertically shifted to give a close view.

In a resolution test, sensor S1-FFPI and S2-FFPI are collocated with R-FFPI, and the parameters are calculated for the data of 20 consecutive laser scans. The results of S1-FFPI are shown in Fig. 36. The results of S2-FFPI are similar.

Table 1 summarizes the statistics of the measurement. It is confirmed again that $\bar{\phi}_{s1}(\nu_c)$ is more accurate than $\bar{\phi}_{s1}(\nu_a)$ and $\bar{\phi}_{s1}(\nu_b)$. In addition, the largest OPD error resulting from $\tau_s$ is much smaller than one fringe, thus making it possible to utilize the phase information $\bar{\phi}_{s1}(\nu_c)$ to improve the resolution of the OPD measurements substantially over what would be possible using $\tau_s$ alone.

Table 1. Sensors' OPD deviations (RMS) based on the Fourier peak and phase shift.

| Sensor | $\Delta\tau_s$ | $\Delta\phi_s(\nu_a)$ | $\Delta\phi_s(\nu_b)$ | $\Delta\phi_s(\nu_c)$ | OPD unit |
|---|---|---|---|---|---|
| S1 | 60 | 1.3 | 1.2 | 0.48 | nm |
| | 0.039 | $8.1\times10^{-4}$ | $7.3\times10^{-4}$ | $3.0\times10^{-4}$ | fringe |
| S2 | 24 | 0.64 | 0.52 | 0.42 | nm |
| | 0.015 | $4.1\times10^{-4}$ | $3.3\times10^{-4}$ | $2.7\times10^{-4}$ | fringe |

Previously, $\nu_a$ was defined such that $\phi_r(\nu_a) \equiv 2M\pi$, and the first reflective peak of R-FFPI data has been assumed to be very close to the $M$ th reflective maximum of R-FFPI. However, if the data acquisition were triggered advanced or delayed, the first peak could possible shift to the $M+k$ th maximum. Consequently, the obtained $\bar{\phi}_{s1}(\nu_a)$ from eq. (5.14) would carry an error of $2k\pi(\tau_s/\tau_r - 1)$. As is evident from Fig. 36, the first peak maintains at the same fringe for repeated tests, so the data acquisition trigger is proved reliable.

Although $M$ is confirmed to be a constant, the exact value remains to be determined. According to the definition of $\nu_c$, the phase at the frequency $\phi_r(\nu_c) = (2M + 675)\pi$. Applying the described Fourier transform technique, the phase of the sensor FFPIs can be generally expressed as $\phi_s(\nu_c) = 2N_s\pi + \bar{\phi}_s(\nu_c)$, with $N_s$ an integer and $0 \le \bar{\phi}_s(\nu_c) < 2\pi$. Consider the following equation

$$n_s = (2m + 675)\tau_s / \tau_r - 2\bar{\phi}_s(\nu_c)/2\pi, \tag{5.16}$$

where $n_s$ will approach to the integer $N_s$, if the integer variable $m = M$. Applying the parameters obtained in Fig. 36, $n_s$ is plotted as a function of $m$ in Fig. 37. Among the adjacent ~4,000 integers, 18339 is the only integer that makes $n_{s1}$ and $n_{s2}$ both approach to integers. Therefore, it is determined that $M$ =18339, $N_{s1}$=22991, and $N_{s2}$ = 18787. Combining the results shown in Fig. 37, the OPD dynamic range is $7.7\times10^7$.

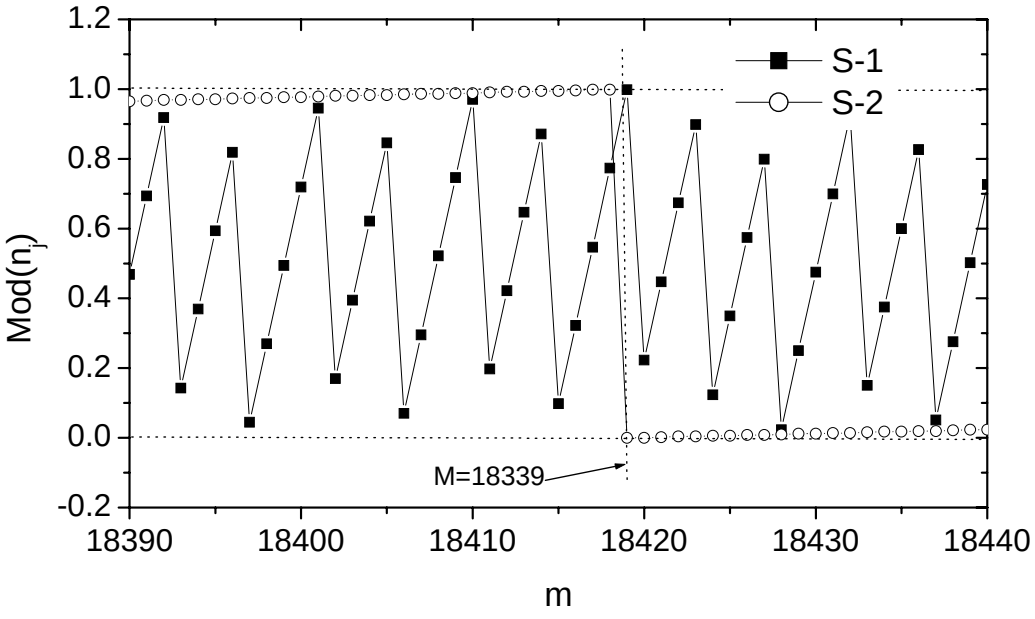


Fig. 37. M is located when $n_{s1}$ and $n_{s2}$ both approach to integers.

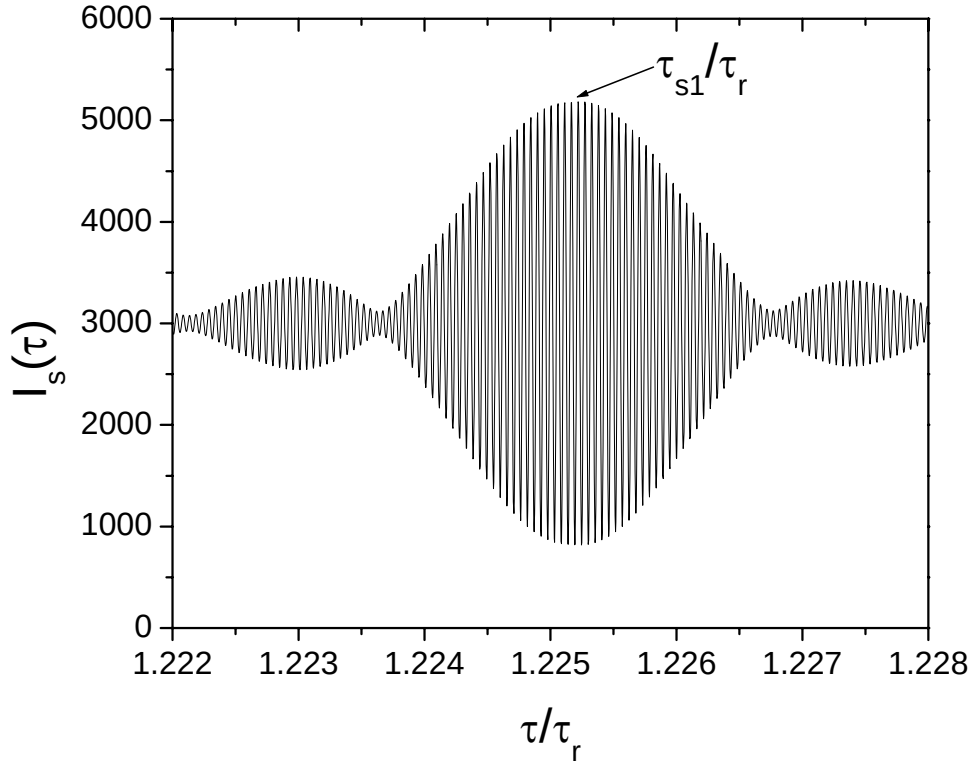


Fig. 38. A "WLI signal" produced by "scanning" a virtual Michelson interferometer.

Now that the absolute phase of R-FFPI is known, a virtual WLI monitoring with an OPD scanned Michelson interferometer can be implemented: The reflectance of a virtue Michelson interferometer is

$$R(\tau) = 1 + \cos[\phi_r(\nu)\tau / \tau_r]. \tag{5.17}$$

When the OPD of this interferometer is "scanned" by changing the parameter $\tau$, a "WLI signal" is produced as

$$I_s(\tau) = \int_{\nu_a}^{\nu_b} I_s(\nu)\{1 + \cos[\phi_r(\nu)\tau / \tau_r]\} d\nu. \tag{5.18}$$

With the “WLI signal” shown in Fig. 38, a special algorithm can be applied to locate the center peak, which is the OPD of the FFPI sensor.

### 5.4. Multiplexing of FFPI sensors

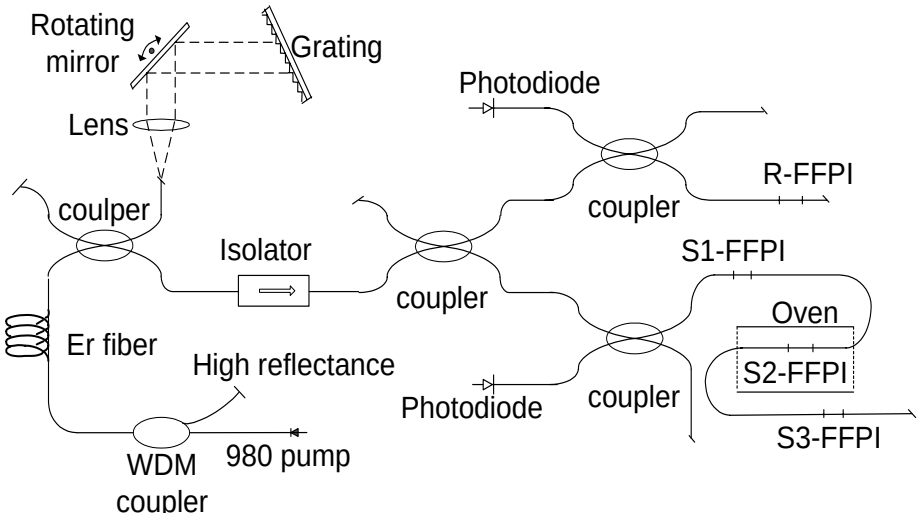


Fig. 39. Experimental setup for multiplexing three FFPIs.

One distinct advantage of the FMCW technique for the monitoring of interferometers is the multiplexing capability. An experimental arrangement shown in Fig. 39 is implemented to investigate the multiplexing performance. The laser output is directed to a reference fiber Fabry-Perot interferometer (R-FFPI) and three sensing interferometers (S1-FFPI, S2-FFPI, S3-FFPI) connected in series. Lengths of the three sensing interferometers are approximately 10 mm, 12 mm, and 11 mm, respectively, while the length of the reference interferometer is approximately 12 mm. A reference photodiode and a sensing photodiode monitor the reflected light from the FFPIs.

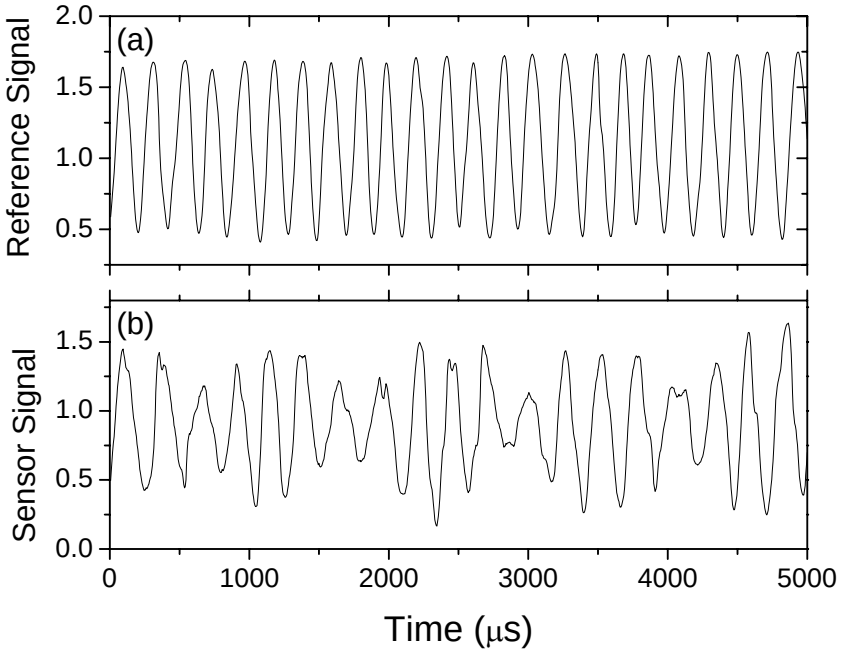


Fig. 40. Reflected signal over a portion of a laser frequency scan for (a) reference FFPI, (b) three multiplexed sensing FFPIs.

It is evident from the regular interference fringe pattern from R-FFPI in Fig. 40(a) that, although the optical frequency from the laser is close to a linear function of time, there are noticeable fluctuations in the scan rate. Fig. 40(b) shows the sensor waveform, which is a superposition of reflected light from the three sensing interferometers. Following eq. (5.14), a Fourier transform is applied to the sensor data. The Fourier amplitude is shown in Fig. 41.

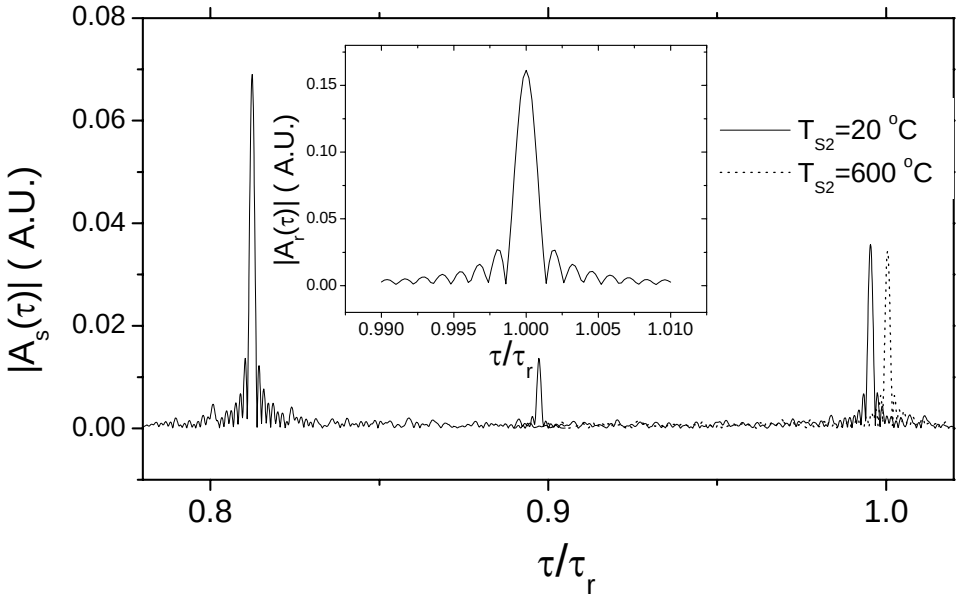


Fig. 41. Fourier transfer amplitude obtained from the sensor scan data (main plot) and the reference interferometer scan (inset).

Variations in the peak positions determined in this manner over 30 consecutive laser frequency scans for the three sensors are plotted in Fig. 42(a-c). The root mean square errors for the three sensors, in fringes, are summarized in Table 2. By contrast, when the raw data was processed without compensating for laser scan rate variations, the root mean square errors were of the order of 10 fringes - an indication of the importance of compensating the data before processing it to determine the OPDs.

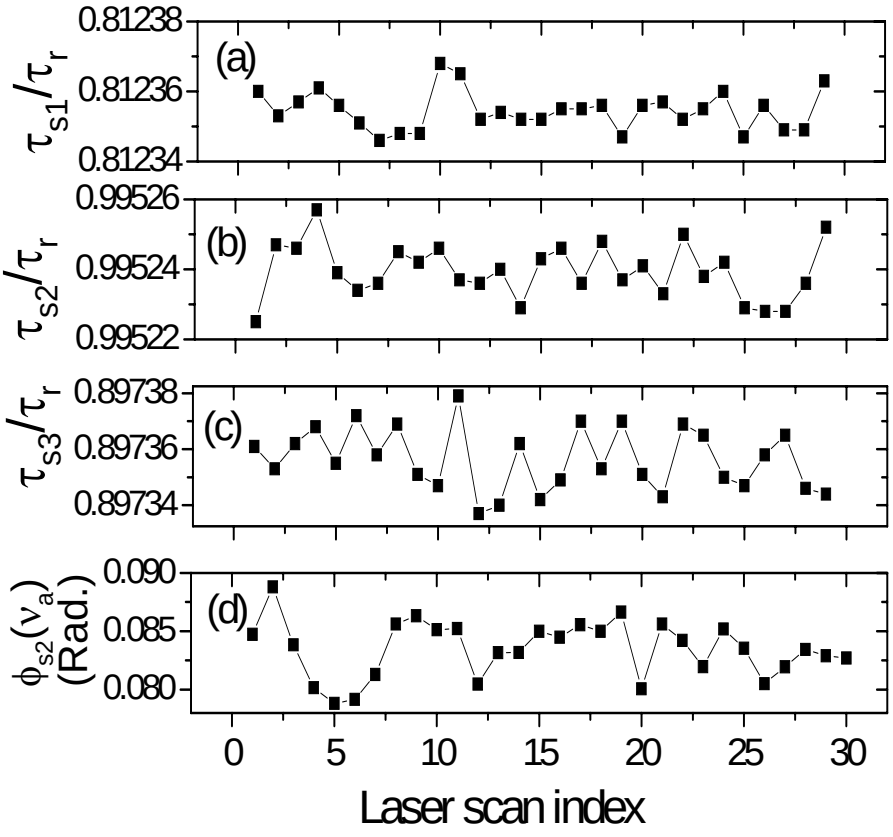


Fig. 42. Data for 30 consecutive laser scans, showing (a-c) variations in the interferometer delay time $\tau$ for the sensors, (d) variations in the phase determined for one of the sensors.

Table 2. OPD measurement resolution using Fourier transform amplitude information only, and using both amplitude and phase information.

| Sensor | Fourier component | $\Delta\tau_s$ | $\Delta\phi_s(\nu_c)$ | OPD unit |
|---|---|---|---|---|
| S1 | Amp. only | 200 | 4.1 | nm |
| | Amp. & Phase | 0.15 | 0.0027 | fringe |
| S2 | Amp. only | 300 | 3.6 | nm |
| | Amp. & Phase | 0.2 | 0.0024 | fringe |
| S3 | Amp. only | 400 | 6.3 | nm |
| | Amp. & Phase | 0.25 | 0.0042 | fringe |

Since the largest error for any of the sensors indicated in Table 2 is << 1 fringe, it is possible to utilize the phase information inherent in the complex Fourier transform and apply eq. (5.12) to improve the resolution of the OPD measurements substantially over what would be possible using amplitude information alone. Fig. 42(d) shows the phase variation for one of the sensors over 30 consecutive laser scans. As indicated in Table 1, the resolution improvement is nearly 2 orders of magnitude.

Finally, the results of measuring the variation in OPD of sensor S2-FFPI over the range from 20°C to 610°C during a heating and cooling cycle are plotted in Fig. 43. Temperature was determined with a reference thermocouple colocated with the sensor in a small oven. Both amplitude and phase information were used in obtaining this plot.

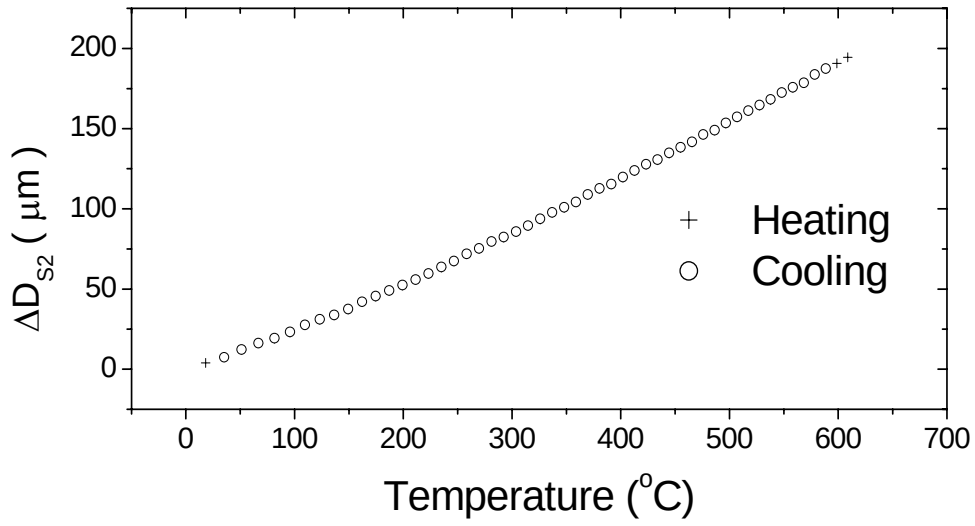


Fig. 43. Variation in OPD of S2-FFPI during a heating and cooling cycle.

### 5.5. Discussion

It is useful to compare the results reported above with other OPD measurements using conventional FMCW techniques. A useful basis for comparison is the dynamic range DR, which will be defined for the results reported here as

$$DR = L_c/\Delta(OPD), \tag{5.19}$$

with $L_c$ the coherence length of the light source (an indication of the maximum measurable OPD) and $\Delta$(OPD) the measurement resolution. The measured coherence length of the scanned Erbium-doped fiber laser used in these experiments was 4.7 cm. Using the value $\Delta$(OPD) = 3.6 nm from Table 2, the calculated DR from eq. (5.19) is $1.3\times10^7$.

A large number of FMCW experiments in optical fibers have been carried out using the Fourier transform amplitude to determine the OPD.[64] The best resolution reported was 14 cm and the best DR was 7,200.[65] On the other hand, in an experiment using a linearly chirped semiconductor laser light source in which a phase measurement was used to determine the OPD, the shot-noise-limited resolution was $3 \times 10^{-5}\ \lambda$, with $\lambda$ the optical wavelength of 1300 nm.[2] Assuming a maximum OPD of one fringe, as is the case for an absolute measurement system, the DR in this case is equal to 30,000.

As the results reported above indicate, the ability to use both phase and amplitude information to determine the OPD makes it possible to extend the measurement dynamic range in an FMCW system by orders of magnitude.

## 5.6. Conclusions

It has been shown that a linearly chirped laser can be used in measuring the OPD of interferometric fiber optic sensors by performing a Fourier transform of the optical signal. A coarse determination of the OPD is obtained by measuring the position of the peak of the absolute square of the Fourier transform amplitude, while fine resolution is obtained from the phase of the Fourier transform. Experimentally, a scanned Erbium-doped fiber laser was used to interrogate three FFPI sensors located serially along a single mode fiber. For accurate OPD measurement, it was necessary to compensate the raw data for variations in the laser scan rate. Temperature was measured with one of the sensors from 20°C to 610°C with a 0.02°C resolution. Multiplexing of three of the sensors arranged in series was demonstrated, with OPD resolution ranging from 3.6 nm to 6.3 nm.

Although the chirped laser monitoring system reported here was characterized for temperature measurement only, with appropriate packaging of the sensing elements[66] it can be used for measurands such as strain and pressure as well. Due to the ability to obtain high accuracy over wide dynamic range for many multiplexed sensors with a single light source, photodetector, and fiber transmission line, such a system could prove cost-effective in a variety of applications. Examples include downhole measurement of

temperature[67] and pressure[68] in oil and gas wells, and strain measurement on railroad[69] and highway bridges[70] and the hulls of ships.[71]

# VI. THE MONITORING AND MULTIPLEXING OF FBG SENSORS USING CHIRPED LASERS

## 6.1. FBG sensors with linearly chirped fiber laser

In an FBG sensor system, the measurand information is resolved by determining the induced Bragg wavelength change. One typical interrogation method is based on the combination of a broadband light source and a wavelength detecting device. The broadband light source is generally either a superluminescent light emitting diode (SLED) or the amplified spontaneous emission (ASE) light of an EDFA.Various wavelength detecting techniques have been demonstrated using an OSA, edge filters, scanning filters and interferometers. However, these schemes have shown difficulties associated with low signal due to the use of narrow spectral band of the light source, low spectral resolution of the filters or spectrometers, or limited dynamic range with the interferometric phase read out.

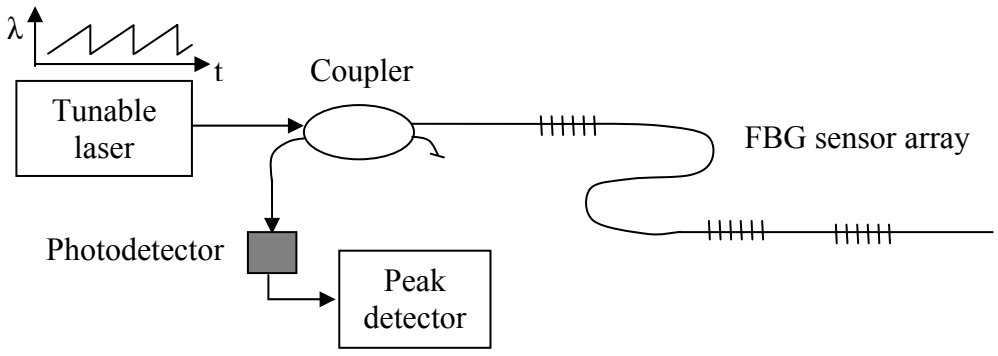


Fig. 44. FBG sensors with tunable laser arrangement.

Active erbium-FBG laser sensors were introduced to increase the signal-to-noise ratio over a broadband illuminating system.[72,73] The laser cavities serve as sensing elements such that the laser wavelengths are monitored to resolve the measurand information. A more attractive interrogation approach has been demonstrated that allows a tunable laser to serve as both light source and spectral analyzer.[74,75] The general arrangement is shown in Fig. 44. When the laser frequency shifts over a spectral range that covers the FBG sensor array spectrum, the reflected optical signal consists of a series of pulses in the time domain such that the Bragg wavelengths are determined from the timing of the pulse sequence. In order to maximize the sensitivity, accuracy and measurement range, desired features of the laser include narrow linewidth, wide tuning range, sufficient power, continuous tuning, and wavelength calibration.

In the experiment reported by Ball et al.,[74] a short cavity erbium-doped fiber laser with FBG reflectors was implemented to monitor an array of three FBG temperature sensors. The laser was tuned over ~2.3 nm wavelength region by applying tensile strain along the fiber with a piezo-translator. Output power of ~100 μw was obtained at 3 mw pump power. Position sensors and an expansion control loop were applied to the piezoceramic to remove hysterisis and thermal drift such that the laser is tuned as linearly as possible. The expansion accuracy was achieved better than 0.2%, which resulted in the measured FBG sensor wavelength resolution of ~2.3 pm.

In another experiment reported by Yun et al.,[75] an array of 3 FBG strain sensors was monitored with an erbium-doped fiber ring cavity laser. The laser is tuned over 28 nm wavelength range by a piezo driven intracavity Fabry-Perot filter. The tuning range was limited by the 33 nm wide free spectral range for the Fabry-Perot filter. The laser linewidth was estimated to be <0.1 nm. At 60 mw pump power, the output power was ~3.3 mw with 3-4% random fluctuations. The sensor strain resolution is determined as 0.47 με, corresponding to ~0.4 pm in wavelength. However, the experiment results indicated that the laser wavelength shifting has a nonlinearity > 1.5 %, possibly due to the piezo hysterisis. Since the FBG wavelength was determined by the timing of the

return pulses, the impact of the nonlinearity on the measurement accuracy was not carefully examined.

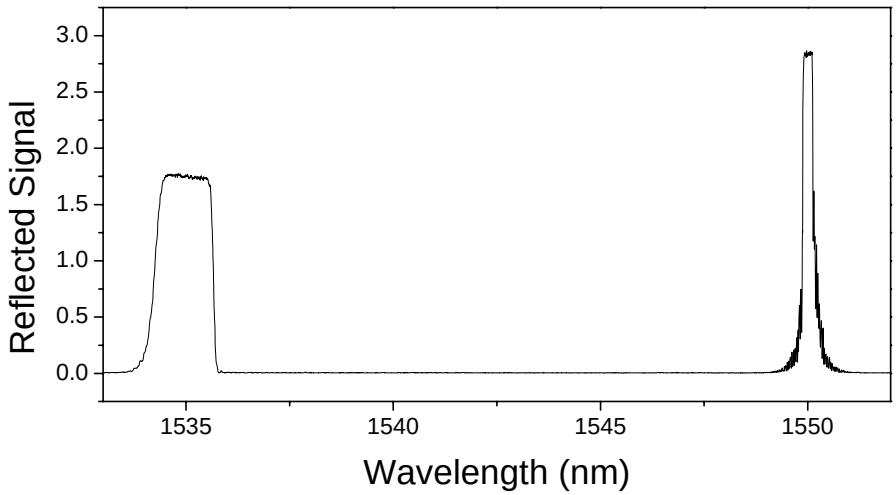


Fig. 45. Laser scanned reflective spectrum of two FBG sensors.

In the present work, the linearly tunable erbium-doped fiber laser designed and assembled at Texas A&M University is used to monitor two FBG sensors serially connected along a single fiber. The laser is tuned over the 1522 to 1568 nm wavelength region with an arrangement of a rotating mirror and bulk grating in Littrow configuration as in Fig. 22. The instantaneous linewidth is measured as 33 pm, and an average laser power of 5.5 mw is obtained at 43 mw pump level. The wavelength shift is monitored with an FFPI sensor such that the laser frequency is shifted at a constant rate with a feedback control loop. Fig. 45 shows the measured spectrum of the FBG sensors, where the time-domain signals have been linearly converted to the frequency domain. The FBG wavelength is identified as the point at which the reflectance is half the

maximum value. Wavelength variations over 30 laser scans were 1.3 pm and 1.7 pm, respectively, for the two FBG sensors.

## 6.2. Monitoring an FBG pair interferometer sensor with a chirped DFB laser

Most fiber optic temperature sensing devices reported to date are classed as intrinsic; i.e., with the sensing element in the fiber itself. Intrinsic sensors are of two basic types: interferometric and fiber Bragg grating (FBG). Some intrinsic temperature measurement schemes which have been reported, with drawbacks of each, include: (1) fiber Fabry Perot interferometer (FFPI) sensor with chirped laser monitoring - cannot provide accurate measurement from a "cold start", [76,77] (2) FFPI sensor with broadband light source (white light interferometry) - signal processing is relatively complex,[3] and (3) FBG with broadband light source - resolution is relatively low[78] and signal processing is somewhat complex. [79,80]

In this research study, we report a new intrinsic fiber optic temperature sensor – FBG pair interferometer (FBGPI) – which is intended to provide all the desired features indicated above: high resolution, the ability to make measurements from a "cold start", and relatively simple signal processing. The spectral dependence of the FBG mirror reflectance makes it possible to determine the "absolute" optical path difference (OPD) in the fiber interferometer from a cold start using chirped laser monitoring.

### 6.2.1. FBGPI

As shown in Fig. 46, two short sections (~2 mm in length) are cut from a 2-cm long commercial FBG and then spliced into a single mode fiber to form an FFPI sensor with a cavity length of ~14.5 mm. The reflectance of the sensor is expressed the same as a conventional FFPI:

$$R = r_1 + r_2 + 2\sqrt{r_1 r_2}\cos\phi \,, \tag{6.1}$$

where $r_1$ and $r_2$ are the individual reflectance of the FBGs, and $\phi$, the round trip propagation phase shift, is given by

$$\phi = 4\pi nL/\lambda , \tag{6.2}$$

with n the effective refractive index of the fiber mode, L the effective cavity length for the FFPI, and λ the free space optical wavelength. The free spectrum range (FSR) of this interferometer sensor is ~7.3 GHz, corresponding to ~0.058 nm in wavelength.

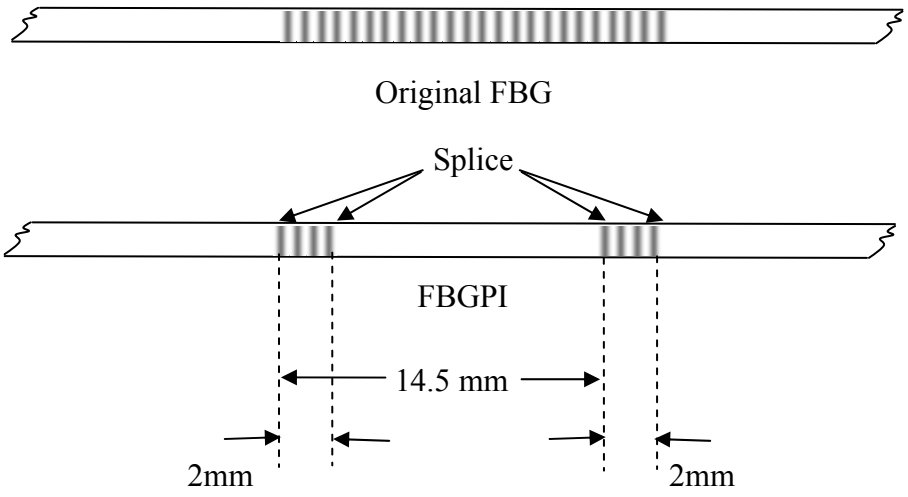


Fig. 46. Diagrams of the FBGPI and the original FBG.

Fig. 47 shows the reflectance spectra of the FBGPI sensor and the original FBG measured with a commercial OSA. Because the 0.2 nm wavelength resolution is much larger than the FSR, the figure shows a "smoothed out" sensor spectrum without the sinusoidal details. It generally agrees with the FBG reflectance dependence on grating length, that the FBGPI sensor has a much lower reflectance and wider bandwidth than the original FBG. At room temperature, the central Bragg wavelength is 1528.3 nm and the DFB laser used in the experiment emits at 1530.6 nm. The FBG sensor spectrum shifts toward longer wavelengths almost linearly at an increasing temperature, so that when the FBGPI sensor is heated, the reflectance vs. temperature plot is a scan of the reversed senor reflectance spectrum.

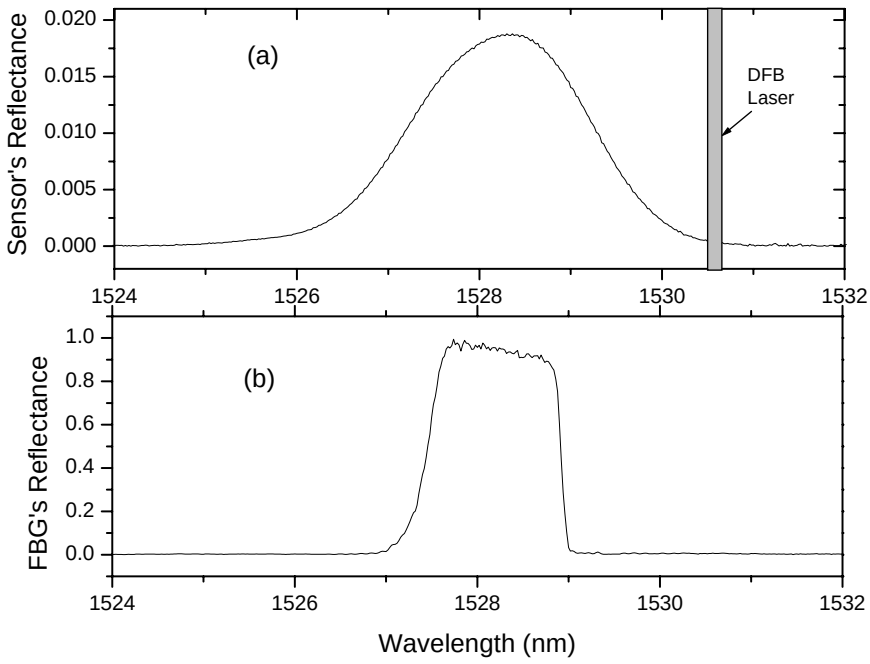


Fig. 47. Reflectance spectrum of (a) the FBGPI sensor; (b) the original FBG.

### 6.2.2. Experiment and results

It is well known that a modulation of drive current causes laser wavelength chirping, an effect which has been used for Fabry-Perot sensing.[2] In the experimental arrangement shown in Fig. 48, the laser driving current is repetitively modulated by a computer generated waveform at frequency of 2 kHz. The modulated laser output is directed to the FBGPI sensor and a conventional reference FFPI sensor with mirrors of reflectance independent of wavelength. The reference FFPI is ~12 mm long and it is held in a controlled environment (i. e., at a known temperature and shielded from other perturbing effects) so that its optical length is kept constant to a high degree of accuracy.

The FBG sensor is placed inside an oven, with temperature monitored by a thermocouple.

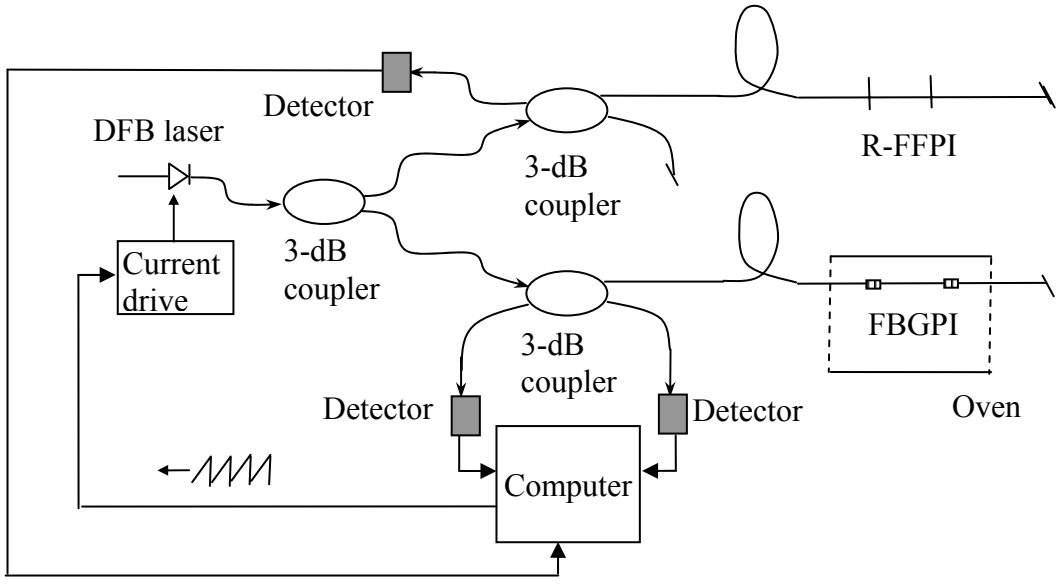


Fig. 48. Experimental arrangement for monitoring an FBGPI with a DFB laser.

When a data acquisition starts, the reflectances of the FBGPI and the reference FFPI are measured by taking the ratio of the reflected light photocurrents to the laser output monitor photo current. Fig. 49 shows the repetitive waveforms of modulated laser power, the FBG sensor reflectance, and the reference sensor reflectance during one full modulation cycle. The data acquisition rate is 400 kHz (2.5 μs sampling interval), so each cycle has 200 sample points. When a modulation cycle begins, the laser wavelength continuously decreases by ~0.15 nm, which produces ~2.6 interference fringes of the FBGPI sensor. At the end of the modulation cycle the laser wavelength abruptly increases to the beginning level. It is evident from Fig. 49(b) that, the amplitude of the FBGPI reflectance is larger at a shorter laser wavelength. When the

FBGPI sensor temperature is increased by 1.5 $^{o}$C, the interference pattern shifts toward left and the modulated amplitude is observed to change by a small increment. This data thus suggests possible absolute OPD method using the amplitude and the phase shift for rough and fine tuning respectively.

In order to determine the phase shift and amplitude for the FBGPI sensor, the Fourier analysis technique previously introduced in a FMCW sensor system is followed. First of all, the laser chirping induced reference FFPI phase shift is monitored. Following eq. (6.1), the phase shift $\tilde{\phi}_r$ is determined from the data in Fig. 49(c) and plotted in Fig. 49(d). Next, the average reflectance and phase shift of the FBG sensor can be respectively determined from the magnitude and phase part of the following complex expression:

$$A_s = \frac{\tau}{4\pi}\int_0^{4\pi/\tau} R_s \cdot \exp(-i\tilde{\phi}_r\tau)\, d\tilde{\phi}_r , \tag{6.3}$$

where $R_s$ is the FBG sensor reflectance, and $\tau$ is a constant approximately equals to the OPD ratio of the FBGPI over the reference FFPI. The integral range covers exact two FBGPI interference fringes. At room temperature, $\tau$ can be accurately measured by averaging a large number of results from a fully Fourier analysis. Furthermore, it can be regarded as a constant within the proposed 400 $^{o}$C temperature measurement range, because an error of less than 0.3% could barely impact on the calculation of amplitude or phase shift. Considering $\tilde{\phi}_r$ and $R_s$ are in the discrete data set $\{\tilde{\phi}_r^{\,k}, R_s^k\}$, eq. (6.3) is approximated as:

$$A_s = \frac{\tau}{8\pi}\sum_{\tilde{\phi}_r^{\,k}=0}^{4\pi/\tau} R_s^k \cdot \exp(-i\tilde{\phi}_r^{\,k}\tau)(\tilde{\phi}_r^{\,k+1} - \tilde{\phi}_r^{\,k-1}) . \tag{6.4}$$

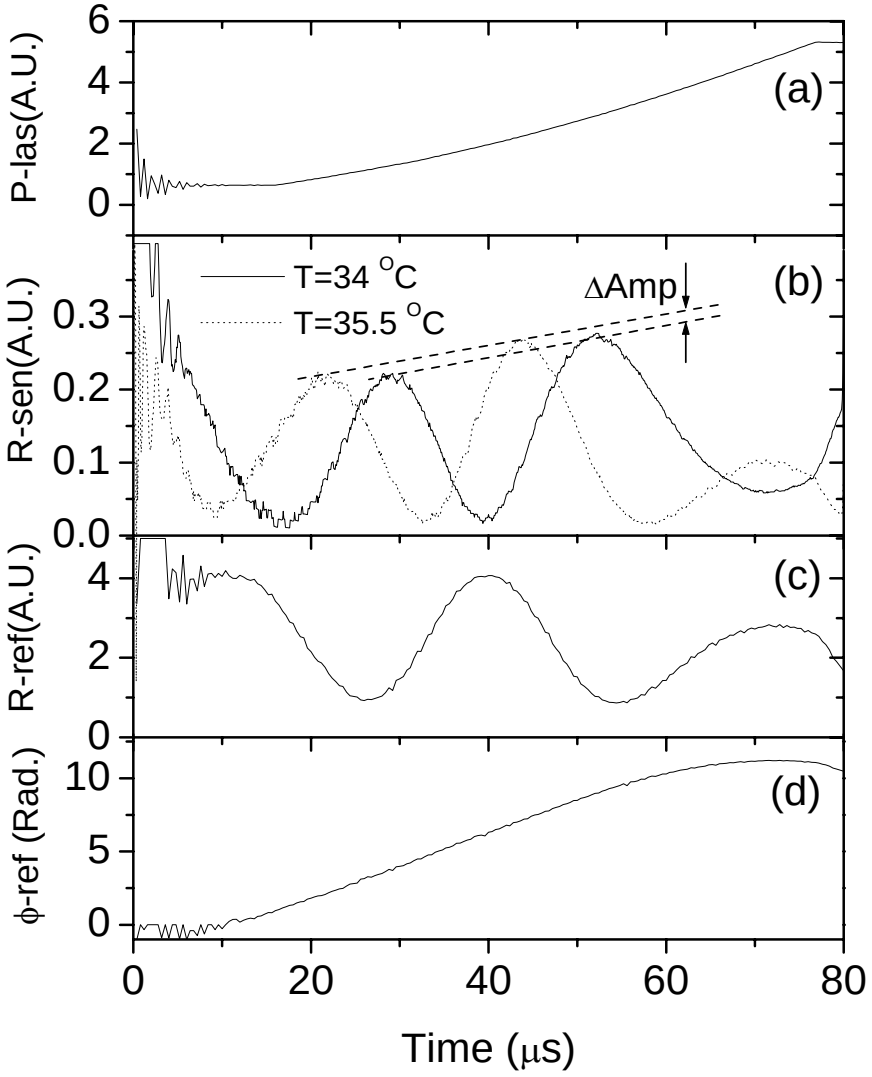


Fig. 49. Repetitive waveforms of (a) laser power, (b) FBGPI reflectance (c) reference FFPI reflectance, (d) reference FFPI phase shift. In (c), the temperature induced amplitude increment (Δamp) is marked for two waveforms.

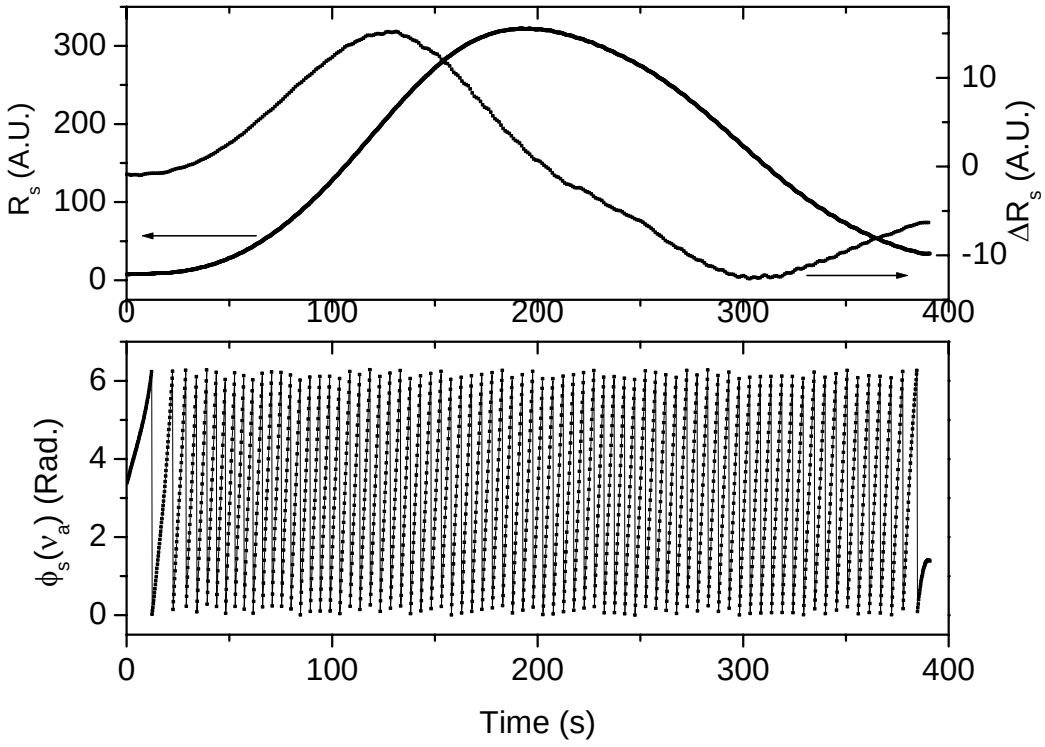


Fig. 50., Plots of the average FBG sensor reflectance Rs, the reflectance difference between two adjacent fringes ΔRs, and the sensor phase shift $\phi_s(\nu_a)$ as a function of time, as the temperature increases from 24 $^{o}$C to 367 $^{o}$C.

During heating from 24 $^{o}$C to 367 $^{o}$C, the data acquisition program (in Labview) simultaneously calculates the sensor average reflectance and phase shift by applying eq. (6.4). Fig. 50 shows the results recorded every 0.2 second. Because of the nearly linearly

increasing temperature, the reflectance curve in Fig. 50(a) shows similarity with the reversed spectrum profile in Fig. 47(a). The maximum reflectance point at the temperature ~ 180 $^{o}$C divides the rising edge and falling edge into two separate measurement regions which allow the temperature to be determined from the reflectance. In order to connect these two regions and double the measurement range, the derivative of reflectance vs laser wavelength is determined from the original data in Fig. 49(b). The derivative is found proportional to the average reflectance difference between two adjacent fringes:

$$\begin{aligned}\Delta A_s &= \frac{\tau}{2\pi}\int_{2\pi/\tau}^{4\pi/\tau} R_s \cdot \exp(-i\tilde{\phi}_r\tau)\, d\tilde{\phi}_r \\ &\quad - \frac{\tau}{2\pi}\int_{0}^{2\pi/\tau} R_s \cdot \exp(-i\tilde{\phi}_r\tau)\, d\tilde{\phi}\end{aligned}, \tag{6.5}$$

where each integral term covers one full interference fringe of the sensor. Appling the discrete data set, eq. (6.5) can be calculated as:

$$\begin{aligned}\Delta A_s &= \frac{\tau}{4\pi}\sum_{\tilde{\phi}_r{}^k=2\pi}^{4\pi/\tau} R_s^k \cdot \exp(-i\tilde{\phi}_r{}^k\tau)(\tilde{\phi}_r{}^{k+1} - \tilde{\phi}_r{}^{k-1}) \\ &\quad - \frac{\tau}{4\pi}\sum_{\tilde{\phi}_r{}^k=0}^{2\pi/\tau} R_s^k \cdot \exp(-i\tilde{\phi}_r{}^k\tau)(\tilde{\phi}_r{}^{k+1} - \tilde{\phi}_r{}^{k-1})\end{aligned}. \tag{6.6}$$

The result of eq. (6.6) is also plotted in Fig. 50(a). Evidently, the rising edge and falling edge of the $A_s$ curve become distinguishable, because $\Delta A_s$ is in the positive and negative regions respectively.

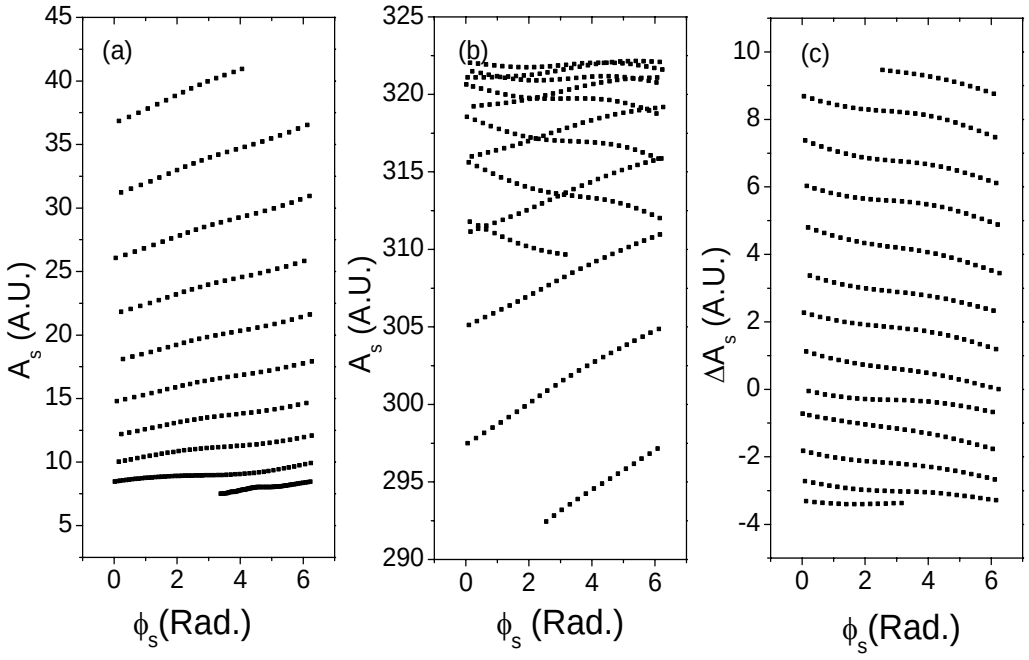


Fig. 51. (a) Fringes where $A_s$ is low at near 24 $^{o}$C; (b) Fringes where $A_s$ approaches toward maximum at near 180 $^{o}$C; (c) Fringes where $\Delta A_s$ crosses zero at near180 $^{o}$C.

In Fig. 50(b), the phase shift results provide the fine determination of temperature. However, the figure also clearly illustrates the ambiguity problem among fringes. To prove that the information in Fig. 50(a) can resolve the ambiguity problem, portions of the data in Fig. 50 are redrawn in Fig. 51, where the phase shift serves as the horizontal axis. In Fig. 51(a), $A_s$ is distinct between adjacent fringes within the temperature region near 24 $^{o}$C. In Fig. 51(b), the sensitivity of $A_s$ becomes low when it approaches the peak value at the temperature near 180 $^{o}$C, such that the top 3~4 fringes

are not distinguishable. However, within the same temperature region in Fig. 51(b), Fig. 51(c) shows that $\Delta A_s$ is distinct between adjacent fringes. Combining $A_s$ and $\Delta A_s$ information, the fringe order can be assigned for every point over the whole temperature region, thus the ambiguity problem is completely removed. Fig. 52 shows that the resultant phase shift is close to a linear function of thermocouple temperature reading. Every $2\pi$-radian phase shift corresponds to ~ 4.6 $^{o}$C temperature change.

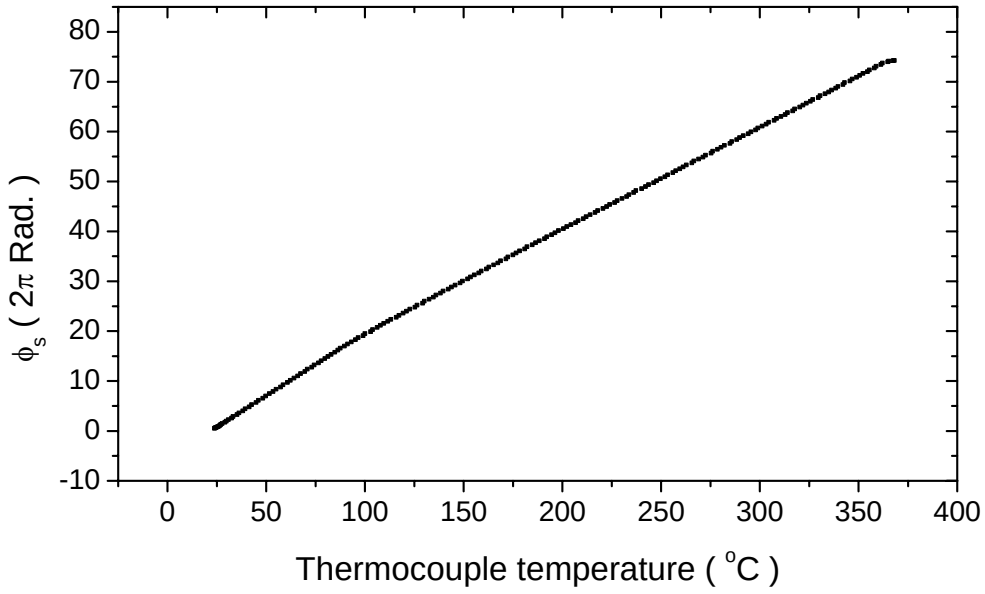


Fig. 52. The resultant phase shift as a function of temperature.

During a system resolution test, the phase shift is determined for 160 consecutive modulation cycles and plotted in Fig. 53. The RMS resolution is determined as 0.005 radian, corresponding to a 0.004 $^{o}$C temperature variance.

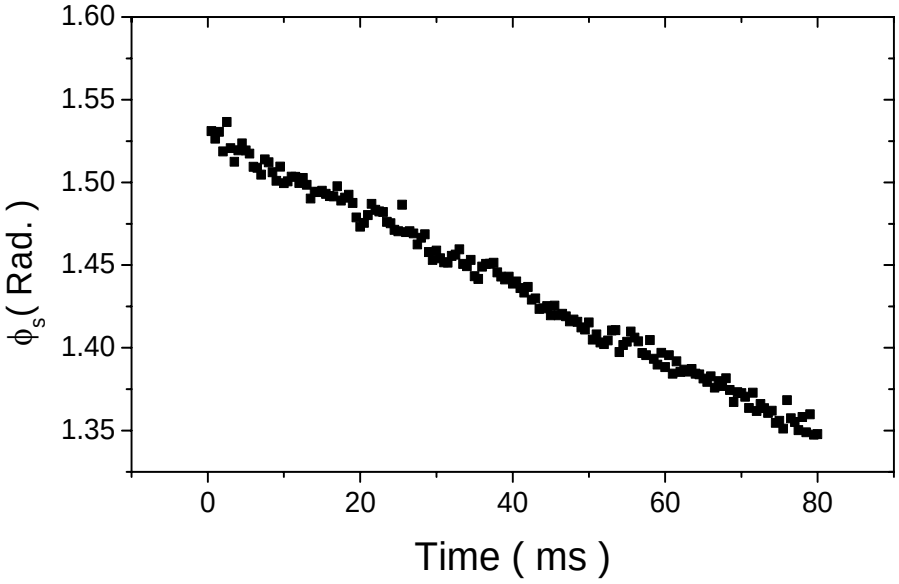


Fig. 53. Obtained phase shift for 160 consecutive modulation cycles. The slope in the phase shift vs. time plot corresponds to a rate of temperature decrease of ~1.6 $^{o}$C/sec.

In conclusion, we present a simple and cost effective technique with fast response to measure temperature. Short FBGs are used to form the two mirrors of an FBGPI sensor, so that the mirror reflectances change gradually as a function of temperature. Modulating the drive current of a DFB laser produces chirping of the laser frequency to scan over ~2.5 fringes of the FFPI reflectance spectrum. Because the fringes are distinguished due to the FBG reflectance change, the ambient temperature can be determined over the range from 24 $^{o}$C to 367 $^{o}$C with a resolution of 0.004 $^{o}$C.

## 6.3. Multiplexing of FBGPI sensors with a linearly chirped fiber laser

Because of the wavelength-encoded nature of the FBG sensors, wavelength division multiplexing (WDM) of FBG sensor is straightforward and attractive. There have been two WDM schemes to monitors an array of FBG sensors: (1) broadband light source and a spectrometer for signal demodulation,[32] and (2) wide band tunable laser as a combination of light source and spectrum analyzer.[75] In such a system, crosstalk between neighboring sensors generally should be avoided, unless the individual sensor spectral profiles can be distinguished from an overlapped spectral signal.[81,82] Therefore, in a conventional WDM system, the maximum number of sensors is limited by the ratio of the light source spectral width (or tuning range) over the bandwidth allocated to each sensor. In this research, a new FBG sensing scheme is introduced to provide improved measurement sensitivity for individual sensing elements and enhanced multiplexing capacity by allowing multiple sensors to share the same regime of the optical spectrum.

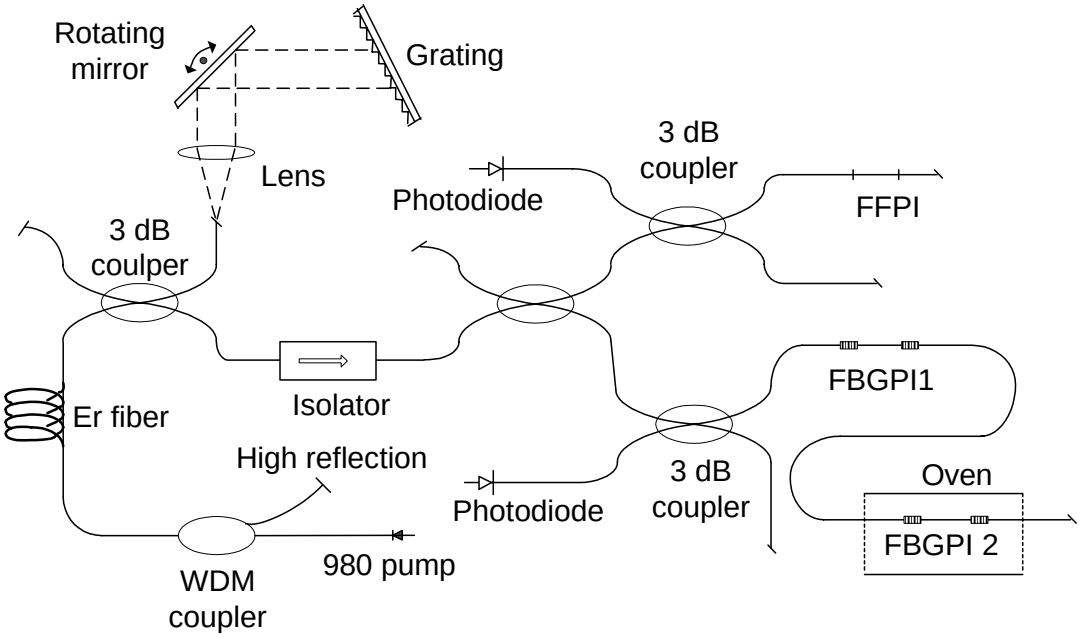


Fig. 54. Experimental arrangement to multiplexing two FBGPIs.

The experimental arrangement is shown in Fig. 54. The light source is a linearly chirped erbium-doped fiber laser, with a rotating galvanometer mirror as the tuning element. The laser output power varies < 1 dB over a 46 nm spectral range from 1522 – 1568 nm. The sensing elements are two FBG pair interferometers $FBGPI_1$ and $FBGPI_2$, arranged in series. Mirrors for the two interferometers are ≈ 2 mm long sections (reflectance peak wavelength of 1528.3 nm, maximum reflectance ≈ 1%, spectral full width at half maximum ≈ 2.3 nm) cut from a single 2 cm commercial FBG with a peak reflectance of almost 100% and a spectral width of about 1 nm. Cavities for the FBGPIs are formed by sections of single mode telecommunications fiber of lengths $L_1$ = 12.0 mm and $L_2$ = 14.5 mm.

Another interferometer, a fiber Fabry Perot interferometer (FFPI),[10] is used to monitor the chirp rate of the laser and correct for nonlinearities in that chirp rate in processing the FBGPI signals. Internal dielectric mirrors for the FFPI, each with a reflectance of about 5 %, are formed in a continuous length of single mode fiber by a fusion splicing technique.

Fig. 55 shows the reflected FFPI reference signal and the sensor signal as a function of time during a portion of a modulation cycle of the laser. The data acquisition rate was 20 KHz. The laser frequency range of 1100 GHz in Fig. 55 corresponds to a wavelength tuning of 8.6 nm. The modulation depth for the sinusoidal FFPI signal in Fig. 55(a) is practically constant over the spectral range because the internal mirror reflectance is almost independent of the optical frequency, while the grating sensor signals in Fig. 55(b) - (d) show the spectral dependence of the FBG reflectance superimposed upon sinusoidal modulation. At room temperature the reflectance spectra for the two sensors nearly coincide. Heating of $FBGPI_2$ causes its reflectance envelope to shift to longer wavelengths until, at 360°C, there is almost no overlap in the spectra.

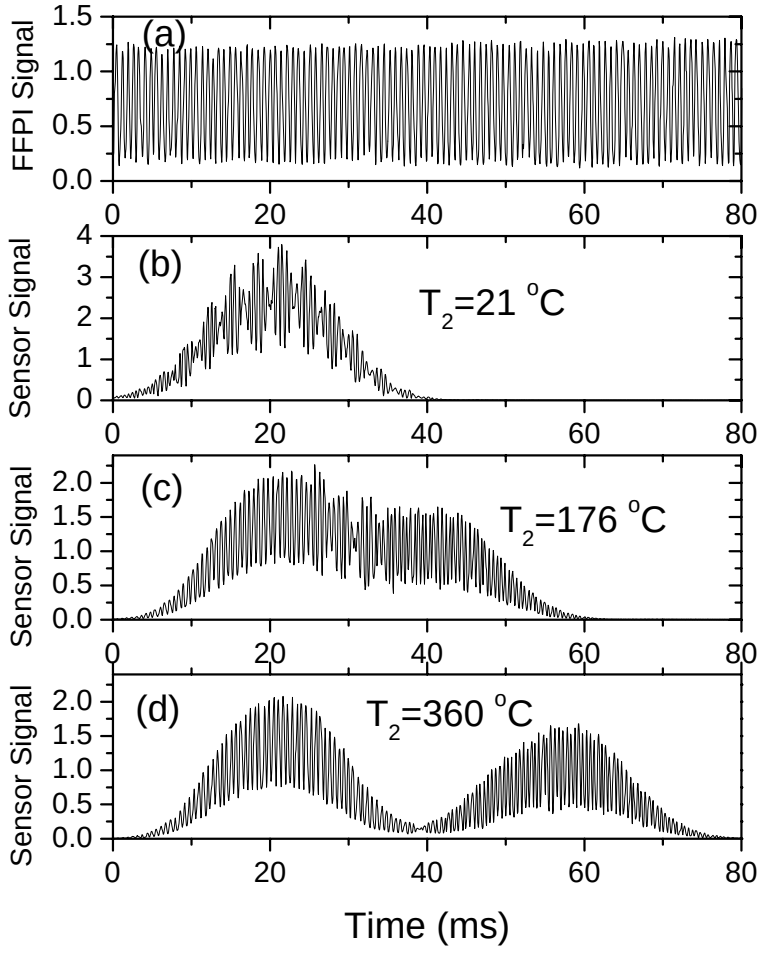


Fig. 55. Comparison of FFPI reflected signal (a) with reflected sensor waveform when the FBGPI spectra are (b) overlapped; (c) partially overlapped; (d) separated.

The FFPI reference signal, used to monitor the laser frequency and correct for nonlinearities in the chirp rate, is given by

$$R_r = r_a + r_b + 2(r_a r_b)^{1/2}\cos(4\pi nL\nu/c), \qquad (6.7)$$

with $r_a$ and $r_b$ the mirror reflectances, n the effective refractive index of the fiber mode, L the cavity length, ν the optical frequency, and c the free space speed of light. This expression assumes that $r_a$ and $r_b$ are both << 1. Defining a fixed frequency $\nu_0$, the laser chirping introduced phase shift $\tilde{\phi}_r = 4\pi n_r L_r(\nu - \nu_0)/c$ can be determined from the reference signal in Fig. 55(a).

The reflectance signal $R_s$ from the FBGPIs can be written

$$R_s = \sum_j \left[ r_{ja} + r_{jb} + 2(r_{ja} r_{jb})^{1/2} \cos(4\pi n_j L_j \nu / c) \right] \tag{6.8}$$

with $n_j L_j$, the optical length of the j'th FBGPI. This is similar to the expression (6.1) for FFPI reflectance, but now the individual mirror reflectances $r_{ja}$ and $r_{jb}$ for $FBGPI_j$ have a strong dependence on optical frequency.

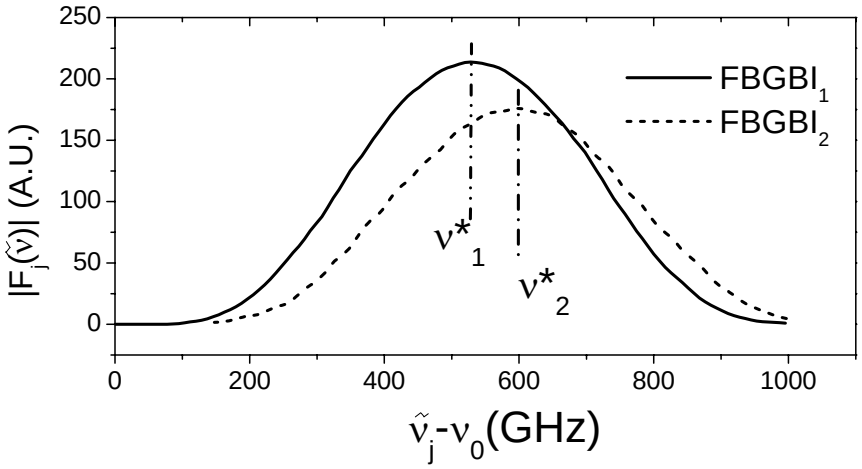


Fig. 56. Calculated $|F_j(\tilde{\nu})|$ for the data in Fig. 45(b).

A coarse measurement of the spectral position of the reflectance peak for the j'th sensor is obtained by convolving the sensor signal $R_s$, as shown in Fig. 55(b) -(d), with a

complex function $\exp(-i\eta_j\tilde{\phi}_r)$, where the constant $\eta_j$ approximately equals to the sensor-reference optical length ratio $n_jL_j/n_rL_r$. The convolution

$$\begin{aligned} F_j(\tilde{\nu}) &= \int_{\tilde{\nu}-\Delta/2}^{\tilde{\nu}-\Delta/2} R_s \exp(-i\eta_j\tilde{\phi}_r)d\nu \\ &\approx \exp(i4\pi n_j L_j \nu_0/c)\int_{\tilde{\nu}-\Delta/2}^{\tilde{\nu}-\Delta/2} (r_{ja}r_{jb})^{-1/2} d\nu \end{aligned} \tag{6.9}$$

is evaluated over a frequency range Δ. The magnitude of the integral peaks at the optical frequency $\nu^*_j$ at which the product of $r_{ja}$ and $r_{jb}$ is a maximum, as shown in Fig. 56. But

$$\nu^*_j = c/2n_j\Lambda_j, \tag{6.10}$$

with $\Lambda_j$ the spatial period of the FBGs for the j'th sensor. In addition, the phase $\phi_j$ of the j'th sensor signal at the frequency $\nu_0$ is

$$\phi_j = \tan^{-1}[\mathrm{Im}(F_j)/\mathrm{Re}(F_j)], \tag{6.11}$$

Assuming that the measurand is experienced uniformly over the length of the FBGs and of the fiber in between, it can be shown that

$$\delta\nu^*_j/\nu^*_j = -\delta\phi_j/\phi_j. \tag{6.12}$$

Thus, the magnitude and phase part of the convolution independently provides two ways of determining the position of spectral reflectance peak.

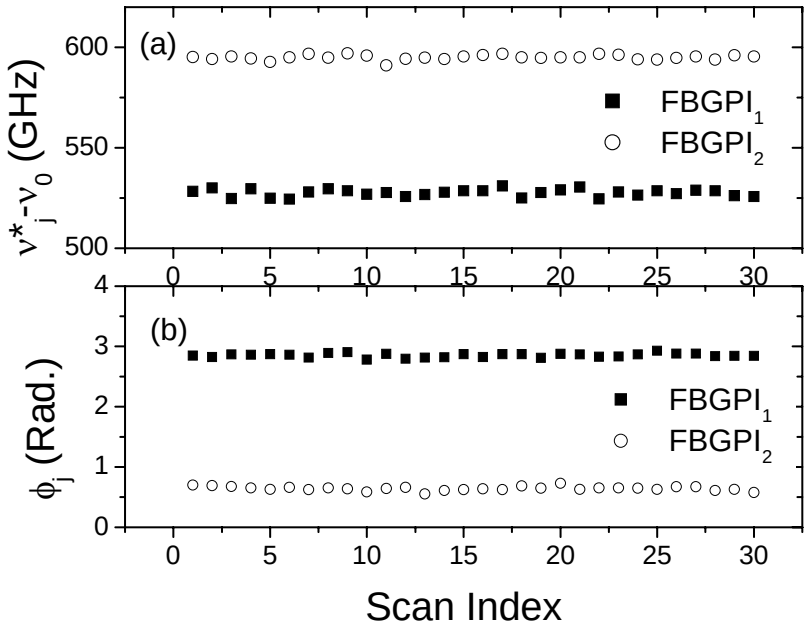


Fig. 57. Results of repetitive measurements of (a) spectral peak position and (b) phase shift for the two FBGPI's at constant temperature.

Fig. 57 gives the calculated variation in the reflectance peak frequency, as determined from the function $|F_j(\tilde{\nu})|$, and the phase shift as determined from eq. (6.11), for 30 consecutive laser scans. As shown in Table 3, analysis of these data shows that the reflectance peak frequency determined using the phase shift data is nearly two orders of magnitude more precise than that obtained using a direct measurement.

Table 3. RMS deviation based on the Spectral peak position (SPP) calculation and the phase shift (PS) calculation. $2\pi$ in phase shift corresponds to one free spectrum range in frequency.

| Sensor | Method | $\Delta\nu^*_1$ (GHz) | $\Delta\phi_1$ ($2\pi$) |
|---|---|---|---|
| $FBGPI_1$ | SPP | 1.7 | 0.21 |
| | PS | 0.045 | 0.0052 |
| $FBGPI_2$ | SPP | 1.1 | 0.15 |
| | PS | 0.04 | 0.0057 |

Finally, Fig. 58 compares the reflectance peak frequency obtained directly with that deduced from a phase shift measurement when $FBGPI_2$ was cooled at a constant rate from 141.4 $^oC$ to 126.4 $^oC$. The benefit in accuracy from using the phase shift data is evident. However, the use of phase shift data alone limits the unambiguous dynamic range to $2\pi$ rad, which corresponds to 7.3 GHz in peak reflectance frequency or 4.5 $^oC$ in temperature, if the signal processing is initiated from a "cold start". However, by applying both the directly measured reflectance peak frequency and the phase shift data the dynamic range of the sensor can be extended to the laser scanning range, while retaining the high precision of the phase shift measurement. In the case of the data shown in Fig. 58 this is possible because, as indicated in Table 3, the equivalent phase shift uncertainty for the direct reflectance measurement is << 2 $\pi$ rad (21% of $2\pi$ for $FBGPI_1$ and 15% of $2\pi$ for $FBGPI_2$).

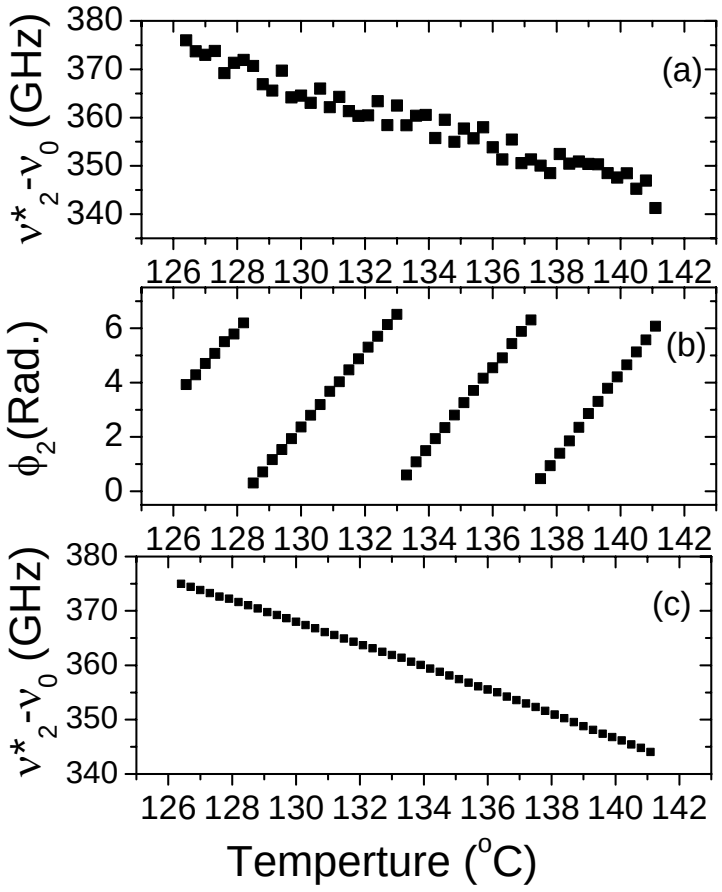


Fig. 58. As $FBGPI_2$ is cooling at a constant rate, comparison of direct measured spectral peak position (a) with resultant spectral peak position (c) using phase shift (b).

In conclusion, a new technique for the monitoring and multiplexing of FBG sensors is described. The sensing elements are low-finesse Fabry-Perot interferometers formed using Bragg grating mirrors with similar spectral characteristics. The sensors are reflectively monitored with an erbium-doped fiber laser which is linearly scanned in optical frequency. The resulting signal from an interferometer varies sinusoidly with

time, at a frequency proportional to its optical length. The sensor signal is convolved with in-phase and quadrature components of a reference waveform corresponding to an interferometer of approximately the same length to obtain a coarse measurement of the optical frequency corresponding to the FBG reflectance peak, and refine this measurement to a higher level of precision, using the phase of the convolved signal. The signal from a fiber Fabry Perot interferometer (FFPI) is used to compensate the data for variations in the laser scan rate. Multiplexing of two interferometers of different lengths used as temperature sensors was demonstrated. Their signals were distinguished through convolution with appropriately matched reference waveforms, even though the reflectance spectra for the FBGs for the two sensors overlap over a wide temperature range. For temperature measurement with two multiplexed sensors, a spectral resolution for the FBG reflectance peak of 0.045 GHz (0.36 pm), corresponding to a temperature resolution of 0.035 $^{o}$C, has been achieved.

# VII. CONCLUSIONS

In conclusion, a wide band linearly chirped erbium-doped fiber laser has been developed. Several new techniques for the monitoring and multiplexing of fiber Bragg grating (FBG), fiber Fabry-Perot interferometer (FFPI) and fiber Bragg grating pair interferometer (FBGPI) sensors have been investigated using this laser. A chirped distributed feedback (DFB) laser is applied to the monitoring of a single FBGPI sensor. High resolution and large dynamic range have been achieved for temperature measurement.

The erbium-doped fiber laser using a rotating mirror/grating combination as one of the reflectors in a Fabry-Perot laser cavity has been tuned over a 46 nm spectral range. Linearization of the chirp rate has been achieved using feedback from an FFPI to adjust the voltage ramp which drives the rotating mirror. This method represents a simple and relatively inexpensive alternative to the optical spectrum analyzer in some spectroscopy applications. In a demonstration of the monitoring an array of two FBG sensors, a wavelength resolution of 1.7 pm has been achieved.

It has been shown that the linearly chirped fiber laser can be used in measuring the optical path difference (OPD) of interferometric fiber optic sensors by performing a Fourier transform of the optical signal. This is an application of the frequency modulated continuous wave (FMCW) technique first applied in radar system. A coarse determination of the OPD is obtained by measuring the position of the peak of the absolute square of the Fourier transform amplitude, while fine resolution is obtained from the phase of the Fourier transform. Multiplexing of an array of three FFPI sensors of different lengths has been demonstrated, with an OPD resolution ranging from 3.6 nm to 6.3 nm. Temperature was measured with one of the sensors over the range from 20°C to 610°C with a 0.02°C resolution.

A simple and cost effective technique of monitoring an FBGPI sensor with a chirped DFB laser has been introduced for temperature measurement. Short FBGs are

used to form the two mirrors of an FBGPI sensor, so that the mirror reflectances change gradually as a function of temperature. Modulating the drive current of the DFB laser produces chirping of the laser frequency to scan over ~2.5 fringes of the FBGPI reflectance spectrum. Because the fringes are distinguished due to the FBG reflectance change, the ambient temperature can be determined over the range from 24 $^{o}$C to 367 $^{o}$C with a resolution of 0.004 $^{o}$C.

Multiplexing of FBGPI sensors of different lengths with a linearly chirped fiber laser has demonstrated improved sensitivity and multiplexing capacity over a conventional FBG WDM system. The FBG spectral peak position and the phase shift of an FBGPI are determined through the convolution of the sensor reflected signal with an appropriately matched reference waveform, even though the reflectance spectra for the FBGs of multiple FBGPI sensors overlap over a wide temperature range. For temperature measurement with two multiplexed sensors of different lengths, a spectral resolution for the FBG reflectance peak of 0.045 GHz (0.36 pm), corresponding to a temperature resolution of 0.035 $^{o}$C, has been achieved.

Table 4. Comparison of prior results of monitoring interferometric fiber optic sensors by the FMCW technique with those reported here (shaded).

| Sensor/Chirped laser | Resolution (fringe) | Dynamic Range |
|---|---|---|
| FFPI / Diode laser[2] | 1/1000 | $10^3$ |
| FI/ Diode laser[64] | $10^4$ | $5\times10^3$ |
| FFPI / Fiber laser[6] | 1/3000 | $6\times10^7$ |
| FBGPI / Fiber laser[8] | 1/200 | $5\times10^6$ |

FI: fiber interferometer.

Table 4 summarizes the performance of FMCW techniques for monitoring interferometer sensors reported here with some previously reported results. The large

improvement in dynamic range for the present results is a consequence of the broad (46 nm) tuning range of the erbium-doped fiber laser and the compensation scheme for linearizing the chirp rate. Although the techniques reported here are characterized for temperature measurement only, with appropriate packaging of the sensing elements they can be used for measurands such as strain and pressure as well. Cost-effective systems can be developed for a variety of applications. Examples include downhole measurement of temperature and pressure in oil and gas wells, and strain measurement on railroad and highway bridges and the hulls of ships.

# VIII. SUGGESTIONS FOR FUTURE RESEARCH

## 8.1. Fast tunable fiber laser

In the demonstrated sensing experiments using the linearly chirped fiber laser, the tuning repetition rate is less than 5 Hz. They are fast enough for temperature measurement or other static measurements. However, this laser can also be very useful for other sensing applications requiring fast tuning rate, such as dynamic strain sensors and optical coherence tomography.

The rotating mirror in Fig. 22 can be operated at up to 1 kHz, and high speed data acquisition hardware is also available to process the data. However, we have observed that the instantaneous linewidth increases with faster tuning speed, such that the interference visibility of a 10-mm long FFPI becomes too low for processing at a repetition rate higher than 30 Hz. Therefore, to narrow the laser linewidth, the tuning element has to be redesigned so that it will have narrower reflectance bandwidth. One approach is to increase focal length of the lens in Fig. 22. For instance, if the focal length increases from 5 cm to 10 cm, the reflectance bandwidth can be reduced from 0.3 nm to 0.15 nm. Another approach is to use a tunable fiber Fabry-Perot filter. To achieve 0.15 nm transmission bandwidth over a 60 nm tuning range, a fiber Fabry-Perot with finesse of over 400 must be used. A fiber Fabry-Perot filter can also be tuned at up to a few hundred Hz.

## 8.2. Q-switched and mode-locked fiber laser

Time division multiplexing (TDM) is an important technique for multiplexing optic fiber sensors, and it is briefly introduced in section 2.5.3. By modifying the linearly chirped fiber laser sources, it is possible to combine TDM with our reported multiplexing techniques such that the total multiplexing capacity can be considerably increased. Moreover, because the FFPI and FPGPI sensors can be made with very low

reflectance, they are suitable for serially connecting a large number of sensors along a single fiber cable.

Q-switching can be applied to generate a laser pulse train for the implementation of TDM. By connecting an electro-optical modulator inside the laser cavity, Q-switched laser pulses can be generated when the switch is opened and then closed. In order to achieve a spatial resolution of 100 m, the gate-open speed should be optimized to obtain a desired pulse width of less than 1 μs. On the one hand, a shorter gate-opening time will generally produce a narrower Q-switched pulse. On the other hand, when the open gate time is short enough and becomes comparable to the cavity roundtrip time, ~200 ns, undesired incomplete mode-locked spikes will occur.[83] The repletion rate of the Q-switch can be adjusted according to the range of the distributed fiber sensors. For instance, a repetition rate less than 100 kHz can be used for monitoring fiber sensors within a1 km range.

Another approach to obtain pulse trains is to apply a mode-locking technique. As an example of active mode-locking, an in-cavity electro-optical switch is modulated harmonically at a frequency of the longitudinal mode spacing, such that a single pulse is traveling inside the laser cavity. Because an output pulses occur once every roundtrip time, the cavity length can be adjusted to achieve a pulse train at the desired repetition rate. For instance, by connecting a 1 km-long fiber inside the laser cavity, the laser can be used for monitoring fiber sensors within a 1 km range.

# REFERENCES


1. C.E. Lee and H.F. Taylor, "Interferometric optical fibre sensors using internal mirrors," Electron. Lett. **24**, 193-194 (1988).
2. R. Sadkowski, C. E. Lee and H. F. Taylor, "Multiplexed interferometric fiber-optic sensors with digital signal processing," Appl. Opt. **34**, 5861-5866 (1995).
3. H.S. Choi, C.E. Lee and H.F. Taylor, "High-performance fiber optic temperature sensor using low-coherence interferometry," Opt. Lett. **22**, 1814-1816 (1997).
4. K. O. Hill, Y. Fuji, D. C. Johnson, and B.S. Sawasaki, "Photo-sensitivity in optical fiber waveguides: Application to reflection filter fabrication," Appl. Phys. Lett. **32**, 647-649 (1978).
5. X. Wan, and H. F. Taylor, "Linearly chirped erbium-doped fiber laser," IEEE Photon. Technol. Lett. **15**, 188-190 (2003).
6. X. Wan, and H. F. Taylor, "Monitoring and multiplexing technique for interferometric fiber optic sensors using a linearly chirped Er:Fiber laser," Appl. Opt. **41**, 7607-7611 (2002).
7. X. Wan, and H. F. Taylor, "Intrinsic fiber Fabry-Perot temperature sensor with fiber Bragg grating mirrors," Opt. Lett. **27**, 1388-1390 (2002).
8. X. Wan, and H. F. Taylor, "Fiber Bragg grating pair interferometer with improved multiplexing capacity and high resolution," IEEE Photon. Technol. Lett., (to appear)
9. S.J. Petuchowski, T.G. Giallorenzi, and S.K. Sheem. A Sensitive fiber-optic Fabry-Perot interferometer. IEEE J. Quantum Electron. **17**, 2168-2170 (1981).
10. T. Yoshino, K. Kurosawa, K. Itoh, and T. Ose, "Fiber-optic Fabry-Perot interferometer and its sensor applications," IEEE J. Quantum Electron. **18**, 1624-1633 (1982).

11. C. E. Lee, J. J. Alcoz, Y. Yeh, W. N. Gibler, R.A. Atkins, and H.F. Taylor, Smart Mater. Struct. **1**, 123 (1992).
12. R. A. Atkins, J. H. Gardner, W. N. Gibler, C. E. Lee, M. D. Oakland, M. O. Spears, V. P. Swenson, H. F. Taylor, J. J. McCoy, and G. Beshouri, "Fiber optic pressure sensors for internal combustion engines," Appl. Opt. **33**, 1315-1320 (1994).
13. J. F. Dorighi, S. Krishnaswamy, and J. D. Achenbach, "Stabilization of an embedded fiber optic Fabry-Perot sensor for ultrasound detection," IEEE Trans. Ultrason., Ferroelectron., and Freq. Contr. **42**, 820-824 (1995).
14. G. Beheim, "Remote displacement measurement using a passive interferometer with a fiber optic link," Appl. Opt. **24**, 2335-2340 (1985).
15. C.E. Lee and H.F. Taylor, "Fiber-optic Fabry-Perot temperature sensor using a low-coherence light source," J. Lightwave Technol. **9**, 129-134 (1991).
16. S. Chen, K. T. V. Grattan, B. T. Meggitt, and A. W. Palmer, "Instantaneous fringe-order identification using dual broadband sources with widely spaced wavelengths," Electron. Lett. **29**, 334-335 (1993).
17. Y. J. Rao, Y. N. Ning, and D. A. Jackson, "Synthesized source for white-light systems," Opt. Lett. **18**, 462-464 (1993).
18. Y. J. Rao, and D. A. Jackson, "A prototype multiplexing system for use with a large number of fiber-optic-based extrinsic Fabry-Perot sensors exploiting coherence interrogation," Proc. SPIE **904**, 114, (1995).
19. V. Bhatia, K. A. Murphy, R. O. Claus, M. E. Jones, J. L. Grace, T. A. Tran, and J. A. Greene, "Optical fibre based absolute extrinsic Fabry-Perot interferometric sensing system," Meas. Sci. Technol. **7**, 58-61 (1996).
20. K. O. Hill, Y. Fuji, D. C. Johnson, and B.S. Sawasaki, "Photo-sensitivity in optical fiber waveguides: Application to reflection filter fabrication," Appl. Phys. Lett. **32**, 647-649 (1978).
21. G. Meltz, W. W. Morey, and W, H. Glenn, "Formation of Bragg gratings in optical fibers by a transverse holographic method," Opt. Lett. **14**, 823-825 (1989).

22. D. K. W. Lam, and B. K. Garside, "Characterization of single-mode optical fiber filters," Appl. Opt. **20**, 440-445 (1981).
23. J. Albert, K. O. Hill, B. Malo, S. Theriault, F. Bilodeau, D. C. Johnson, and L. E. Erickson, "Apodisation of the spectral response of fibre gratings using a phase mask with variable diffraction efficiency," Electron. Lett. **31**, 222-223 (1995).
24. C. R. Giles, T. Erdogan, and V. Mizrahi, "Reflection-induced changes in the optical spectra of 980 nm QW lasers," IEEE Photon. Technol. Lett. **6**, 903-906 (1994).
25. B. F. Ventrudo, G. A. Rogers, G. S. Lick, D. Hargreaves, and T. N. Demayo, "Wavelength and intensity stabilization of 980 nm diode lasers coupled to fiber Bragg gratings," Electron. Lett. **30**, 2147-2149 (1994).
26. J. L. Zyskind, J. W. Sulhoff, P. D. Magill, K. C. Reichmann, V. Mizrahi, and D. J. DiGiovanni, "Transmission at 2.5 Gbit/s over 654 km using an erbium-doped fiber grating laser source," Electron. Lett. **29**, 1105-1106 (1993).
27. F. Bilodeau, K. O. Hill, S. Faucher, and D. C. Johnson, "Low-loss highly overcoupled fused coupler: Fabrication and sensitivity to external pressure," IEEE J. Lightwave Technol. **6**, 1476-1482 (1988).
28. F. Ouellette, "Dispersion cancellation using linearly chirped Bragg grating filters in optical waveguides," Opt. Lett. **12**, 847-849 (1987).
29. A. D. Kersey, M. A. Davis, H. J. Patrick, M. Leblanc, K. P. Koo, C. G. Askins, M. A. Putnam, and E. J. Friebele, "Fiber grating sensors," IEEE J. Lightwave Technol. **15**, 1442-1463 (1997).
30. S. M. Melles, K. Liu, and R. M. Measures, "A passive wavelength demodulation system for guided-wave Bragg grating sensors," IEEE Photon. Technol. Lett. **4**, 516-518 (1992).
31. M. A. Davis, and A. D. Kersey, "All-fibre Bragg grating strain-sensor demodulation technique using a wavelength division coupler," Electron. Lett. **30**, 75-77 (1994).
32. A. D. Kersey, T. A. Berkoff, and W. W. Morey, "Multiplexed fiber Bragg grating strain-sensor system with a fiber Fabry-Perot wavelength filter," Opt. Lett. **18**, 1370-1372 (1993).

33. M. G. Xu, H. Geiger, J. L. Archambault, L. Reekie, and J. P. Dakin, "Novel interrogation system for fibre Bragg grating sensors using an acousto-optic tunable filter," Electron. Lett. **29**, 1510-1511 (1993).
34. D. A. Jackson, A. B. L. Ribeiro, L. Reekie, and J. L. Archambault, "Simple multiplexing scheme for fiber-optic grating sensor network," Opt. Lett. **18**, 1192-1194 (1993).
35. A. D. Kersey, T. A. Berkoff, and W. W. Morey, "Fiber-optic Bragg grating strain sensor with drift-compensated high resolution interferometric wavelength-shift detection," Opt. Lett. **18**, 72-74 (1993).
36. T. A. Berkoff, A. D. Kersey, "Fiber Bragg grating array sensor system using a bandpass wavelength division multiplexer and interferometric detection," IEEE Photon. Tech. Lett. **8**, 522-525 (1996).
37. P. C. Becker, N. A. Olsson, J. R. Simpson, "Erbium-doped fiber amplifiers: fundamentals and technology," (Academic press, San Diego, CA, 1997), pp. 110-112.
38. V. P. Gapontsev, S. M. Matitsin, A. A. Isinev, and V. B. Kravchenko, "Erbium glass lasers and their applications," Opt. Laser Tech. **14**, 189-196 (1982).
39. D. E. McCumber, Phys. Rev. **174**, 429 (1968).
40. W. J. Miniscalco and R. S. Quimby, "General procedure for the analysis of $Er^{3+}$ cross sections," Opt. Lett. **16**, 258-260 (1991).
41. J. Stone and C. A. Burrus, "Neodymium-doped silica lasers in en-pumped fiber geometry," Appl. Phys. Lett. **23**, 388-389 (1973).
42. J. Stone and C. A. Burrus, "Neodymium-doped fiber lasers – room temperature cw operation with an injection laser pump," Appl. Opt. **13**, 1256-1258 (1974).
43. R. J. Mears, L. Reekie, S. B. Poole, and D. N. Payne, "Neodymium-doped silica single mode fiber lasers," Electron. Lett. **23**, 738-740 (1985).
44. C. R. O Cochlain, and R.J. Mears, "Broadband tunable single frequency diode-pumped erbium doped fibre laser," Electron. Lett. **28**, 124-126 (1992).

45. J. L. Zyskind, J. W. Sulhoff, J. Stone, D. J. Digiovanni, L. W. Stulz, H. M. Presby, A. Piccirilli, P. E. Pramayon, "Electrically tunable, diode-pumped erbium-doped ring laser with fibre Fabry-Perot etalon," Electron. Lett. **27**, 1950-1951 (1991).
46. Y. C. Chung, R. M. Derosier, H. M. Presby, C. A. Burrus, Y. Akai, and N. Masuda, "A 1.5-μm laser package frequency-locked with a novel miniature discharge lamp," IEEE Photon. Technol. Lett. **3**, 841-844 (1991).
47. N. Park, J. W. Dawso, and K. J. Vahala, "Frequency locking of an erbium-doped fiber ring laser to an external fiber Fabry-Perot resonator," Opt. Lett. **18**, 879-981 (1993).
48. Y. T. Chieng and R. A. Minasian, "Tunable erbium-doped fiber laser with a reflection Mach-Zehnder interferometer," IEEE Photon. Technol. Lett. **6**, 153-156 (1994).
49. Y. W. Song, S. A. Havstad, D. Starodubov, Y. Xie, A. E. Willner, and J. Feinberg, "40-nm-wide fiber ring laser with single-mode operation using a highly stretchable FBG," IEEE Photon. Technol. Lett. **13**, 1167-1169 (2001).
50. Y. T. Chieng, G. J. Cowle and R. A. Minasian, "Optically amplitude-stabilised tunable erbium-doped fibre laser with <20μs tuning speed," Electron. Lett. **31**, 1451-1452 (1995).
51. Y. T. Chieng, G. J. Cowle, "Relaxation oscillation suppression in tunable fibre lasers," Electron. Lett. **18**, 1419-1420 (1994).
52. Y. T. Chieng, G. J. Cowle and R. A. Minasian, "Optimization of wavelength tuning of erbium-doped fiber ring lasers," J. Lightwave Technol. **14**, 1730-1739 (1996).
53. G. A. Ball, W. W. Morey, "Continuously tunable single-mode fiber laser," Opt. Lett. **17**, 420-422 (1992).
54. P. Oberson, B. Huttner, O. Guinnard, L. Guinnard, G. Ribordly, and N. Gisin, "Optical frequency domain reflectometry with a narrow linewidth fiber laser," IEEE Photon. Technol. Lett. **12**, 867-869 (2000).
55. S. P. Fang, and H. F. Taylor, "High-performance single-mode fiber-optic switch," Opt. Lett. **19**, 1204-1206 (1994).

56. G. Beheim, “Remote displacement measurement using a passive interferometer with a fiber optic link,” Appl. Opt. **24**, 2335-2340 (1985).
57. Y. Chen and H. F. Taylor, “Multiplexed fiber Fabry-Perot temperature sensors system using white light interferometry,” Opt. Lett. **27**, 903-905 (2002).
58. C. M. Davis, C. J. Zarobila, and J. D. Rand, “Fiber-optic temperature sensor for microwave environments,” in *Optical Fibers in Medicine III,* A Katzir ed., Proc. SPIE **906**, 114-118 (1988).
59. M. Singh, C. J. Tuck, and G. F. Fernando, “Multiplexed optic fiber Fabry-Perot sensors for strain metrology,” Smart Mater. Struct. **8**, 549-553 (1999).
60. S. C. Kaddu, S. F. Collins, and D. J. Booth, “Multiplexed intrinsic optical fibre Fabry-Perot temperature and strain sensors addressed using white light interferometry,” Meas. Sci. Technol. **10**, 416-420 (1999).
61. I. P. Giles, D. Uttam, B. Culshaw, and D. E. N. Davies, “Coherent optical-fibre sensors with modulated laser sources,” Electron. Lett. **19**, 14-15 (1983).
62. D. Uttam and B. Culshaw, “Precision time domain reflectometry in optical fiber systems using a frequency modulated continuous wave ranging technique,” J. Lightwave Technol. **3**, 971-977 (1985).
63. A. J. Hymans and J. Lait, “Analysis of a frequency-modulated continuous-wave ranging system,” Proc. Inst. Elect. Eng., **107 B**, 365-372 (1960).
64. I. Alasaarela, P. Karioja, and H. Kopola, “Comparison of distributed fiber optic sensing methods for location and quantity information measurements,” Opt. Eng. **41**, 181-189 (2002).
65. K. Tsuji, K. Shimizu, T. Horiguchi, and Y. Koyamada, “Spatial-resolution improvement in long-range coherent optical frequency domain reflectometry by frequency-sweep linearisation,” Electron. Lett. **33**, 408-410 (1997).
66. H. F. Taylor, "Fiber Optic Fabry Perot Sensors," in *Fiber Optic Sensors* F. T. Y. Yu, ed. (Marcel Dekker, New York, 2002), pp 41-74.

67. S. Grosswig, E. Hurtig, K. Kuh, and F. Rudolph, "Distributed fibre-optic temperature sensing technique (DTS) for surveying underground gas storage facilities," Oil Gas Eur. Mag. **27**, 31-34 (2001).
68. T. Unneland, Y. Manin, and F. Kuchuk, "Permanent gauge pressure and rate measurements for reservoir description and well monitoring: Field cases," SPIE Reservoir Eval. Eng. **3**, 224-230 (1988).
69. W. Lee, J. Lee, C. Henderson, H. F. Taylor, R. James, C. E. Lee, V. Swenson, R. A. Atkins, and W. G. Gemeiner, "Railroad bridge instrumentation with fiber optic sensors," Appl. Opt. **38**, 1110-1114 (1999).
70. R. C. Tennyson, A. A. Mufti, S. Rizkalla, G. Tadros, and B. Benmokrane, "Structure health monitoring of innovative bridges in Canada with fiber optic sensors," Smart Mater. Struct. **10**, 560-573 (2001).
71. G. Wang, K. Pran, G. Sagvolden, G. B. Havsgard, A. E. Jensen, G. A. Johnson, and S. T. Vohra, "Ship hull structure monitoring using fibre optic sensors," Smart Mater. Struct. **10**, 472-478 (2001).
72. S. M. Melle, A. T. Alavie, S. Karr, T. Coroy, K. Liu, and R. M. Measures, "A Bragg grating-tuned fiber laser strain sensor system," IEEE Photon. Technol. Lett. **5**, 263-266 (1993).
73. G. A. Ball, W. W. Morey, and P. K. Cheo, "Single- and multipoint fiber-laser sensors," IEEE Photon. Technol. Lett. **5**, 267-270 (1993).
74. G. A. Ball, W. W. Morey, and P. K. Cheo, "Fiber laser source/analyzer for Bragg grating sensor array interrogation," J. Lightwave Technol. **12**, 700-703 (1994).
75. S. H. Yun, D. J. Richarson, B. Y. Kim, "Interrogation of fiber grating sensor arrays with wavelength-swept fiber laser," Opt. Lett. **23**, 843-845 (1998).
76. Y. Yeh, C. E. Lee, R. A. Atkins, W. N. Gilber, and H. F. Taylor, "Fiber optic sensor for substrate temperature monitoring," J. Vac. Sci. Technol. **A8**, 3247-3250 (1990).
77. J. X. Fang and H. F. Taylor, "Accurate monitoring of an interferometric fiber-optic sensor with a multimode semiconductor laser," Opt. Lett. **24**, 522-524 (1999).

78. M. G. Xu, J. L. Archambault, L. Reekie, and P Dakin, “Discrimination between strain and temperature effects using dual wavelength fibre grating sensors,” Electron. Lett**. 30**, 1085-1887 (1994).
79. A.D. Kersey, T. A. Berkoff, and W. W. Morey, “High-resolution fibre-grating based strain sensor with interferometric wavelength-shift detection,” Electron. Lett. **28**, 236-238 (1992).
80. Y. J. Rao, M. R. Cooper, D. A. Jackson, C. N. Pannell, and L. Reekie, “Absolute strain measurement using an in-fiber-Bragg-grating-based Fabry-Perot sensor,” Electron. Lett. **36**, 708-709 (2000).
81. L. Zhang, Y. Liu, J. A. R. Williams, and I. Bennion, “Enhanced FBG strain sensing multiplexing capacity using combination of intensity and wavelength dual coding technique,” IEEE Photon. Technol. Lett. **11**, 1638-1640 (1999).
82. J. M. Gong, J. M. K. MacAlpine, C. C. Chan, W. Jin, M. Zhang, and Y. B. Liao, “A novel wavelength detection technique for fiber Bragg grating sensors,” IEEE Photon. Technol. Lett. **14**, 678-680 (2002).
83. S. Adachi, and y. Koyamada, “Analysis and design of Q-switched erbium-doped fiber lasers and their application to OTDR,” IEEE J. Lightwave Technol. **20**, 1506-1511 (2002).

# VITA

Xiaoke Wan was born in Chongqing, China in 1974. He received a B.S. degree of physics from Jilin University in 1994 and an M.S. degree in optics from Shanghai Institute of Optics and Fine Mechanics, Chinese Academy of Sciences in 1997. He came to Texas A&M University in 1997 and received a M.S. degree in physics in 1999.

In January 2000, he joined the Electrical Engineering Department at Texas A&M University, and he worked as a research assistant in the Fiber Optics group with Dr. Henry F. Taylor.

His major interests include fiber optic sensors, fiber optics and lasers.

Mailing address: Electrical Engineering Department
Texas A&M University, College Station, TX 77843
E-mail address: xkwan@ee.tamu.edu